Spring 5-9-2020

Charge Transfer and Plasmon-Pumped Molecular Excitation Mechanisms in Surface Enhanced Photochemistry

Tefera Entele Tesema
University of New Mexico

Tefera Entele Tesema
Candidate

Chemistry and Chemical Biology
Department

This dissertation is approved, and it is acceptable in quality and form for publication:

Approved by the Dissertation Committee:

Professor Terefe Habteyes, Chairperson

Professor Yang Qin

Professor John Grey

Professor Alejandro Manjavacas

Title
CHARGE TRANSFER AND PLASMON-PUMPED MOLECULAR EXCITATION MECHANISMS IN SURFACE ENHANCED PHOTOCHEMISTRY

By

B.Sc., Chemistry, Addis Ababa University, Ethiopia, 1997
M.Sc., Inorganic Chemistry, Addis Ababa University, Ethiopia, 2002

DISSERTATION

Submitted in Partial Fulfillment of the
Requirements for the Degree of

Doctor of Philosophy

Chemistry

The University of New Mexico
Albuquerque, New Mexico

May, 2020

DEDICATION

DEDICATED TO MY FAMILY

IN PARTICULAR TO

MY WIFE

ABAYNESH BOGALE KABTYIMER

MY DAUGHTER

DHARRAA TEFERA ENTELE

MY SONS

MADDAA TEFERA ENTELE

AND

HUNDE TEFERA ENTELE

ACKNOWLEDGMENTS

I delightedly acknowledge my advisor Dr. Terefe G. Habteyes for allowing me to be part of his research group. Dr. Habteyes thank you a lot for your unreserved support, dedicated guidance, and very kind advice sometimes as a professor, sometimes as a colleague, and sometimes as an elder brother. I learned a lot from you. I would also like to thank, Dr. Yang Qin, Dr. John Grey, and Dr. Alejandro Manjavacas for being my dissertation committee. I appreciate your scholarly advice, support, and recommendations in my graduate research. Dr. Qin thank you for your kindness and excellent teaching style in the polymer course you taught me in 2014 and Dr. Grey for making that difficult Quantum chemistry course simpler and enjoyable in my first semester of the graduate program. Dr. Manjavacas you gave me interesting insight about plasmonic in the series of a lecture you gave at CHTM and presentation during group meetings while we have been collaborating on charge transfer mechanisms in particle-film plasmon coupling.

I would like to thank Habteyes group Sharmin Haq, Bijesh Kafle, Hamed Kookhaee, Chih-feng Wang, Isadora Nizalowski, Bisweswar Patra, and Eric Gomez for your kind support and friendship, Jenny Sanchez for your unforgettably very good friendship and moral support, Meron Tadese and Claudia Rivera for your help in solution preparation and Langmuir-Blodgett (LB) films fabrication. Furthermore, I would like to acknowledge the department of chemistry and chemical biology for lab facility, center for high technology materials (CHTM) for research lab and office facilities, and center for integrated nanotechnology (CINT) at Sandia National Laboratory for giving me access to integrated semiconductor processing lab. I express my sincere gratitude to Dr. Martin

Kirk for allowing me to use his UV-Vis-NIR spectrometer and his student KC for assisting me in the measurement. I thank Dr. Jeff Rack for guiding me during my research proposal defense.

Finally, I gratefully acknowledge my wife Abaynesh Bogale for her love, encouragement, and taking care of our children while I am away for such a long time. Abay, without your kind help, this Ph.D. work would have not been accomplished. I have a big appreciation for your love and support.

CHARGE TRANSFER AND PLASMON-PUMPED MOLECULAR EXCITATION MECHANISMS IN SURFACE ENHANCED PHOTOCHEMISTRY

by

Tefera Entele Tesema

B.Sc., CHEMISTRY, ADDIS ABABA UNIVERSITY, ETHIOPIA, 1997

M.Sc., INORGANIC CHEMISTRY, ADDIS ABABA UNIVERSITY, ETHIOPIA, 2002

Ph.D., CHEMISTRY, UNIVERSITY OF NEW MEXICO, USA, 2020

ABSTRACT

Photochemistry that can be driven at low incident photon flux on optically excited plasmonic nanoparticles is attracting increasing research interest because plasmon-driven reactions offer new pathways for efficient conversion of the abundant solar energy into fuel. The confinement of the electromagnetic field by plasmonic metal nanoparticle and consequent field enhancement gives a dual advantage of ultrasensitive *in situ* and *operando* spectroscopic methods to monitor enhanced field-driven photochemical transformation. Charge carrier driven either via direct or indirect excitation mechanism are well-established pathways in plasmon-driven reactions to date. However, the excitation mechanism via plasmon-pumped electron transition from an occupied molecular orbital (HOMO) to an unoccupied molecular orbital (LUMO) of the adsorbate is not well understood and hence not reported yet. Here, we address for the first-time excitation wavelength-dependent plasmon-pumped electronic excitation mechanism to initiate surface photochemistry based on the N-demethylation of methylene blue (MB) on gold nanostructures. At excitation wavelength that overlaps with the resonances of MB and the localized surface plasmon

resonance of gold nanoparticles, we enhanced selectively conversion of MB to thionine (TH) in the presence of oxygen in the atmosphere and water in the surface–molecule complex. In this mechanism, the intense electric field pushes the ground state of the adsorbed MB and increase the population of the excited state that increases the quantum yield of singlet oxygen generated via energy transfer from MB triplet excited state to oxygen in triplet ground state. The chemical changes are monitored by detecting the vibrational signatures of the reactant and product species in situ using surface-enhanced Raman scattering (SERS) spectroscopy.

It is important to note that enhanced surface chemistry and ultrasensitive spectroscopic methods depend strongly on enhanced adsorbate absorption. However, accurate determination of the adsorbate on the surface of metal nanoparticle is often ignored because of the technical difficulties for direct absorption measurements. Here, we show that molecule-plasmon weak excitation coupling can be used for determining the electronic absorption band of resonant adsorbates with sensitivity down to sub-monolayer surface coverage. By comparing the absorbance of gold nanoisland (AuNI) with and without adsorbate of resonant molecules (methylene blue (MB) and thionine (TH)), induced transparency is observed at the absorption band of the adsorbates. Apart from significant spectral broadening and red shifting of peak wavelength, the inverted transparency spectrum has a surprising similarity to the absorption spectrum of the corresponding dye in solution. Interestingly, the adsorption isotherm determined based on the integral area under the inverted transparency spectra is linearly correlated to the corresponding isotherm determined based on adsorbate induced plasmon resonance red shift. The results presented

in this work demonstrate a simple, sensitive and reliable approach for determining adsorbate absorption spectrum from molecule-plasmon excitation coupling.

TABLE OF CONTENT

Title ii

DEDICATION iii

ACKNOWLEDGMENTS iv

ABSTRACT vi

TABLE OF CONTENT ix

LIST OF FIGURES xiv

1 Introduction 1

1.1 Localized surface plasmon resonances (LSPR) and their application 1

1.2 Plasmon-driven reaction via charge transfer mechanism 3

1.2.1 Hot electron transfer mechanism: Indirect and Direct mechanisms 4

1.3 Photothermal mechanism (phonon driven) excitation 8

1.4 Plasmon-pumped adsorbate electronic excitation mechanism 9

1.5 Statement of the problem 10

1.6 Organization of the dissertation 12

1.7 References 13

2 Methods and Background 20

2.1 Chemicals and materials 20

2.1.1 Dyes and other organic and inorganic molecules 20

2.1.2 Gold nanoparticles and semiconductor quantum dots 20

2.1.3 Solvents 21

2.1.4 Materials 21

2.2 Methods 22

2.2.1 Sample preparation for SERS Experiments 22

2.2.2 Preparation of SAM Spacer between nanostructure and adsorbate 24

2.2.3 Surface enhanced Raman spectroscopy (SERS) 25

2.2.4 Dark-field scattering measurement. 27

2.2.5 UV-Visible Spectroscopic Measurements 29

2.2.6 Thin film fabrication techniques and synthesis of gold nanorods 30

2.2.6.1 Electron beam metal evaporation and deposition 30

2.2.6.2 Langmuir-Blodgett technique to prepare quantum dot thin films 30

2.2.6.3 CTAB capped Seed mediated Synthesis of Gold Nanorods 31

2.2.6.4 Template stripping of AuF 32

2.2.6.5 Atomic layer deposition (ALD) of Al_2O_3 dielectric spacer 33

2.2.7 Structural Characterization 33

2.3 Background 36

2.3.1 Photophysics and photochemistry of phenothiazinium dyes 36

2.3.2 Surface-enhanced Raman Spectroscopy (SERS) 39

2.3.3 Origin of electromagnetic enhancement mechanism in SERS 40

2.4 References 43

3 Plasmon Enhanced Resonant Excitation and Demethylation of Methylene Blue 47

3.1 Abstract 47

3.2 Introduction 48

3.3 Spectral overlap of the molecular and plasmon resonances 49

3.4 Surface-Enhanced Raman Spectra to Monitor Photochemistry 52

3.5 Laser power dependence of temporal evolution of SERS signals 54

3.6 Comprehensive analysis of the temporal evolution of SERS signals 56

3.7 Effect of excitation source and localized surface plasmon resonance on N-demethylation 58

3.7.1 Effect of supporting substrate on the spectral position of localized surface plasmon resonance 58

3.7.2 Excitation wavelength Dependence 60

3.8 Mechanism of Plasmon-Enhanced Excitation and Demethylation 62

3.9 Conclusion 66

3.10 References 67

Chapter Four: 74

4 Plasmon-Enhanced Autocatalytic N-Demethylation of Methylene Blue 74

4.1 Abstract 74

4.2 Introduction 75

4.3 Results and Discussion 78

4.3.1 Plasmon-enhanced photochemistry in ambient condition 78

4.3.2 Scattering spectrum of gold nanorods and absorption spectra of methylene blue and its N-demethylation derivatives 78

4.3.3 Raman and SERS spectra of MB and its N-demethylation derivatives..... 79

4.4 Photochemical reaction in reactive and inert atmosphere 83

4.5 Effect of spacer layer on photochemical N-demethylation 93

4.6 4.5 Effect of dehydration. 95

4.7 4.6 Mechanism of plasmon-pumped adsorbate excitation 97

4.8 Conclusion 103

4.9 Reference 104

5 Extracting transition band of adsorbate from molecule-plasmon coupling 111

5.1 Abstract 111

5.2 Introduction 112

5.3 Result and Discussion 115

5.4 Conclusion 125

5.5 References 126

6 Future work 130

6.1 Plasmon Assisted photobiology of phenothiazinium dyes 130

6.2 Correlation of near-field distribution and Raman scattering 131

6.3 Exciton-Induced excitation of higher order plasmonic mode 132

6.4 References 139

1 Appendix A 141

LIST OF FIGURES

Figure 1.1: (a) Schematic of the nanoantenna that consists of two gold nanobars with W = 40 nm, L = 40–100 nm, H = 25–30 nm, and G < 20 nm.(b) Representative SEM image of the fabricated nanoantennas (c) field localization in the gap of coupled gold nanobars (d) Calculated field distribution. Taken from reference[6] copyright applied physics letter (2014)..... 1

Figure 1.2: Charge transfer excitation mechanisms (a) Indirect hot electron transfer mechanism. Hot electrons generated via nonradiative decay of an LSP to form transient negative ion (TNI) state of the molecule (b) direct charge transfer. Electrons are resonantly transferred from the metal nanoparticle (NP)to molecule..... 4

Figure 1.3: Potential energy surface for ground state and TNI..... 5

Figure 1.4:. A comparison of light-induced HD production (grey) relative to HD produced by the equivalent thermal response with no illumination (red). Adapted from ref[15] with permission..... 6

Figure 1.5: Schematic in visible photon driven reduction of activation barrier (E_a)..... 9

Figure 2.1: Schematic showing sample preparation scheme. (Left) AuNR deposited on SAM of molecules on gold film (right) probe molecule functionalized AuNR and deposited on oxide coated silicon wafer. Dimensions are not to scale..... 24

Figure 2.2: Schematic showing sample preparation scheme. (top) thin gold film containing gold nanoisland deposited on glass cove or silicon wafer and coated with PSS as spacer layer between AuNI and MB (bottom) same structure without a spacer layer (control sample). Dimensions are not to scale..... 25

Figure 2.3: Schematic diagram showing optical set up for Raman and PL measurements (a) simplified outline from laser input to signal out (b) detailed optical paths and components 26

Figure 2.4: Schematic showing the experimental setup for Stokes and Anti-Stokes Raman Scattering measurements 27

Figure 2.5: Schematic showing the dark-field scattering microscopy and spectroscopy experimental setup. 29

Figure 2.6: Schematic diagram (not to scale) for ANSOM set up 36

Figure 2.7: (a) absorption spectra of 15 μM aqueous solution of MB, AZB, AZA, and TH (b) absorption spectrum of a thin film of MB on a cover glass 38

Figure 2.8: Schematic of the spherical gold nanoparticle placed in an external electric field 42

Figure 3.1: The absorption spectrum of $1x10^{-6}$ M methylene blue in ethanol solution (black line) and the corresponding fluorescence (FL) spectrum (red line). (c) The absorption (black line) and scattering (cyan and red lines) of gold nanorods (AuNRs) with nominal diameter of 40 nm and length 90 nm. The scattering spectra of a single (cyan line) and aggregates (red line) of AuNRs are obtained as the nanorods are adsorbed on MB coated gold film 51

Figure 3.2: Temporal evolution of the SERS signal of methylene blue molecules in plasmonic cavities. (a) Intensity map representing 80 spectra acquired at different time delays after continuous irradiation with $\lambda = 633$ nm excitation source is turned on. (b) Representative SERS spectra of MB recorded at the time delays indicated on the plot (t_0

≈ 0.5 s, acquisition time of a single spectrum) compared to the Raman spectra of methylene blue (black line) and thionine (green line) solid powders. 52

Figure 3.3: Calculated Raman Shifts showing the vibrational modes excited as the methyl groups are replaced with hydrogen atoms in going from MB (bottom spectrum) to TH (top spectrum). We used B3LYP density functional theory for the calculation with DGDZVP basis sets using Gaussian 09 software. The calculation agrees well with experiment in predicting the 479 cm^{-1}band TH but not for MB. The spectrum of Azure B is similar to that of MB. The 479 cm^{-1} band appears for Azure A confirming the excitation of the vibrational mode is triggered by at least complete N-demethylation of terminal N-atom. For Azure C the spectrum is similar to TH apart from small down shift of frequency 53

Figure 3.4: Average SERS spectra of AuF-MB-AuNR obtained at 633 nm excitation wavelength and incident laser power of (a) 0.16 mW, and (b) 0.73 mW. Each intensity map represents 400 spectra acquired within 207 seconds, and the spectra at each time point are the average of at least 10 spectra that represent different locations on the sample. (c) Average of the spectra acquired within 207 seconds at incident laser power of 0.16 mW (black line), 0.34 mW (cyan line) and 0.73 mW (red line). Note that with increasing laser power, both the background and the vibrational band intensities increase. The flat region at ~707 cm^{-1} marked with vertical dashed line is used for background correction and for studying the temporal evolution of the vibrational band intensities. .. 55

Figure 3.5: Comprehensive analysis of the temporal evolution of the SERS signals using representative vibrational bands of reactant and product species. (a) The peak intensity of the 1621 cm^{-1} band plotted as a function of time. The solid lines represent exponential

function fit to the data.(b) The same as (a) but for 479 cm^{-1} band and a single exponential function is fit to the data. (c) The rate constants ($k = 1/\tau$) extracted from the fitting procedure in (a) and (b) are plotted as a function of laser power. 57

Figure 3.6: (a) Dark-field scattering spectra of aggregates of gold nanospheres (AuNSs, diameter 40 nm) (blue line) and gold nanorods (AuNRs, 40 nm × 148 nm) (red line) functionalized with MB and deposited on silica surface. (b) SERS spectra of MB adsorbed on the AuNS and AuNRs recorded 30 s after exposing to the lasers. The vertical dashed cyan lines indicate the vibrational frequencies of thionine at 479 and 804 cm^{-1}. The peak at 520 cm^{-1} in all the spectra in (b) is due to silicon. 61

Figure 3.7: Raman spectra of MB adsorbed on gold film without plasmonic nanoparticles. More than a monolayer layer of MB was adsorbed so as to improve the signal-to-noise ratio of the Raman spectrum. The spectra were recorded with an acquisition time of 1 s at 633 nm excitation wavelength and intensity of ~100 kW/cm^2. The vertical dashed green lines indicate absence of vibrational frequencies of thionine at 479 and 804 cm^{-1}. 62

Figure 3.8: Comparison of the temporal evolution of the Stokes (a) and anti-Stokes (b) Raman intensities of the 448 cm^{-1} and 479 cm^{-1} bands. (c) Stokes to ant-Stokes intensity ratio of the 479 cm^{-1} band plotted as a function of time. 64

Figure 3.9: Energy diagram showing excitation and decay channels of methylene blue. The singlet ground state (S_0) to single excited state (S_1) transition is accessible at 633 nm excitation. After intersystem crossing (ISC), the triplet state population can be annihilated via efficient energy transfer (ET) to molecular oxygen in the ground state ($^3O_2$) that leads to excitation to singlet oxygen ($^1O_2$)..... 65

Figure 4.1: The absorption spectra of MB, azure B, azure A, and thionine in water and the plasmon scattering spectrum of AuNRs (Diameter 40 nm and length 90 nm) aggregated on coverslip 78

Figure 4.2: Normal Raman spectra of solid powders (blue lines) and SERS spectra (red lines) of methylene blue, azure B, azure A, and thionine as labeled. 81

Figure 4.3**:** Temporal evolution of SERS spectra demonstrating PEND-MB. (a) Representative SERS spectra recorded in ambient atmosphere at the beginning (black line) and after 200 s of illumination using 633 nm excitation wavelength. (b) Intensity map representing 400 spectra acquired sequentially during illumination for about 207 s. The zoom-in intensity maps at the bottom show the important spectral changes with time. Each spectrum is recorded with 0.5 s acquisition time at 0.4 mW incident power focused with 0.7 NA objective. 82

Figure 4.4: Illustration of background signal change as a function of continuous illumination. (a) Spectra at the beginning of illumination (black line) and after 207 seconds (red line). (b) Time dependence of the background signal where there is no vibrational band (at position ~707 cm^{-1}). The trend is the same if other locations labeled 1, 2 or 3 in (a) are used. (c) The spectra acquired at 0.5 s and 207 s exposure time after background correction 84

Figure 4.5 Schematic showing the experimental setup of the photochemical reaction under the flow of different gases over the solid thin film of sample (MB adsorbed on gold nanostructures). 86

Figure 4.6: Temporal evolution of the SERS signal of MB adsorbed on AuNRs and illuminated with 0.4 mW of 633 nm CW laser (focused with 0.7 NA objective) in air (a,

d), oxygen (b, e), and nitrogen (c, f) atmospheres. The SERS spectra are acquired continuously with 0.5 s acquisition time for over 200 s of continuous illumination, and the black, green, red, and blue lines in (a)−(c) represent average spectra of at least 10 different spots on the same sample at different exposure times, as labeled. (d) & (f) Integrated intensities of representative vibrational bands plotted as a function of exposure time. 87

Figure 4.7: Top panels: Intensity map representing 400 spectra showing the decline of MB reactant signal at 446 cm-1 and growth of thionine product signal at 479 cm-1 as a function of exposure time in (a) air, (b) oxygen and (c) nitrogen atmospheres. Middle panels: spectra showing the relative intensities of the 446 cm-1 (reactant) and 479 cm-1 (product) peaks at the beginning (black line) and end (red line) of illumination for 207 seconds in air, oxygen and nitrogen atmospheres. Bottom panels: product to reactant peak intensity ratios in air, oxygen and nitrogen atmospheres. 89

Figure 4.8: (a−c) Integrated and normalized relative intensities of representative vibrational bands plotted as a function of exposure time in (a) air, (b) oxygen, and (c) nitrogen atmospheres. (d−f) Vibrational frequency shift of the different bands as labeled based on the initial peak frequencies. The peak vibrational frequencies are determined by fitting a Gaussian function to the spectra. The integrated intensities and frequencies are extracted from 1000 spectra each recorded with 0.1 s acquisition time within 120 s of continuous exposure time using 0.2 mW of 632.8 nm CW laser that is focused with 0.7 NA objective. 90

Figure 4.9: (a) SERS spectra of methylene blue (black line) and azure B (red line) recorded at 0.4 mW of 633 nm CW laser and 0.5 s acquisition time in nitrogen

atmosphere. The spectra are recorded one after another at the same optical settings so that exactly the same reference point is used in determining the Raman shifts for the two compounds. (b) Ratio of the intensity at 1426 cm^{-1} to the peak intensity at ~1392 cm^{-1} (MB) or ~1386 cm^{-1} (azure B, azure A, and thionine). 93

Figure 4.10: (a) Representative spectra showing the relative intensities of the peaks labeled p1−p4 at the beginning (black line) and end (red line) of illumination at 633 nm for 207 s in the presence (upper two spectra) and absence (lower two spectra) of poly(sodium 4-styrenesulfonate) (PSS) coating on e-beam evaporated gold nanostructures as labeled. Each spectrum represents an average of at least 10 different spots on the same sample. (b) Peak intensity ratios as a function of exposure time. 95

Figure 4.11: Temporal evolution of the SERS signal for dehydrated MB−AuNR complex. The amount of adsorbed water is minimized by using ethanol solution of MB and AuNRs during the sample preparation. Representative spectra acquired under the flow of (a) dry O_2 gas and (b) O_2/ H_2O gas formed by passing the O_2 gas through a water bubbler (c, d) relative peak intensities extracted from the spectra acquired under the flow of (c) dry O_2 gas and (d) O_2/H_2O gas. 96

Figure 4.12: Schematic showing possible photophysical processes for MB on gold nanoparticles when the excitation energy is in resonance with the particle plasmon resonance and MB adsorbate electronic transition. The plasmon near field of the particle pumps the $S_0 \rightarrow S_1$ electronic transition of the MB adsorbate (blue lines). S_1 to T_1 intersystem crossing (purple arrow) can populate the MB T_1 state, from which energy transfer (green arrows) can promote oxygen from its triplet ground state ($^3O_2$) to singlet

excited state ($^1O_2$). The black arrows indicate energy transfer to the metal surface, and red arrows indicate hot electron transfer to the unoccupied adsorbate states. 99

Figure 4.13: Relative adsorption energy per gram for methylene blue (MB), azure B (AZB), azure A (AZA), azure C (AZC), and thionine based on the theoretical results in ref 52. 103

Figure 5.1: Schematic that shows the principle of the experiment. (b) Scanning electron microscope image of the gold nanoislands formed by electron-beam evaporation of gold on glass. (c) Calculated near-field distribution at λ = 680 nm..... 116

Figure 5.2: Experimental procedure for determining adsorbate induced transparency. (a) The dotted black (AuNI-1) and red lines (AuNI-2) are absorption spectra of two different bare plasmonic AuNIs. The solid lines (A_N) and (A_R) show the absorption spectra after the non-resonant MHA and resonant MB molecules are adsorbed on the AuNI-1 and AuNI-2, respectively. (b) Difference spectrum obtained by subtracting A_N from A_R. (c) The inverted difference spectrum (blue line) compared to the absorption spectrum of MB in water (black line). 118

Figure 5.3: Representative AFM image of the AuNI 119

Figure 5.4: Spectral evolution depending on adsorption time. (a) The absorption spectra of the same AuNIs as the adsorption time of MB is increased from 0 (black line, bare gold) to 60 minutes (pink line). (b) Difference spectra obtained by subtracting the spectrum of AuNI-MHA from the AuNI-MB spectra at different adsorption time. The numbers next to each plot are the adsorption time in minutes. (c, d) Same as (a, b) for thionine as adsorbate. 121

Figure 5.5: (a, b) Adsorption isotherms determined from plasmonic absorbance intensity changes induced by MB (a) and TH (b). (c, d) Adsorption isotherms determined from plasmon resonance wavelength shifts induced by MB (c) and TH (d). (e, f) Correlation between normalized intensity changes and plasmon resonance wavelength shift for MB (e) and TH (f) The numbers in (e) indicate the concentration in μM of MB water, in which nominally the same AuNIs are immersed. 123

Figure 6.1: Experimental setup and near-field optical amplitude and optical phase images of gold nanorods randomly dispersed on oxide-coated silicon wafer. Adapted with permission from reference [14] Copyright (2014) American Chemical Society..... 131

Figure 6.2: schematic show method for probing plasmon-exciton interaction..... 132

Figure 6.3: AFM image of Langmuir Blodgett (LB) monolayer films of CdSeS/ZnS-645, QD645 (orange) on top of monolayer of CdSeS/ZnS-450, QD450 (red). The substrate (black) is an oxide coated silicon wafer. (b) AFM film thickness profile measured along white dashed line. (c) Photoluminescence spectra of QD450 and QD645. The average size of QD450 and QD645 are 9.1 and 12.6 nm respectively..... 133

Figure 6.4: Photoluminescence (PL) peak position shift (a), FWHM shift (b), and normalized peak intensity (c) as a function of time at excitation wavelength of 532 nm for a system of QD645 on QD450 (blue dot); QD645 on glass (black diamond); QD630 on QD450 (green triangle). 135

Figure 6.5: Photoluminescence (PL) peak position shift (a), FWHM shift (b), and normalized peak intensity (c) as a function of time at excitation wavelength of 405 nm for a system of QD645 on QD450. Blue dot is for QD645 spectrum and black diamond is for QD450..... 136

Figure 6.6: Variation in emission peak position (a), FWHM (b), and normalized intensity (c) as a function of time at different intensities of light source. Low intensity, 6 kW/cm^2 (black square), medium intensity, 28 kW/cm^2 (red dot), and high intensity, 55 kW/cm^2 (green diamond) 138

LIST OF ABBREVIATION

3,3’-diethylthiadicarbocyanin iodide (DTCC) 18

6-mercaptohexanoic acid (6-MHA) 18

Aperture less (scattering type) near-field scanning optical microscope (ANSOM) 32

Atomic force microscope (AFM) 32

atomic layer deposition (ALD) 31

azure A (AZA) 18

Azure B (AZB) 18

center for high technology materials (CHTM) 18

Center for High Technology materials (CHTM) 19

cetyltrimethylammonium bromide (CTAB) 19

crystal violet (CV) 18

deionized (DI) 19

gold nanoisland (AuNI) 22

gold nanorods (AuNR) 19

Gold nanospheres (AuNS) 19

Langmuir-Blodgett (LB) 20, 28

methylene blue (MB) 18

Phenothiazine (PTz) 18

Photoluminescence (PL) 24

poly(sodium-4-styrenesulfonate) (PSS) 18

quantum dots (QD) 19

Rhodamine B (RhB) 18

Scanning electron microscope (SEM) 32

Self-Assembled monolayer (SAM)..... 21

surface enhanced Raman scattering (SERS)..... 21

thionine(TH) 18

Transmission electron microscope (TEM)..... 32

Trimethylaluminium (TMA)..... 31

University of New Mexico (UNM)..... 18, 19

1 Introduction

1.1 Localized surface plasmon resonances (LSPR) and their application

Localized surface plasmon (LSP) are excitations due to the oscillation of conduction electrons of finite nanostructures coupled to an electromagnetic field. This excitation creates enhanced surface field confined to a nanoscale volume that is beyond diffraction-limited.[1-5] For example, large field enhanced localization of plasmonic hotspot at short interparticle separation ($d \ll \lambda$) distances (gaps) has been quantified by using near-field optical imaging technique with spatial resolution on the order of 10 nm (**Figure 1.1)**.

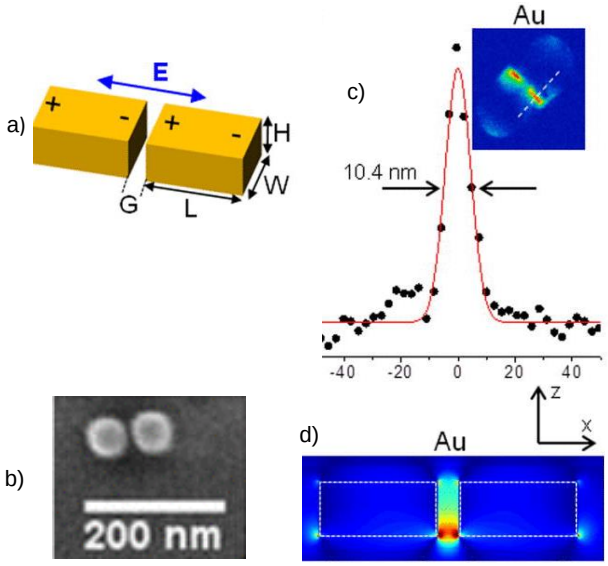

Figure 1.1 (a) Schematic of the nanoantenna that consists of two gold nanobars with W = 40 nm, L = 40–100 nm, H = 25–30 nm, and G < 20 nm.(b) Representative SEM image of the fabricated nanoantennas (c) field localization in the gap of coupled gold nanobars (d) Calculated field distribution. Taken from reference[6] copyright applied physics letter (2014)

When molecules are adsorbed on the surface of the plasmonic nanoparticles or in the gap between the particle and metal film system, their spectroscopic signal can be enhanced enormously by the plasmon near-field, an evanescent wave that decays exponentially with

distance from the surface. The near-field effect has led to the development of highly sensitive spectroscopy, notably surface-enhanced Raman scattering (SERS) spectroscopy[7] to the extent that Raman scattering due to single molecules can be detected.[8, 9] In addition to enhancing spectroscopic signals, optical excitation of plasmon resonances can drive surface photochemistry of adsorbates.[10-16] These dual plasmonic effects inherently combine surface reactions and in situ detection of reactant and product species, providing a convenient platform for mechanistic investigation of surface photochemistry. Albeit plasmon-enhanced spectroscopy such as SERS is relatively well established,[17-19] plasmon-driven photochemical reaction is a growing area of research and becoming a very active current research interest.

There are three different mechanisms of plasmon-mediate surface photochemical reactions. The first and most frequently explored mechanism is a plasmon-driven charge transfer excitation mechanism that involves the transfer of hot electrons from a metal to adsorbate.[20-22] Second, surface plasmons generated local heating to drive a chemical reaction in a way distinctly different from the conventional thermal driven process.[5, 23-27] The third and probably the least explored but yet important excitation mechanism is plasmon-pumped (near-field enhanced) electronic excitation of adsorbates. The three methods will be described in the following section with the emphasis on the third mechanism.

1.2 Plasmon-driven reaction via charge transfer mechanism

As stated above, metal nanoparticles are capable of field confinement by using LSP and form an intense density of state that accelerates electrons to unoccupied state within the particle. The confinement within a finite size of the particle also reduces electron-electron interaction and electron-phonon coupling that positively contribute to the lifetime of the non-thermal electron much longer than femtosecond duration exhibited by extended surface to do the intended job.[15, 22, 28]

Excited LSP relaxes via radiative and non-radiative decay paths. The non-radiative damping of the plasmon energy generates highly energetic electron-hole pairs, a hot carriers-a process called Landau damping within a short period. (~10 fs for Au and Ag). The hot electrons have a transient, non-thermal energy distribution that will eventually scatter with the other electrons to form high-temperature Fermi-Dirac thermal distribution within~100 fs.[29] However, no clear consensus has been reached among the researchers working actively on this area as to which electron distribution is involved to induce chemical reaction. The non-thermal hot electrons have higher energy and longer lifetime than the thermal distribution to play dominant role in chemical reaction.[30] Depending on the nature and size of the nanoparticle, the time scale for the decay of the excited electrons (hot electrons) ranges from 1–10 picoseconds.[22, 31]

1.2.1 Hot electron transfer mechanism: Indirect and Direct mechanisms

In charge carrier driven reaction mechanism, energetic electrons or holes formed according to the mechanism described above on the surface of nanoparticles, transiently occupy energetically accessible orbitals of the adsorbed molecule before their energy is dissipated into phonon modes of nanoparticles. This process is called indirect charge transfer mechanism and it's schematically depicted in **Figure 1.2**a. The energetic electrons that are injected into the adsorbed chemical species form transient negative ion (TNI) state.

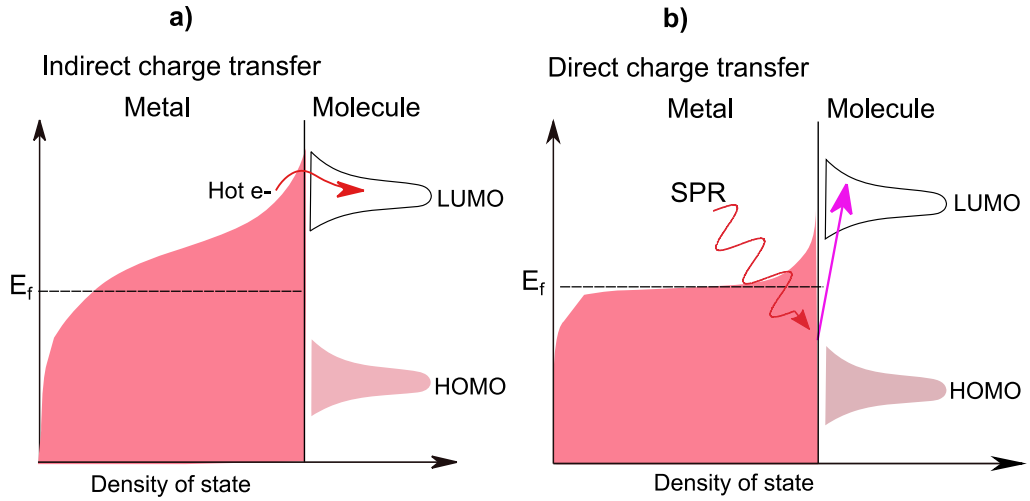

Figure 1.2 Charge transfer excitation mechanisms (a) Indirect hot electron transfer mechanism. Hot electrons generated via nonradiative decay of an LSP to form transient negative ion (TNI) state of the molecule (b) direct charge transfer. Electrons are resonantly transferred from the metal nanoparticle (NP)to molecule.

The TNI relaxes by releasing an electron back to the metal and returning to neutral potential energy surface (PES) with vibrational excitation in the adsorbate (**Figure 1.4**).

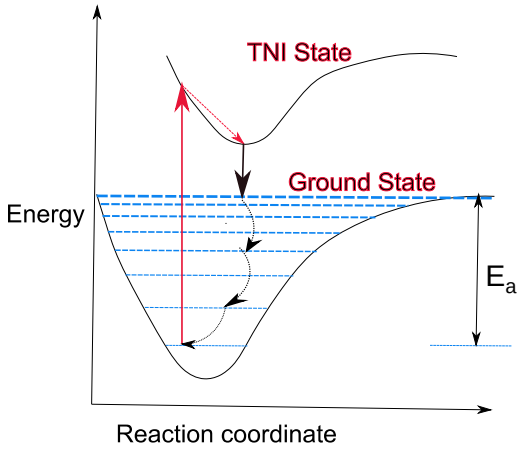

Figure 1.3 Potential energy surface for ground state and TNI

When the vibrational energy acquired through this process is sufficient to overcome the activation barrier, chemical reaction occurs.

The direct charge transfer mechanism also known as chemical interface damping assumes that the SPR-mediated photon absorption occurs through the creation of electron–hole pairs of specific energy that are localized on the adsorbate as illustrated in **Figure 1.2**b. In this process, the presence of unoccupied adsorbate orbitals that match with SPR for the direct resonant transition from occupied to unoccupied orbitals of the molecule–nanoparticle complex. An example of this type of mechanism have been demonstrated by using methylene blue adsorbed on aggregates of silver cube and performed wavelength dependent rate of degradation of methylene blue[32]. Interestingly, they observed that the Anti-Stokes Raman signal at excitation source of 532 nm and 785 nm at the same photon flux is much higher for 785 nm than that of 532 nm, indicating the process of charge excitation at 785 nm resulted in energy being selectively stored into the adsorbate than heating the entire system. This observation is the direct consequence of plasmon-mediated

pumping of excited vibration modes of the adsorbate and subsequent photochemical reaction.

A typical example (see **Figure 1.4**) of reactions known to be initiated by hot electron transfer is the H_2 dissociation reaction on surface small (5-30 nm) gold nanoparticle supported on SiO_2.[33] The reaction was monitored by following the formation of HD as indicated in the chemical equation below. The significant response under laser illumination compared to that of thermal equivalent indicate the role SPR to generate hot electron and cause a reaction by the indirect transfer process.

$$H_2 + D_2 \xrightarrow[\text{laser (white light)}]{\text{AuNP (5-30 nm),}} 2HD$$

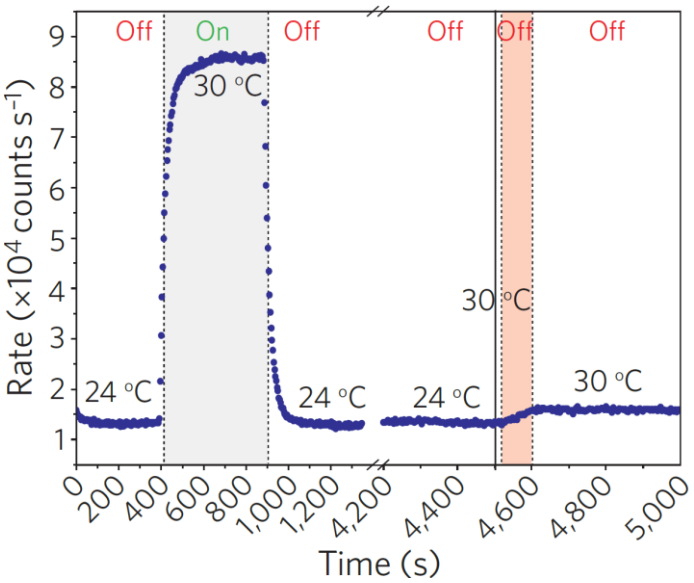

Figure 1.4. A comparison of light-induced HD production (grey) relative to HD produced by the equivalent thermal response with no illumination (red). Adapted from ref[15] with permission

Recent theoretical modeling shows that the antibonding molecular orbital of the H_2 that hybridizes with a gold nanoparticle lies about 1.5 eV above the Fermi energy of the metal, indicating the feasibility of particle-molecule charge transfer.[34] Since the potential energy surface of the antibonding orbital is repulsive, the charge transfer can lead to dissociation of the molecule.

Many studies have also reported charge-transfer driven reactions (some involve bimetallic nanoparticle) of more complex molecules This includes the reduction of nitrobenzene and its derivatives[35], esterification reaction[36], Cross-coupling reactions[37, 38], oxidation of benzyl alcohol to benzaldehyde,[39] and 2-propanol to acetone[40]. Other examples of plasmon-driven chemical reactions that may involve hot-electron transfer include ethylene epoxidation,[41] azo-coupling of para-aminothiophenol[42-48] and para-nitrothiophenol,[49-54] as well as their redox interconversion,[55 56] and CO_2 reduction.[57, 58] Except for the H_2 dissociation and CO_2 reduction, the other reactions are believed to involve oxygen that can be activated by the energetic plasmon electrons.[41, 46, 48] That is, for the most part, the hot electron transfer mechanism may result in the formation of surface-bound transient anionic species such as H^-, O_2^- or CO_2^-. Interestingly, the formation of these species is well known from gas-phase studies.[59-62] In the gas-phase, metastable anions can be stabilized through solvation,[63-65] while interaction with the nanoparticle surface and co-adsorbates such as water and oxygen molecules can have a similar stabilizing effect.

1.3 Photothermal mechanism (phonon driven) excitation

Non-radiatively excited electrons and holes losses their excitation via electron-phonon interaction in the sub-Pico second to picosecond time scale. The excited phonon modes undergo phonon-phonon coupling and reach thermal equilibrium with the surrounding medium in about 100 ps. Under CW laser the nanoparticles are subjected to a steady-state temperature that is higher than the bulk. Therefore the excitation of plasmons is always accompanied by a photothermal heating effect.[66] Many studies have been reported the difficulty of distinguishing whether the enhancement in reaction kinetics is due to non-thermal or thermal or if both which process contributes more is still an unanswered question. Plasmon mediated reduction of the activation barrier in the conversion of ammonia into elemental nitrogen and hydrogen is an example of photothermal driven excitation mechanism reported recently by using an alloy of copper nanoparticle and ruthenium.[67] The reduction in activation barrier was observed to be dependent on the intensity and wavelength of the excitation light source. The schematic in **Figure 1.5** predicts the effect of light on the activation enthalpy of the reaction.

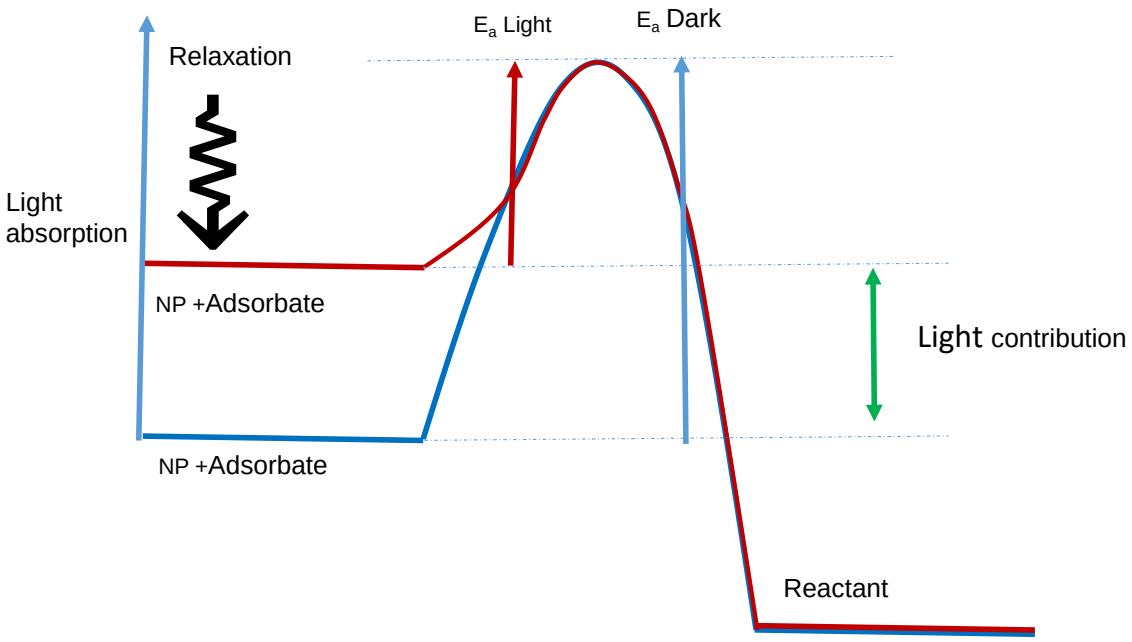

Figure 1.5 Schematic in visible photon driven reduction of activation barrier (E_a)

1.4 Plasmon-pumped adsorbate electronic excitation mechanism

To our knowledge, no study about the mechanism of excitation for photochemical transformation via plasmon-pumped resonant electronic excitation of the adsorbate. The localized surface plasmon resonances (LSPR) of gold nanorods used in this study are to provide a highly intense electric field that pushes the valence electrons of adsorbate in the ground state configuration to excited electronic state at the proper frequency to overcome unfavorable damping of molecular excitation by metal surface. Interestingly, for physisorbed molecules that have triplet state, intersystem crossing rate is not affected by the surface and hence increase the lifetime of the excitation to do photochemistry.[70] Recently, wavelength-dependent surface plasmon enabled photodissociation of $(CH_3S)_2$ on single crystal Ag(111) and Cu(111) metal surfaces has been reported to be initiated by near-field enhanced direct electronic excitation of the reactant.[71, 72] However, the

mechanism of excitation assisted by the near field created by was not clear as surface plasmon lifetime is very short in such extended metal structure.

Optical absorption of molecules adsorbed on metal nanoparticles can cause significant shifts in their electronic band. Overlap between this band and plasmon resonance can be affected by adsorption induced spectral shift and linewidth broadening.[73-75] The magnitude of this shift and broadening depends on the extent of metal-molecule interaction and makes the spectral position of surface absorption band uncertainty unless systematic measurements are performed. At sub-monolayer this optical modification cannot be associated with molecule-molecule interactions and hence it is the intrinsic effect of the adsorption to the metal surface. This knowledge is very important in quantitative interpretation of SERS[76] , enhanced surface photochemistry, and adsorption kinetics at monolayer or less coverage[77]. Compared to conventional methods,[78, 79] which lack surface specificity due to interferences from non-adsorbate molecules in a solution or limited by electrochemical properties of the molecules,[80-82] surface-specific absorption spectra of molecular adsorbate on metallic nanoparticles at monolayer coverage with enhancement in sensitivity over 40 times can be obtained by using SPR.[77]

1.5 Statement of the problem

In this dissertation, the author used the plasmon-enhanced photochemical conversion of methylene blue to thionine as one of the most interesting model systems for mechanistic investigation. It is a slow process that involves intermediates and therefore competition between enhanced absorption and quenching by co-adsorbate is inevitable.[83] Here, it is interesting to note that the best place to see enhanced photochemistry of this type is not

directly on the surface metal nanoparticle but a short distance above it where the best compromise is struck between field enhancement and nonradiative damping. For this, we implemented nanoparticle-on-metal film or dielectric support configuration by coupling colloidal gold nanorods to the substrates and have studied the photophysical characteristics of the coupled system for the intended application. The choice of AuNRs was based on (1) the inherently much narrower resonances of AuNRs than that of a classic model system of gold spheres[84] are desirable to probe the plasmonic responses of the coupled system with higher sensitivity (2) the aspect ratio dependent tunability of the surface plasmon resonances of gold nanorods (3) unlike spherical particles on metal film which has only out-of-plane polarization via dipole-image dipole interaction, excitation of cavity resonances of gold nanorods on metal film is more efficient for in-plane polarized excitation field.

The chemical properties of these colloidal solutions of the nanoparticles depend on the nature of surface ligands that provide a natural spacer of thickness on the order of few nanometers when they are self-assembled on metal film or dielectric substrate. But much more precise thickness of the dielectric spacer layer between the nanoparticles and metal substrate was controlled by atomic layer deposition technics to determine the nature of the interaction, and hence the plasmonic response of the coupled system. Herein, the author addresses the research by introducing a new mechanism of excitation for photochemical transformation that is plasmon-pumped resonant electronic excitation in photochemical transformation processes using phenothiazinium dyes as a model system. Furthermore, we developed a method of extracting adsorbate adsorption band from molecule-plasmon

coupling interaction. Also, adsorption kinetics of these dyes on gold metal nanostructure from sub-monolayer to monolayer coverage have been investigated.

1.6 Organization of the dissertation

This dissertation is organized into six chapters. **Chapter 2** is about experimental and methods and background of model systems used in the study. **Chapter 3** covers the photochemical transformation of methylene blue under different excitation and the coupling of the molecules to a plasmonic system at different particle-substrate interfaces. **Chapter 4** presents **the** mechanism of plasmon-enhanced photochemistry under controlled atmospheric conditions. In this chapter details of the effect of the inert and reactive atmosphere, solvent, and distance of molecule from the metal surface on the mechanism of excitation are discussed. **Chapter 5** presents a study about adsorption induced surface absorption spectral shifts and line broadening of some selected phenothiazinium dyes and their adsorption kinetics. The last chapter (**Chapter 6**) contains brief future work.

1.7 References

1. Sarid, D. & Challener, W. Modern Introduction to Surface Plasmons (University Press, Cabridge, UK, 2010).

2. Willets, K.A. & Van Duyne, R.P. Localized surface plasmon resonance spectroscopy and sensing. Annual Review of Physical Chemistry 58, 267-297 (2007).

3. Jain, P.K., Huang, W.Y. & El-Sayed, M.A. On the universal scaling behavior of the distance decay of plasmon coupling in metal nanoparticle pairs: A plasmon ruler equation. *Nano Letters* **7**, 2080-2088 (2007).

4. Kiesow, K.I., Dhuey, S. & Habteyes, T.G. Mapping near-field localization in plasmonic optical nanoantennas with 10 nm spatial resolution. *Applied Physics Letters* **105**, 053105 (2014).

5. Golubev, A.A., Khlebtsov, B.N., Rodriguez, R.D., Chen, Y. & Zahn, D.R.T. Plasmonic Heating Plays a Dominant Role in the Plasmon-Induced Photocatalytic Reduction of 4-Nitrobenzenethiol. *The Journal of Physical Chemistry C* **122**, 5657-5663 (2018).

6. Kiesow, K.I., Dhuey, S. & Habteyes, T.G. Mapping near-field localization in plasmonic optical nanoantennas with 10 nm spatial resolution. *Applied Physics Letters* **105**, 053105 (2014).

7. Otto, A., Mrozek, I., Grabhorn, H. & Akemann, W. SURFACE-ENHANCED RAMAN-SCATTERING. *Journal of Physics-Condensed Matter* **4**, 1143-1212 (1992).

8. Nie, S. & Emory, S.R. Probing Single Molecules and Single Nanoparticles by Surface-Enhanced Raman Scattering. *Science* **275**, 1102-1106 (1997).

9. Kneipp, K. et al. Single Molecule Detection Using Surface-Enhanced Raman Scattering (SERS). *Physical Review Letters* **78**, 1667 (1997).

10. Linic, S., Aslam, U., Boerigter, C. & Morabito, M. Photochemical transformations on plasmonic metal nanoparticles. *Nature Materials* **14**, 567-576 (2015).

11. Zhang, Z.L., Xu, P., Yang, X.Z., Liang, W.J. & Sun, M.T. Surface plasmon-driven photocatalysis in ambient, aqueous and high-vacuum monitored by SERS and TERS. *Journal of Photochemistry and Photobiology C-Photochemistry Reviews* **27**, 100-112 (2016).

12. Kim, M., Lin, M., Son, J., Xu, H.X. & Nam, J.M. Hot-Electron-Mediated Photochemical Reactions: Principles, Recent Advances, and Challenges. *Advanced Optical Materials* **5**, 1700004 (2017).

13. Zhang, Y. et al. Surface-Plasmon-Driven Hot Electron Photochemistry. *Chemical Reviews* **118**, 2927-2954 (2018).

14. Kim, Y. & Kazuma, E. Mechanistic studies of plasmon chemistry on metal catalysts. *Angewandte Chemie International Edition* **0**.

15. Brongersma, M.L., Halas, N.J. & Nordlander, P. Plasmon-induced hot carrier science and technology. *Nature Nanotechnology* **10**, 25-34 (2015).

16. Liu, J.G., Zhang, H., Link, S. & Nordlander, P. Relaxation of Plasmon-Induced Hot Carriers. *ACS Photonics* **5**, 2584-2595 (2018).

17. Stiles, P.L., Dieringer, J.A., Shah, N.C. & Van Duyne, R.R. Surface-Enhanced Raman Spectroscopy. *Annual Review of Analytical Chemistry* **1**, 601-626 (2008).

18. Kneipp, K., Moskovits, M. & Kneipp, H. (eds.) Topics in Applied Physics (Springer, Germany, 2006).

19. Le Ru, E. & Etchegoin, P. Principles of Surface-Enhanced Raman Spectroscopy (Elsevier, Amsterdam, The Netherlands, 2009).

20. Govorov, A.O., Zhang, H. & Gun'ko, Y.K. Theory of Photoinjection of Hot Plasmonic Carriers from Metal Nanostructures into Semiconductors and Surface Molecules. *Journal of Physical Chemistry C* **117**, 16616-16631 (2013).

21. Sundararaman, R., Narang, P., Jermyn, A.S., Goddard, W.A. & Atwater, H.A. Theoretical predictions for hot-carrier generation from surface plasmon decay. *Nature Communications* **5** (2014).

22. Manjavacas, A., Liu, J.G., Kulkarni, V. & Nordlander, P. Plasmon-Induced Hot Carriers in Metallic Nanoparticles. *Acs Nano* **8**, 7630-7638 (2014).

23. Baffou, G. et al. Photoinduced Heating of Nanoparticle Arrays. *Acs Nano* **7**, 6478-6488 (2013).

24. Yang, H. et al. Quantitative Detection of Photothermal and Photoelectrocatalytic Effects Induced by SPR from Au@Pt Nanoparticles. *Angewandte Chemie-International Edition* **54**, 11462-11466 (2015).

25. Yu, Y., Sundaresan, V. & Willets, K.A. Hot Carriers versus Thermal Effects: Resolving the Enhancement Mechanisms for Plasmon-Mediated Photoelectrochemical Reactions. *The Journal of Physical Chemistry C* **122**, 5040-5048 (2018).

26. Kamarudheen, R., Castellanos, G.W., Kamp, L.P.J., Clercx, H.J.H. & Baldi, A. Quantifying Photothermal and Hot Charge Carrier Effects in Plasmon-Driven Nanoparticle Syntheses. *Acs Nano* **12**, 8447-8455 (2018).

27. Zhou, L.A. et al. Quantifying hot carrier and thermal contributions in plasmonic photocatalysis. *Science* **362**, 69-+ (2018).

28. Inouye, H., Tanaka, K., Tanahashi, I. & Hirao, K. Ultrafast dynamics of nonequilibrium electrons in a gold nanoparticle system. *Physical Review B* **57**, 11334-11340 (1998).

29. Fann, W.S., Storz, R., Tom, H.W.K. & Bokor, J. Electron thermalization in gold. *Physical Review B* **46**, 13592-13595 (1992).

30. Shin, H.-H., Koo, J.-J., Lee, K.S. & Kim, Z.H. Chemical reactions driven by plasmon-induced hot carriers. *Applied Materials Today* **16**, 112-119 (2019).

31. Sun, C.K., Vallée, F., Acioli, L.H., Ippen, E.P. & Fujimoto, J.G. Femtosecond-tunable measurement of electron thermalization in gold. *Physical Review B* **50**, 15337-15348 (1994).

32. Boerigter, C., Campana, R., Morabito, M. & Linic, S. Evidence and implications of direct charge excitation as the dominant mechanism in plasmon-mediated photocatalysis. *Nature Communications* **7**, 10545 (2016).

33. Mukherjee, S. et al. Hot Electrons Do the Impossible: Plasmon-Induced Dissociation of H-2 on Au. *Nano Letters* **13**, 240-247 (2013).

34. Zhang, Y., Nelson, T., Tretiak, S., Guo, H. & Schatz, G.C. Plasmonic Hot-Carrier-Mediated Tunable Photochemical Reactions. *Acs Nano* **12**, 8415-8422 (2018).

35. Zhu, H., Ke, X., Yang, X., Sarina, S. & Liu, H. Reduction of Nitroaromatic Compounds on Supported Gold Nanoparticles by Visible and Ultraviolet Light. *Angewandte Chemie International Edition* **49**, 9657-9661 (2010).

36. Zhang, Y. et al. Direct Photocatalytic Conversion of Aldehydes to Esters Using Supported Gold Nanoparticles under Visible Light Irradiation at Room Temperature. *The Journal of Physical Chemistry C* **118**, 19062-19069 (2014).

37. Wang, F. et al. Plasmonic Harvesting of Light Energy for Suzuki Coupling Reactions. *Journal of the American Chemical Society* **135**, 5588-5601 (2013).

38. Xiao, Q. et al. Visible Light-Driven Cross-Coupling Reactions at Lower Temperatures Using a Photocatalyst of Palladium and Gold Alloy Nanoparticles. *ACS Catalysis* **4**, 1725-1734 (2014).

39. Huang, X. et al. Plasmonic and Catalytic AuPd Nanowheels for the Efficient Conversion of Light into Chemical Energy. *Angewandte Chemie International Edition* **52**, 6063-6067 (2013).

40. Sugano, Y. et al. Supported Au–Cu Bimetallic Alloy Nanoparticles: An Aerobic Oxidation Catalyst with Regenerable Activity by Visible-Light Irradiation. *Angewandte Chemie International Edition* **52**, 5295-5299 (2013).

41. Christopher, P., Xin, H.L. & Linic, S. Visible-light-enhanced catalytic oxidation reactions on plasmonic silver nanostructures. *Nature Chemistry* **3**, 467-472 (2011).

42. Huang, Y.-F. et al. When the Signal Is Not from the Original Molecule To Be Detected: Chemical Transformation of para-Aminothiophenol on Ag during the SERS Measurement. *Journal of the American Chemical Society* **132**, 9244-9246 (2010).

43. Fang, Y.R., Li, Y.Z., Xu, H.X. & Sun, M.T. Ascertaining p,p '-Dimercaptoazobenzene Produced from p-Aminothiophenol by Selective Catalytic Coupling Reaction on Silver Nanoparticles. *Langmuir* **26**, 7737-7746 (2010).

44. Yan, X.F., Wang, L.Z., Tan, X.J., Tian, B.Z. & Zhang, J.L. Surface-Enhanced Raman Spectroscopy Assisted by Radical Capturer for Tracking of Plasmon-Driven Redox Reaction. *Scientific Reports* **6** (2016).

45. Choi, H.K., Shon, H.K., Yu, H., Lee, T.G. & Kim, Z.H. b(2) Peaks in SERS Spectra of 4-Aminobenzenethiol: A Photochemical Artifact or a Real Chemical Enhancement? *Journal of Physical Chemistry Letters* **4**, 1079-1086 (2013).

46. Huang, Y.F. et al. Activation of Oxygen on Gold and Silver Nanoparticles Assisted by Surface Plasmon Resonances**. *Angewandte Chemie-International Edition* **53**, 2353-2357 (2014).

47. Zhao, L.B. et al. Surface Plasmon Catalytic Aerobic Oxidation of Aromatic Amines in Metal/Molecule/Metal Junctions. *Journal of Physical Chemistry C* **120**, 944-955 (2016).

48. Xu, P. et al. Mechanistic understanding of surface plasmon assisted catalysis on a single particle: cyclic redox of 4-aminothiophenol. *Scientific Reports* **3**, 2997 (2013).

49. Dong, B., Fang, Y.R., Xia, L.X., Xu, H.X. & Sun, M.T. Is 4-nitrobenzenethiol converted to p,p '-dimercaptoazobenzene or 4-aminothiophenol by surface photochemistry reaction? *Journal of Raman Spectroscopy* **42**, 1205-1206 (2011).

50. Dong, B., Fang, Y.R., Chen, X.W., Xu, H.X. & Sun, M.T. Substrate-, Wavelength-, and Time-Dependent Plasmon-Assisted Surface Catalysis Reaction of 4-Nitrobenzenethiol Dimerizing to p,p '-Dimercaptoazobenzene on Au, Ag, and Cu Films. *Langmuir* **27**, 10677-10682 (2011).

51. Sun, M.T., Zhang, Z.L., Zheng, H.R. & Xu, H.X. In-situ plasmon-driven chemical reactions revealed by high vacuum tip-enhanced Raman spectroscopy. *Scientific Reports* **2** (2012).

52. van Schrojenstein Lantman, E.M., Deckert-Gaudig, T., Mank, A.J.G., Deckert, V. & Weckhuysen, B.M. Catalytic processes monitored at the nanoscale with tip-enhanced Raman spectroscopy. *Nature Nanotechnology* **7**, 583-586 (2012).

53. Kang, L.L. et al. Laser wavelength- and power-dependent plasmon-driven chemical reactions monitored using single particle surface enhanced Raman spectroscopy. *Chemical Communications* **49**, 3389-3391 (2013).

54. Choi, H.-K. et al. Metal-Catalyzed Chemical Reaction of Single Molecules Directly Probed by Vibrational Spectroscopy. *Journal of the American Chemical Society* **138**, 4673-4684 (2016).

55. Joseph, V. et al. Characterizing the Kinetics of Nanoparticle-Catalyzed Reactions by Surface-Enhanced Raman Scattering. *Angewandte Chemie-International Edition* **51**, 7592-7596 (2012).

56. Kafle, B., Poveda, M. & Habteyes, T.G. Surface Ligand-Mediated Plasmon-Driven Photochemical Reactions. *The Journal of Physical Chemistry Letters* **8**, 890-894 (2017).

57. Calaza, F. et al. Carbon Dioxide Activation and Reaction Induced by Electron Transfer at an Oxide-Metal Interface. *Angewandte Chemie-International Edition* **54**, 12484-12487 (2015).

58. Yu, S.J., Wilson, A.J., Heo, J. & Jain, P.K. Plasmonic Control of Multi-Electron Transfer and C-C Coupling in Visible-Light-Driven CO2 Reduction on Au Nanoparticles. *Nano Letters* **18**, 2189-2194 (2018).

59. Cooper, C.D. & Compton, R.N. METASTABLE ANIONS OF CO2. *Chemistry and Physics of Lipids* **14**, 29-& (1972).

60. Celotta, R.J., Bennett, R.A., Levine, J., Hall, J.L. & Siegel, M.W. MOLECULAR PHOTODETACHMENT SPECTROMETRY .2. ELECTRON AFFINITY OF O2 AND STRUCTURE OF O2. *Physical Review A* **6**, 631-& (1972).

61. Coe, J.V., Snodgrass, J.T., Freidhoff, C.B., McHugh, K.M. & Bowen, K.H. NEGATIVE-ION PHOTOELECTRON-SPECTROSCOPY OF THE NEGATIVE CLUSTER ION H-(NH3)1. *Journal of Chemical Physics* **83**, 3169-3170 (1985).

62. Kleingeld, J.C., Ingemann, S., Jalonen, J.E. & Nibbering, N.M.M. FORMATION OF THE NH4-ION IN THE GAS-PHASE. *Journal of the American Chemical Society* **105**, 2474-2475 (1983).

63. Grumbling, E.R. & Sanov, A. Solvation effects on angular distributions in H-(NH3)(n) and NH2-(NH3)(n) photodetachment: Role of solute electronic structure. *Journal of Chemical Physics* **135** (2011).

64. Habteyes, T., Velarde, L. & Sanov, A. Photodissociation of CO2- in water clusters via Renner-Teller and conical interactions. *Journal of Chemical Physics* **126** (2007).

65. Akin, F.A., Schirra, L.K. & Sanov, A. Photoelectron imaging study of the effect of monohydration on O-2(-) photodetachment. *Journal of Physical Chemistry A* **110**, 8031-8036 (2006).

66. Jain, P.K. Taking the Heat Off of Plasmonic Chemistry. *The Journal of Physical Chemistry C* **123**, 24347-24351 (2019).

67. Zhou, L. et al. Quantifying hot carrier and thermal contributions in plasmonic photocatalysis. *Science* **362**, 69-72 (2018).

68. Nitzan, A. & Brus, L.E. CAN PHOTOCHEMISTRY BE ENHANCED ON ROUGH SURFACES. *Journal of Chemical Physics* **74**, 5321-5322 (1981).

69. Nitzan, A. & Brus, L.E. THEORETICAL-MODEL FOR ENHANCED PHOTOCHEMISTRY ON ROUGH SURFACES. *Journal of Chemical Physics* **75**, 2205-2214 (1981).

70. Wolkow, R.A. & Moskovits, M. ENHANCED PHOTOCHEMISTRY ON SILVER SURFACES. *Journal of Chemical Physics* **87**, 5858-5869 (1987).

71. Kazuma, E., Jung, J., Ueba, H., Trenary, M. & Kim, Y. Direct Pathway to Molecular Photodissociation on Metal Surfaces Using Visible Light. *Journal of the American Chemical Society* **139**, 3115-3121 (2017).

72. Kazuma, E., Jung, J., Ueba, H., Trenary, M. & Kim, Y. Real-space and real-time observation of a plasmon-induced chemical reaction of a single molecule. *Science* **360**, 521-525 (2018).

73. Craighead, H.G. & Glass, A.M. OPTICAL-ABSORPTION OF SMALL METAL PARTICLES WITH ADSORBED DYE COATS. *Optics Letters* **6**, 248-250 (1981).

74. Darby, B.L., Auguie, B., Meyer, M., Pantoja, A.E. & Le Ru, E.C. Modified optical absorption of molecules on metallic nanoparticles at sub-monolayer coverage. *Nature Photonics* **10**, 40-U54 (2016).

75. Birke, R.L., Lombardi, J.R., Saidi, W.A. & Norman, P. Surface-Enhanced Raman Scattering Due to Charge-Transfer Resonances: A Time-Dependent Density Functional Theory Study of Ag-13-4-Mercaptopyridine. *Journal of Physical Chemistry C* **120**, 20721-20735 (2016).

76. Brus, L. Noble Metal Nanocrystals: Plasmon Electron Transfer Photochemistry and Single-Molecule Raman Spectroscopy. *Acc. Chem. Res.* **41**, 1742 (2008).

77. Knebl, D. et al. Gap plasmonics of silver nanocube dimers. *Phys. Rev. B: Condens. Matter Mater. Phys.* **93**, 081405 (2016).

78. Pozzi, E.A. et al. Evaluating Single-Molecule Stokes and Anti-Stokes SERS for Nanoscale Thermometry. *J. Phys. Chem. C* **119**, 21116 (2015).

79. Nguyen, S.C. et al. Study of Heat Transfer Dynamics from Gold Nanorods to the Environment Via Time-Resolved Infrared Spectroscopy. *ACS Nano* **10**, 2144 (2016).

80. Kazuma, E., Jung, J., Ueba, H., Trenary, M. & Kim, Y. Real-Space and Real-Time Observation of a Plasmon-Induced Chemical Reaction of a Single Molecule. *Science* **360**, 521 (2018).

81. Hartland, G.V., Besteiro, L.V., Johns, P. & Govorov, A.O. What's So Hot About Electrons in Metal Nanoparticles? *ACS Energy Lett.* **2**, 1641 (2017).

82. Linic, S., Aslam, U., Boerigter, C. & Morabito, M. Photochemical Transformations on Plasmonic Metal Nanoparticles. *Nat. Mater.* **14**, 567 (2015).

83. Nitzan, A. & Brus, L.E. Theoretical-Model for Enhanced Photochemistry on Rough Surfaces. *J. Chem. Phys.* **75**, 2205 (1981).

84. Pérez-González, O., Aizpurua, J. & Zabala, N. Optical transport and sensing in plexcitonic nanocavities. *Opt. Express* **21**, 15847 (2013).

2 Methods and Background

2.1 Chemicals and materials

2.1.1 Dyes and other organic and inorganic molecules

Solid powders of methylene blue (MB), $C_{16}H_{18}ClN_3S{\cdot}3H_2O$, azure A (AZA) chloride, dye content 70%, and thionine(TH) acetate, dye content ≥ 85%, crystal violet (CV), dye content ≥90%, 3,3'-diethylthiadicarbocyanin iodide (DTCC), dye content 98%, Rhodamine B (RhB), dye content 95%, Phenothiazine (PTz), purum ≥ 98.0%, (GC grade), 6-mercaptohexanoic acid (6-MHA), The dye contents were as certified by biological stain commission. All these chemicals were purchased from Sigma-Aldrich. Azure B (AZB), was purchased from Alfa Aesar, and poly(sodium-4-styrenesulfonate) (PSS) (70 kDa, Polysciences Inc., Warrington, PA, USA) and Sodium Chloride (99%, Aldrich). These chemicals were used as a dilute solution in water or ethanol without further purification Gold (99.999%, Process Materials, Inc, USA) was used in thin film fabrication Oxygen (research grade, 99.999%, Chemical & research laboratory supplier (CRLS) at University of New Mexico (UNM)) was used as reactive environment in a gas chamber, Nitrogen (99.999%, center for high technology materials (CHTM) facilities).were used as inert atmosphere and for fast drying applications.

2.1.2 Gold nanoparticles and semiconductor quantum dots

An aqueous solution of cetyltrimethylammonium bromide (CTAB) stabilized gold nanorods (AuNR) of different aspect ratio (L/w), A = 1.7, 2.2, 3.7 with w = 40 nm and L = 68, 88, 148 nm as well as A = 2.3, 2.8, 3.6 with w = 25 nm and L = 58, 70, 90 nm, were obtained from Nanopartz, Inc. Gold nanospheres (AuNS) of 40 nm diameter with citrate as a capping agent from was also purchased from Nanopartz, Inc. The aqueous suspensions

were used by 10 times dilution for dark-filed scattering of individual nanoparticles. For aggregated gold nanoparticles the gold nanoparticles were used by re-functionalization after removing excess surfactants. CdSSe/ZnS or CdSe/ZnS core/shell quantum dots (QD) consist of a monolayer of oleic acid coating in chloroform (10 mg/ml) with emission wavelength peak from 400 nm to 665 nm and having >50% quantum yield were obtained from Ocean NanoTech LLC, San Diego, CA and used as received.

2.1.3 Solvents

Solvents, ultrapure deionized (DI) water from water treatment plant at Center for High Technology materials (CHTM), the University of New Mexico (UNM), ethyl alcohol (200 proof, GR ACS, EMD Millipore corporation), acetone (Semiconductor grade, BDH), isopropyl alcohol (general laboratory grade, BDH), and toluene (general laboratory grade, BDH) were used as received, Methanol (GC-Mass grade) and chloroform (HPLC grade) were purchased from Sigma-Aldrich.

2.1.4 Materials

The substrates used were microscope glass cover slides (VWR micro cover glass, 22 mm x 22 mm), 2” silicon wafer (P-type prime grade SSP, University wafer) cut into appropriate size, 2” Oxide coated silicon wafer (type P/B, 100 mm, 300 nm wet thermal, orient <100>, SSP, 500 µm thick, University wafer) cut into appropriate size, 2”gold films (50 nm and 100 nm thick, cut into appropriate size) were fabricated by depositing gold on silicon substrate using electron beam evaporation and titanium (2 nm) as adhesion layer (**see method section**). All substrates were cleaned by sonication in ultrasonic bath (Branson ultrasonics corporation, 1800) in acetone, then isopropyl alcohol, and finally ultrapure DI water (for 5 min each) and dried under a nitrogen stream. Ultraviolet ozone treatment

(Novascan Technologies, Inc.) were used to remove any remaining organic materials on the surface of substrate and for surface activation. Standard orbital shaker (Henry Troemner LLC) was operated with gradual increase in speed to assist the assembly of individual gold nanoparticles on substrates by spreading solutions containing the nanoparticles. Langmuir-Blodgett (LB) trough (KSV NIMA) was used to fabricate semiconductor quantum dots (QD) and/or metal particle-QD composite thin films. Excess capping agents or ligands that are loosely attached to nanoparticle surfaces were removed by using VWR symphony 2421, ambient micro centrifuge. CV10Q1400F-Fusion-SP chemical resistance enhanced quartz cuvettes (Thorlabs) were used for absorption and fluorescence measurements.

A closed chamber with a gas inlet system (Warner Instruments Inc., RC-21B) was sealed by placing a bare coverslip on recessed grooves of the chamber from top side and sample containing coverslip (with the sample side facing upward) from bottom side. The chamber was used to control atmospheric condition (inert or reactive) and a length of tube in the outlet was used as a back pressure control to ensure smooth flow of gases in photochemical experiment (**section 2.2.3**). Water bubbler filled with ultrapure DI water was connect to the chamber to control the moisture content of the system.

2.2 Methods

2.2.1 Sample preparation for SERS Experiments

Generally two sample preparation methods have been employed in experimental surface enhanced Raman scattering (SERS) studies namely (1) Self-Assembled monolayer (SAM) on gold film before drop casting gold nanoparticles on top and (2) Functionalization of AuNR or AuNS with probe molecules and drop cast the particle-molecule complex on a substrate as shown by schematic diagram in **Figure 2.1** for each case.

SAM of molecules of interest were prepared on gold film by dipping the substrate (~10 mm x 10 mm or less) into dilute (15 μM) aqueous or ethanol solution of the probe dyes molecules such as MB, TH, AZA, AZB for at least 1 hr. Then 500 μL of colloidal AuNR was diluted to 2 ml and then excess surfactants were removed by centrifuge (at 5000 RPM for 5 min) and the residue was re-suspended in 1 ml of pure DI water and second round centrifuge was performed. Finally the residue was re-suspended in 200 μL of the solvent and the suspension was drop cast on top of the SAM and left dry at room temperature leaving behind solid thin film of gold nanorods (**Figure 2.1, left**).

In Functionalization of AuNR or AuNS with probe molecules**,** excess CTAB of AuNR or citrate of AuNS surfactants were removed once following same procedure described above. Then the AuNR or AuNS were re-suspended in 1 ml of solution of the probe molecules (aqueous or ethanol) for at least 1 h to ensure adsorption of the molecules on the gold nanoparticles. Unabsorbed excess molecules were removed through one round of centrifuge. The residue was suspended in 200 μL of pure solvent (water or ethanol) and drop cast on coverslip or oxide coated silicon wafer and dried at ambient condition (**Figure 2.1, right**).

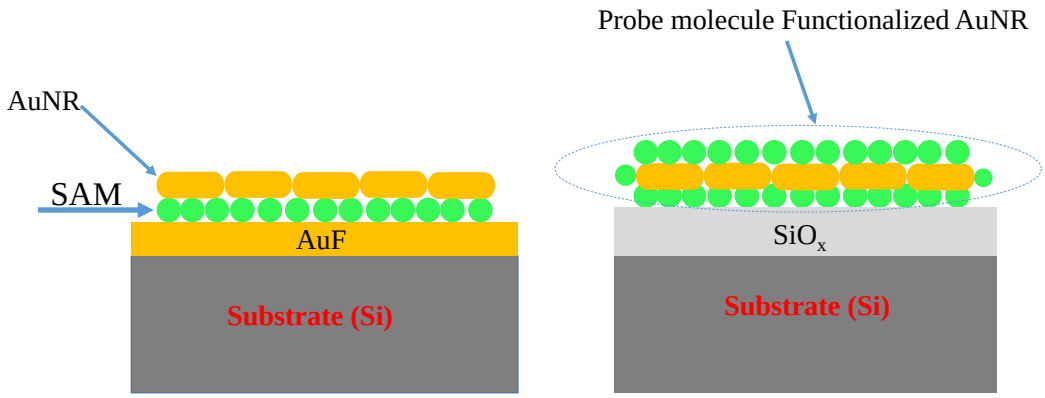

Figure 2.1 Schematic showing sample preparation scheme. (Left) AuNR deposited on SAM of molecules on gold film (right) probe molecule functionalized AuNR and deposited on oxide coated silicon wafer. Dimensions are not to scale.

To control the involvement of water in the SERS experiment, the above functionalization procedure was repeated for MB but this time with anhydrous ethanol as a solvent in each and every step. This procedure assists to remove coordinated water molecules from aggregates of AuNR-MB system.

2.2.2 Preparation of SAM Spacer between nanostructure and adsorbate

Ultrathin (less than 10 nm thick) gold film having a well-defined island structures (gold nanoisland (AuNI)) were evaporated on glass substrate using electron-beam evaporation method. At this thickness, the evaporation procedure inherently produces plasmonic nanostructures with broad resonances (**See next section**). The nanostructures were coated with a monolayer of poly(sodium 4-styrenesulfonate) (PSS) to yield spacer layer of about 1 nm between thin films of gold and MB. It was prepared by immersing the gold/substrate inside 2 mg/mL solution of PSS in 0.1 M aqueous solution of NaCl for 5 min. Then, PSS coated AuNI was incubated in 15 μM solution of MB in ethanol for overnight at room temperature. The film was then pulled out and rinsed thoroughly with ultrapure water and blown dry with nitrogen gas. Control sample was prepared by adsorbing MB directly on

AuNI from same solution under same condition. Schematic diagram showing this sample preparation technique is depicted in **Figure 2.2.**

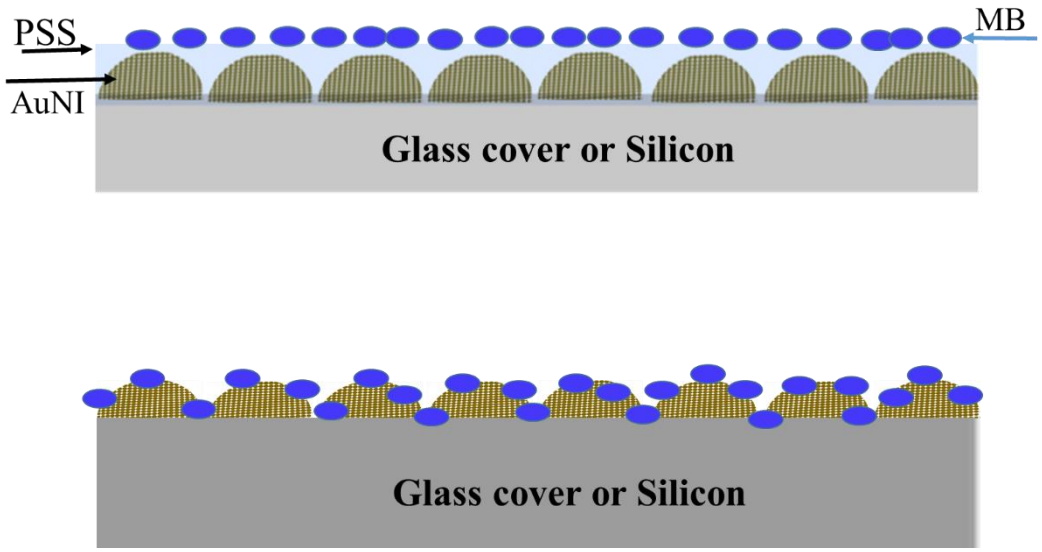

Figure 2.2 Schematic showing sample preparation scheme. (top) thin gold film containing gold nanoisland deposited on glass cove or silicon wafer and coated with PSS as spacer layer between AuNI and MB (bottom) same structure without a spacer layer (control sample). Dimensions are not to scale.

2.2.3 Surface enhanced Raman spectroscopy (SERS)

We used flexible open space optical set up for Raman and Photoluminescence (PL) measurements in Habteyes lab, at CHTM, UNM. Schematic diagram showing detailed optical paths in this experiment is depicted in **Figure 2.3**.

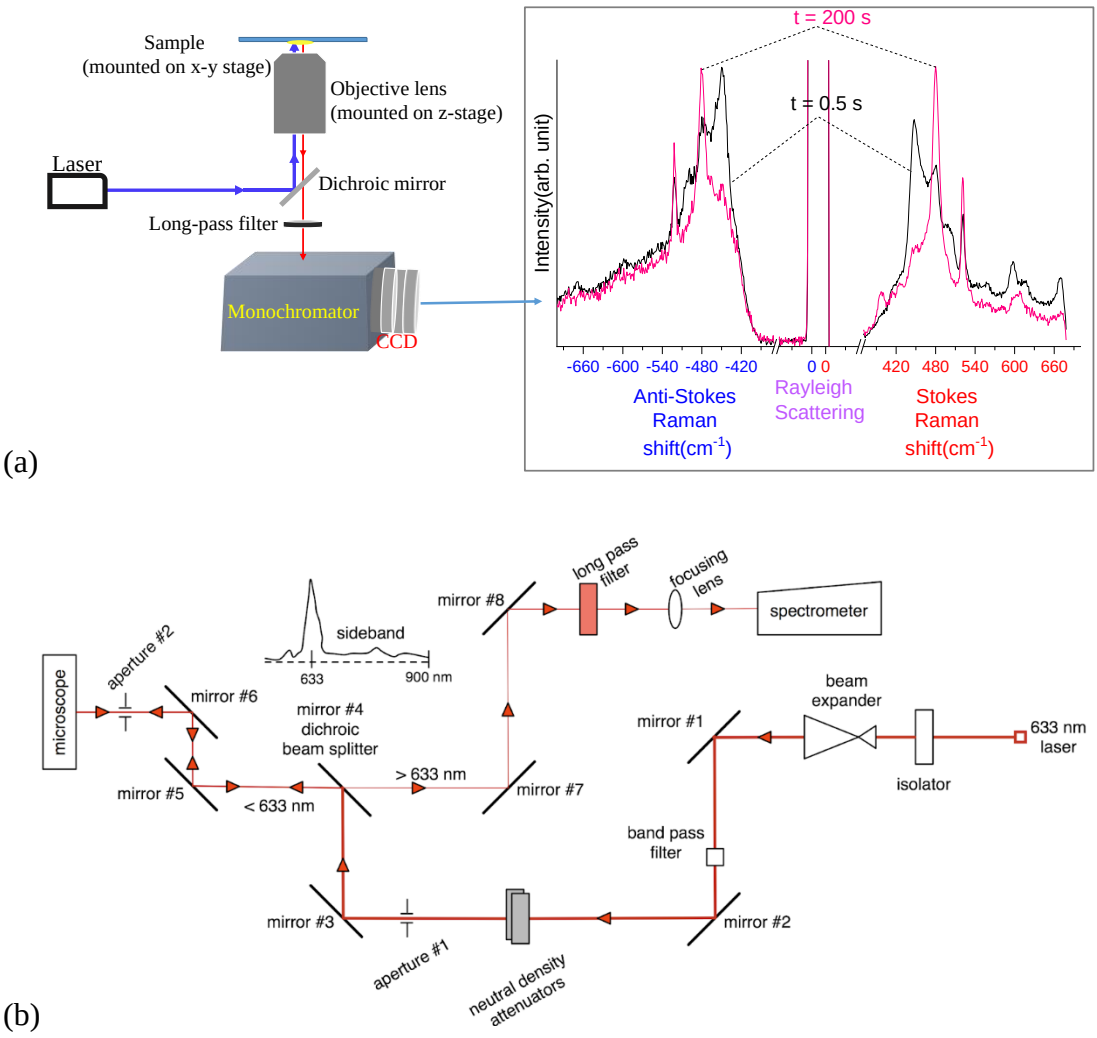

Figure 2.3 Schematic diagram showing optical set up for Raman and PL measurements (a) simplified outline from laser input to signal out (b) detailed optical paths and components

Visible (405 nm, 532 nm, 633 nm) and near IR (808 nm, 785 nm) lasers were used as an excitation sources. A collimated and linearly polarized light that has been attenuated to appropriate intensity is aligned by two apertures and directed to a microscope by optical mirrors and dichroic beam splitter. More than 90% of the light collected from the sample through microscope objectives is directed to the spectrometer (IsoPlane Spectrograph of Princeton Instruments) that uses thermoelectrically cooled (−75 °C) and back-illuminated deep depletion CCD camera via the same dichroic mirror and any remaining source light

was filter out by a long pass. The remaining (10%, see **Figure 2.5**) signal is directed to the Olympus UC30 camera that is attached to the microscope (Olympus GX51) for imaging the dark-field scattering of the sample. This optical setup allows us to obtain PL, Raman, and SERS data from a fixed area using the same objective by simply switching the excitation sources, while all of the other optical components and the sample remain stationary.

The comparison of Stokes and anti-Stokes Raman intensities was carried out using atomic force/near-field microscope as described in the schematic shown in **Figure 2.4**. Collimated laser beam was focused at the tip−sample junction using a parabolic mirror (numerical aperture, NA = 0.46) and scattered light was collected on the opposite side of the mirror by operating AFM to scan the sample while keeping the tip stationary. The laser line was screened by a notch filter and signals were directed to same spectrometer mentioned above for the detection of the Raman scattering (both Stokes and Anti-Stokes).

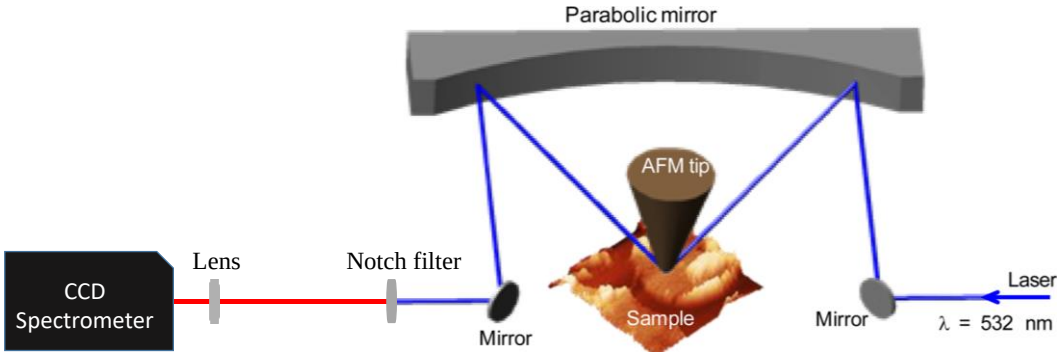

Figure 2.4 Schematic showing the experimental setup for Stokes and Anti-Stokes Raman Scattering measurements

2.2.4 Dark-field scattering measurement**.**

The dark-field scattering measurement was performed using the GX51 Olympus microscope. The optical layout is shown in the schematic in **Figure 2.5**. The sample is

excited with 100W halogen lamp white light source. Dark-field scattering images of the individual nanoparticles or aggregates were obtained by directing about 10% of the signal to the camera (Olympus UC30) that is attached to the microscope. The corresponding scattering spectra were then recorded by centering the particle of interest to the focus of the objective, and directing about 90% of the light collected from the sample to spectrometer (IsoPlane Spectrograph of Princeton Instruments), which uses a thermoelectrically cooled (-75 ^{o}C) and back-illuminated deep depletion CCD camera.

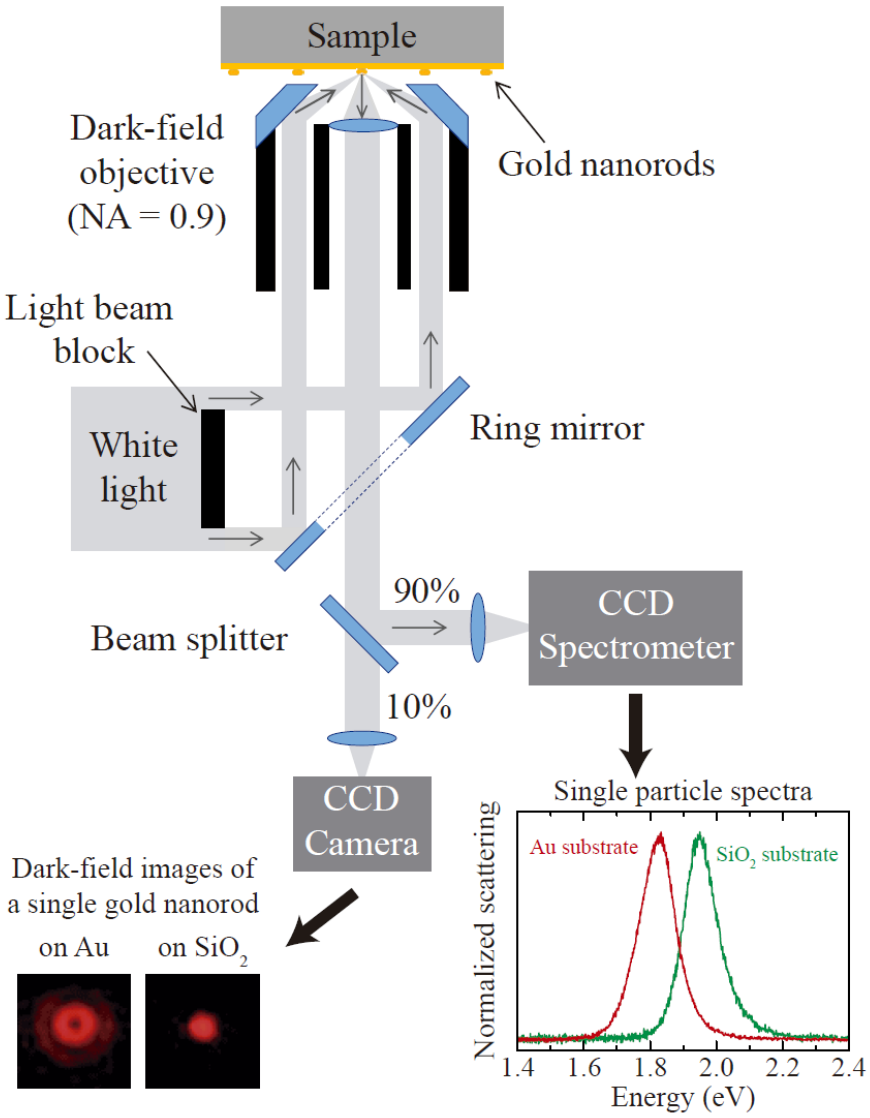

Figure 2.5 Schematic showing the dark-field scattering microscopy and spectroscopy experimental setup.

2.2.5 UV-Visible Spectroscopic Measurements

Double beam UV-Vis absorption data were obtained on a Shimadzu UV-2450 spectrophotometer. Sub-monolayer dye was adsorbed on the ultrathin gold film from a dilute solution of analytes (100-220 µM) by carefully bringing the gold film coated side of the quartz cuvette vertically with the aid of mechanical stage until it just touches the surface of the solution. Then the system is covered with aluminum foil and incubated for a period

of 1-60 min.at room temperature. Absorption spectra at normal incidence of bare ultrathin gold film (AuNI) and those coated with molecules (AuNI-M) were measured using a conventional Shimadzu UV-2450 Ultraviolet-Visible spectrophotometer. In this experiment, baseline was acquired with both reference and sample cells empty. Then the absorbance of Au film was obtained by placing a one side Au film coated quartz cuvette in the sample cell, while keeping the reference cell empty. The sample cuvette was taken out and Au film coated side of the cuvette was incubated with the analyte solution for a fixed time, then dried and placed back in spectrometer to measure the absorbance of analyte coated Au film under the same measurement parameters. In the case absorption measurement for a solution, a quartz cuvette (1400 µL) filled with solvent (water or ethanol) was used as reference.

2.2.6 Thin film fabrication techniques and synthesis of gold nanorods

2.2.6.1 Electron beam metal evaporation and deposition

Ultrathin metal films were deposited on a clean substrates at a rate of 0.2 Å/sec to a nominal thickness of 1-20 nm using electron beam evaporation technique at a chamber pressure of 1-2 x 10^{-7} Torr. The film mass thickness (nominal thickness) and deposition rate were monitored by using a quartz crystal microbalance and the films were used without thermal annealing.

2.2.6.2 Langmuir-Blodgett technique to prepare quantum dot thin films

Dry and clean oxide coated silicon wafer or cover glass was obtained following the cleaning procedures described above and subjected to ultraviolet ozone treatment. Then it was immersed vertically in ultrapure DI water subphase in Langmuir-Blodgett (LB) trough to a pre-programmed height and let the water surface clean and stable. A 10 mg/ml solution

of quantum dots in a chloroform was gently applied to the water surface using Hamiltonian microliter syringe and was allowed to stabilize for different duration depending on the target exposure time of the QDs to the water surface. The film was then compressed at a typical speed of 10 mm/min until a target pressure of 20−40 mN/m was attained. The compressed film was stabilized for about 5 min and transferred to a substrate as it move automatically out of the subphase at a speed of 5 mm/min and compressed to a constant surface pressure.

2.2.6.3 CTAB capped Seed mediated Synthesis of Gold Nanorods

1. **Preparation of Seed Solution**[1]

Seed solution for AuNRs was prepared following standard procedures elsewhere.[2,3] Briefly, a 5 mL 0.5 mM $HAuCl_4$ was mixed with 5 mL of 0.2 M CTAB solution. Then, a 0.6 mL portion of fresh 0.01 M $NaBH_4$ was diluted to 1 mL with water and then injected into the Au (III)-CTAB solution under vigorous stirring (1200 rpm). The solution color was changed from yellow to brownish-yellow, and the stirring was stopped after 2 min. The seed solution was aged at room temperature for 30 min before use.

2. **Preparation of Growth Solution A: CTAB-Sodium Salicylate-$HAuCl_4$**

To prepare the growth solution, 9.0 g of CTAB together with 0.8 g (0.010 M) sodium salicylate were dissolved in 250 mL of warm water (50 ^oC) in a 500 mL Erlenmeyer flask. The solution was allowed to cool to 30 ^oC and 6 ml of 4 mM $AgNO_3$ solution was added. The mixture was kept undisturbed at 30 ^oC for 15 min, after which 250 mL of 1 mM $HAuCl_4$ solution is added. After 15 min of slow stirring (400 rpm), 1 mL of 0.064 M ascorbic acid is added, and the solution is vigorously stirred for 30 s until it becomes

colorless. The growth solution has a CTAB concentration of about 0.05 M and was used right after preparation.

3. **Preparation of Growth Solution B: CTAB-Salicylic acid-$HAuCl_4$**

The author followed same procedure that has been described in part 2 above. To this end, 9.0 g of CTAB together with 0.8 g (0.010 M) salicylic acid were dissolved in 250 mL of warm water (70 ^oC) in a 500 mL Erlenmeyer flask. The solution was allowed to cool to 30 ^oC and 12 ml of 4 mM $AgNO_3$ solution was added. The mixture was kept undisturbed at 30 ^oC for 15 min, after which 250 mL of 1 mM $HAuCl_4$ solution was added. After 15 min of slow stirring (400 rpm), 2 mL of 0.064 M ascorbic acid was added, and the solution was vigorously stirred for 30 s until it become colorless. The growth solution has a CTAB concentration of about 0.05 M and used right after preparation.

4. **Growth of Gold Nanorods**

Finally, 0.8 mL of seed solution was injected into the growth solution. The resultant mixture was stirred for 30 s and left undisturbed at 30 ^oC for 12 h for nanorods growth. The reaction products were isolated by centrifugation at 8500 rpm for 25 min followed by removal of the supernatant. The precipitates were re-dispersed in 10 mL of water.

2.2.6.4 Template stripping of AuF

Two component, part A (colorless) and part B (amber) EPO-KET377 (fiber optics grade epoxy) was purchased from Epoxy technology Inc. The components were mixed in 1:1 ratio by mass and mixed thoroughly with continuous stirring using glass rod or metal spatula to obtain homogenous mixture. A drop of the mixed glue was applied on 100 nm thick gold film on silicon wafer. The gold film was deposited on the wafer by using electron-beam evaporation technique at rate of 1 Å/s at base pressure of ~7.0 x 10^{-7} mbar.

Then clean silicon wafer cut into 10 mm x 10 mm was placed on top and the glue was cured for 1 hour at 150 ^{o}C. After cooling, the top silicon substrates are gently pushed-off, and substrates are thereby stripped off, with Au adhering to the glue and the small silicon wafer.

2.2.6.5 Atomic layer deposition (ALD) of Al_2O_3 dielectric spacer

Al_2O_3 film is deposited on the Au film using the atomic layer deposition (ALD system of Picosun. Trimethylaluminium (TMA) and H_2O vapors are pulsed alternately through the reaction chamber utilizing N_2 as carrier gas at a flow rate of 150 cm^3/min and 200 cm^3/min for TMA and H_2O respectively. The pressure inside the reaction chamber is 4 Torr with the growth temperature of 100 ^{0}C. TMA reactant exposure time (pulse time) is 0.5 s and N_2 purge following TMA exposure time is 10 s. H_2O reactant exposure time is 0.7 s and N_2 purge following H_2O exposure time is 20 s for Al_2O_3 growth on Au film. Long purge time are necessary at low temperature to prevent chemical vapor deposition of Al_2O_3.[4] This growth temperature and pulse/purge time for TMA and H_2O has been optimized carefully, since uniform and conformal deposition of Al_2O_3 bellow sub-nanometer length scale is challenging. TMA and H_2O yield ALD Al_2O_3 growth according to the following two half-reactions (A) and (B).

$$AlOH^* + Al(CH_3)_3 \rightarrow AlOAl(CH_3)_2^* + CH_4 \quad (A)$$

$$AlCH_3^* + H_2O \rightarrow AlOH^* + CH_4 \quad (B)$$

The * in above reaction denotes the surface species and the steps repeats as ABAB to form for ALD Al_2O_3 via self- limiting surface reactions.[5, 6]

2.2.7 Structural Characterization

Atomic force microscope (AFM).

Atomic force microscope (AFM) images were recorded in air using Neaspec-GmbH instrument operated in a tapping mode with tapping amplitude ≈50 nm near the resonance oscillation frequency of the cantilever. The cantilevers used were NCHR series of standard and supersharp silicon (Nanoworld, NanoAndmore, USA), with a resonance frequency of 250-390 kHz and an average tip radius of $\leq$ 5 nm and $\leq$ 12 nm respectively, for super sharp and standard AFM tip.

Scanning electron microscope (SEM)

Scanning electron microscope (SEM) images were obtained using Quanta 3D FEG scanning electron microscope with regular ion-beam imaging using SE detector with high resolution at 5-30 kV.

Transmission electron microscope (TEM). High resolution TEM (HRTEM) images will be taken on a JEOL 2010F microscope operating at acceleration voltage of 200kV and beam source was Schottky field emission gun (zirconated tungsten). It has point to point resolution of 0.19 nm and lattice resolution of 0.14 nm. The scanning TEM resolution was 0.17 nm (HAADF detector).

Apertureless (scattering type) near-field scanning optical microscope (ANSOM). The basic principle of ANSOM imaging involves focusing external laser light at the tip of atomic force microscope (AFM) probe and measuring the scattered light as the sample is raster scanned in close proximity to the tip. For a given sample and AFM operating parameters, the nature and strength of the probe-sample interaction depends on (1) the radius of curvature of the probe tip (2) the material properties of the probe (3) the polarization of the excitation light with respect to the probe axis and (4) the wavelength of the excitation light.[7] The detail of experimental procedure of near-field setup are available

elsewhere.[7-11] Briefly, we used Neaspec GmbH near-field setup that is based on tapping mode atomic force microscope and pseudo-heterodyne interferometer. The AFM probe oscillates with tapping amplitude ~50 nm above the sample surface near the natural resonance oscillation frequency (Ω ~250 kHz) of the cantilever. Linearly polarized radiation from a HeNe laser (633 nm, Thorlabs) or a mid-IR quantum cascade laser (6 and 10 μm, MIRCat-1200, DAYLIGHT SOLUTION) is directed and focused onto the tip-sample junction with an angle of 30° with respect to the sample by using a parabolic mirror (NA = 0.46). A simplified schematic diagram of the experimental setup with mid-IR laser source is depicted in **Figure 2.6**.The scattered visible light plus reference beam is detected using a silicon photodiode (New Focus, Model 2051), whereas the corresponding mid-IR signals were detected by HgCdTe photodiodes (Kolmar Technologies, Inc). The output of the detector is demodulated at $n\Omega$, and the optical images obtained at $n \geq 2$ we used for image analysis. The near-field optical amplitude and optical phase as well as AFM topography images are acquired simultaneously by raster-scanning the sample stage and recording the near-field scattering and the height information as a function of the sample position.

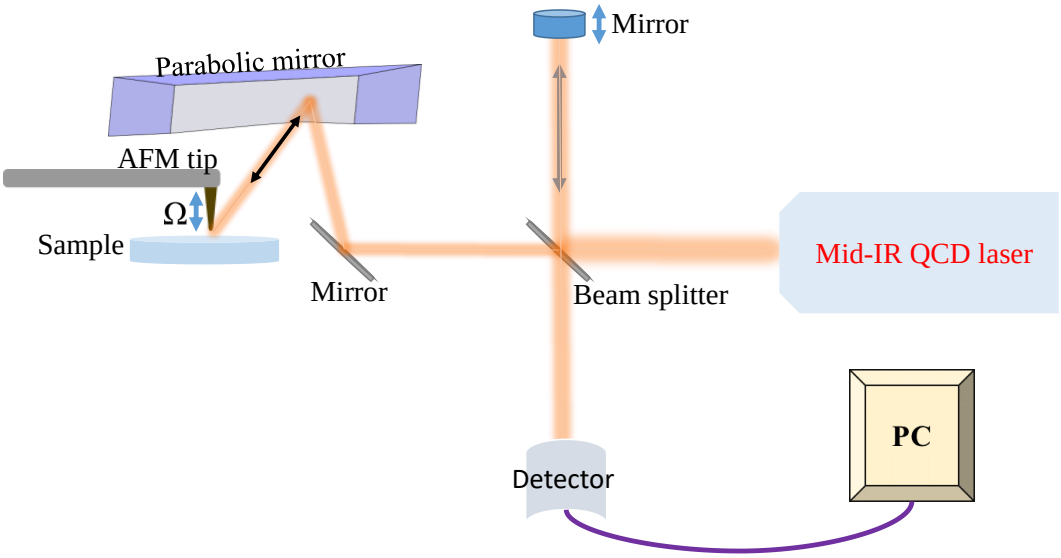

Figure 2.6 Schematic diagram (not to scale) for ANSOM set up

2.3 Background

2.3.1 Photophysics and photochemistry of phenothiazinium dyes

Methylene blue and its N-demethylated derivate (**Scheme 1**) are cationic dyes that belong to phenothiazinium class of compounds.[12] The characteristic colors of these compounds are caused by the strong absorption band in the 550—700 nm region, which contrasts with the weak absorption band to the blue and red side of this range. The absorption band moves progressively to longer wavelengths with increasing degree of methylation (**Figure 2.7**a). The appearance of a shoulder at a higher energy side of the principal absorption band is associated with a vibronic sideband of the dye monomers.[13] An aqueous solution of these dyes tends to aggregate to form face-to-face or H-aggregates.[14] For example, aggregates of MB (dimer or oligomer) form in solution, which are easily identified by their blue-shifted (hypsochromic) absorption compared with their monomer components.[15-17] The room temperature equilibrium constant of dimerization of MB is reported to be ~3.8×10^3 M^{-1} in water.[18] The dimer has a visible absorption band about 80 nm to shorter wavelengths than

the monomer. MB monomer has a maximum at 664 nm (**Figure 2.7**a) and dimer at 585 nm (**Figure 2.7**b). Reports indicate that the aggregation of MB and its N-demethylation derivatives are facilitated by biological substrates (DNA, RNA, etc) and negatively charged interfaces.[19]

Depending on the nature of the ground state (monomer versus dimer), the photochemical properties of MB can be shifted from a Type II (energy transfer to oxygen forming singlet oxygen) to a Type I mechanism (electron transfer forming the semi-reduced and the semi-oxidized radicals of MB). These photophysical and photochemical behaviors make these dyes an ideal choice for photosensitizers as a drug in photodynamic therapy[20-23] and energy conversion applications.[20, 24-26]

Scheme 1Chemical structure of MB and its demethylation derivative

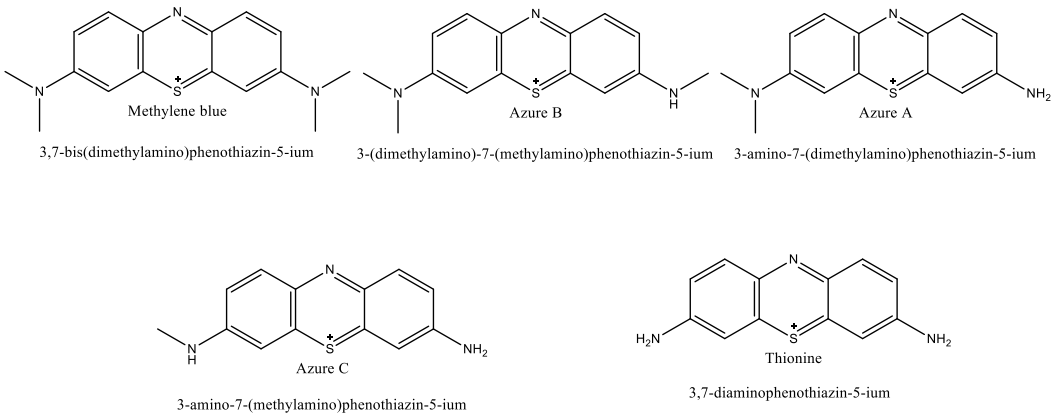

Phenothiazinium dyes of the above type all give fluorescence with low quantum yield and the lifetime of MB and TH are reported to fall in the range of 330-390 ps.[27, 28] The lifetimes of the triplet state of MB in aqueous solution are typically in the microsecond regime and its lifetime increase with pH due to greater basicity of the excited state compared to its ground state. Non-protonated form of MB is the stable ground state species under most

conditions, as its protonation does not take place unless in strongly acidic solutions.[29] Solute-solvent interaction and solvents dielectric constant play a significant role in modulating the lifetime of the singlet and triplet excited states of the phenothiazine dyes which can be inferred from their low fluorescence quantum yield.[24]

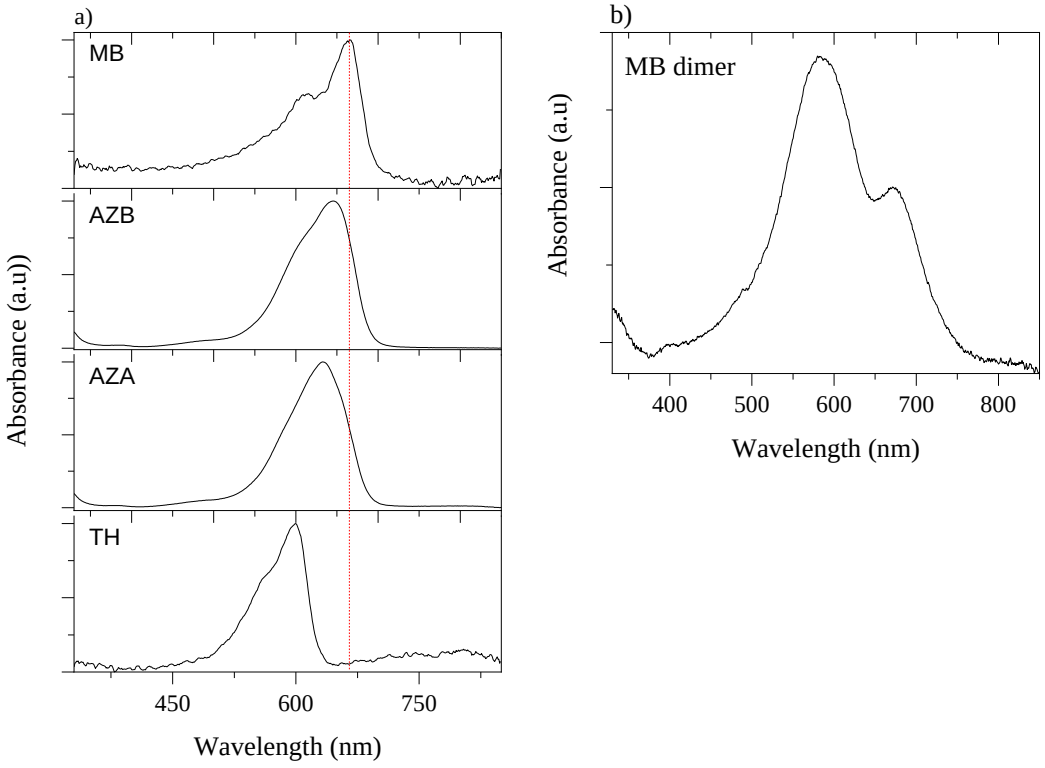

Figure 2.7 (a) absorption spectra of 15 µM aqueous solution of MB, AZB, AZA, and TH (b) absorption spectrum of a thin film of MB on a cover glass

The 664 nm (n, π*) MB singlet state relaxes with an intersystem crossing (ISC) rate of 3 x 10^9 s^{-1} to the lowest triplet state. The triplet states are efficiently quenched with oxygen molecules via the energy transfer pathway forming $^1\Delta_g$ O_2 with a quantum yield of 0.5 pH. Similar data are reported for other dyes in this family.[30] Absorption, fluorescence, and redox properties of these dyes are summarized in **Table 1**.

Table 1 Absorption, fluorescence and redox properties of phenothiazinium dyes[12]

Dye	λ_{max} (abs.)	ε_{max} (M^{-1} cm^{-1})	λ_{max} (fluor.)	E^o_{gs}(V)	ΔE_{ss} (eV)	E^o_{ss} (V)	ΔE_{ts} (eV)	E^o_{ts} (V)
MB	664 nm	81600	685 nm	0.04	1.83	1.87	1.44	1.48
AZB	647 nm	78000	675 nm	0.05	1.90	1.95		
AZA	633 nm	75000	660 nm	0.05	1.92	1.97		
AZC	616 nm	73000	645 nm	0.05	1.97	2.02		
TH	598 nm	71000	623 nm	0.05	2.03	2.08	1.69	1.74

NB. All potentials in volts vs. NHE

.

In addition to the energy transfer (type II photochemical pathway), Electron transfer quenching (type I) of the triplet state MB and its analogs have been through reviewed by Tuite and Kelly[12] and the references in there.[31] The equations (1) up to (4) below outline the different types of quenching exhibited by the triplet excited states of MB. Based on redox properties indicated in **Table 1,** other dyes are also believed to undergo a similar type of photophysical processes**.**

$$^3MB + Q \rightarrow {}^3[MB\ldots Q] \quad (1)$$

$$^3[MB\ldots Q] \rightarrow {}^{3,1}[MB^{-}\cdot\ldots Q\cdot^{+}] \quad (2)$$

$$^{3,1}[MB^{-}\cdot\ldots Q\cdot^{+}] \rightarrow MB + Q \quad (3)$$

$$^{3,1}[MB^{-}\cdot\ldots Q\cdot^{+}] \rightarrow MB^{-}\cdot + Q\cdot^{+} \quad (4)$$

2.3.2 Surface-enhanced Raman Spectroscopy (SERS)

We used the SERS methods for studying the photochemical transformation of methylene blue into sequential N-demethylation products. The method involves the coupling of a monolayer of phenothiazinium dyes with plasmonic metal nanoparticles that sustain

intense plasmon resonances upon excitation with visible light. Because of the unique properties (will be discussed in the next section) associated with their shape AuNRs, we obtained enormous amplification of the spectroscopic signature of the molecules coupled and makes the method ultrasensitive to follow the photochemical transformations.

Vibrational spectroscopy has been used to complement fluorescent measurements in spectroscopic characterization of molecular systems[32] because the later has an inherent limitation in providing detailed molecular information and it suffers from photobleaching unless employed at low temperature. In contrast, Raman spectroscopy is capable of providing a detailed vibrational signature of molecules and rapid photobleaching problem is relatively insignificant. However, Raman cross-section is approximately 14-15 orders of magnitudes smaller than fluorescence cross-section per molecule and this makes the method inefficient. Therefore, it requires the amplification of the Raman signal by same order magnitude of to utilize ultrasensitive spectroscopic characterization of molecules down to single-molecule detection.[33] Surface-enhanced Raman Scattering, which was discovered in 1970's was used to overcome by amplifying the scattering signals via electromagnetic or a combination of chemical (electronic) and electromagnetic enhancement mechanisms. This will be described in detail in **section 2.3.3.**

2.3.3 Origin of electromagnetic enhancement mechanism in SERS[34]

Electromagnetic enhancement in SERS originates from the excitation of the collective oscillation of conduction electrons of a metallic nanostructure with an electromagnetic field. This excitation is called a surface plasmon. Two different types of surface plasmon can form under the influence of the external field namely localized surface plasmon resonance (LSPR) and surface plasmon polariton (SPP). LSPRs are excitation due to

oscillation of conduction electrons of finite nanostructures coupled to electromagnetic field whereas SPPs are excitations of conduction electrons in an extended 2D structure that results in the propagation of waves at the metal-insulator interface. LSPRs are applied mainly for SERS, enhanced absorption, as well as fluorescence and it will be the major emphasis of this dissertation.

Metals are characterized by the dielectric function of a free electron gas model, also known as the plasma model. The plasma frequency (ω_p) derived from a classical Maxwell theory is related to the complex dielectric function ($\varepsilon(\omega)$) of the free electron gas using a model called the Drude model.

$$\varepsilon(\omega) = 1 - \frac{\omega_p^2}{(\omega^2 + i\gamma\omega)}$$

The quantity γ in the denominator is the damping frequency of electron collision. For noble metals (Cu, Ag, and Au) expression that takes into account of the bound electrons of the metals given by:

$$\varepsilon(\omega) = \varepsilon_\infty - \frac{\omega_p^2}{(\omega^2 + i\gamma\omega)}$$

Gold and silver are the most important metals for plasmonic studies in the visible and near-infrared. The LSPR of the nanoparticles of these metals falls into the visible region of the electromagnetic spectrum. A striking consequence of this is the bright colors exhibited by particles both in transmitted and reflected light, due to resonantly enhanced absorption and scattering. This effect has found applications for many hundreds of years, for example in the staining of glass for windows or ornamental cups

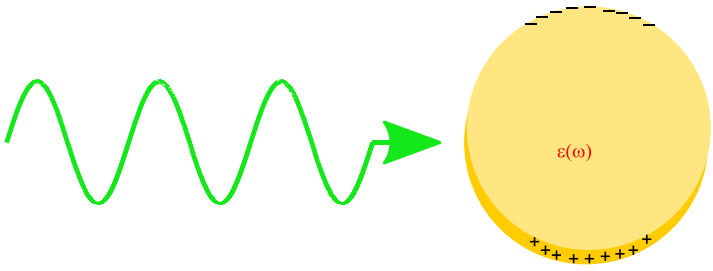

Figure 2.8 Schematic of the spherical gold nanoparticle placed in an external electric field

The dipole moment **p** induced by applied field ($\mathbf{E_o}$) is given by the expression:

$$\boldsymbol{p} = 4\pi\varepsilon_o\varepsilon_m a^3 \frac{\varepsilon - \varepsilon_m}{\varepsilon + 2\varepsilon_m}\boldsymbol{E_0}$$

The quantities ε_o, ε_m, and *a* are vacuum permittivity, a dielectric constant of the surrounding medium, and radius of the spherical metal particle respectively. If we introduce polarizability α, so that $\boldsymbol{p} = \varepsilon_o\varepsilon_m\boldsymbol{\alpha E_0}$, then, we obtain:

$$\alpha = 4\pi a^3 \frac{\varepsilon - \varepsilon_m}{\varepsilon + 2\varepsilon_m}$$

The polarizability experiences a resonance enhancement under the condition that $|\varepsilon + 2\varepsilon_m|$ is a minimum. Metals have generally small or slowly varying Im[ε] and large negative the condition of resonance met at Re [ε(ω)] =-2ε_m. The consequence of the resonantly enhanced polarization α is a concomitant enhancement in the efficiency with which a metal nanoparticle scatters and absorbs light. The absorption cross-section (C_{abs}), scattering cross-section (C_{sca}), and extinction cross-section (C_{ext}) are given by the following expressions respectively, and with k = 2π/λ

$$C_{abs} = kIm[\alpha] = 4\pi k a^3 Im[\tfrac{\varepsilon-\varepsilon_m}{\varepsilon+2\varepsilon_m}]$$

$$C_{sca} = \frac{k^4}{6\pi}|\alpha|^2 = \frac{8\pi}{3}k^4a^6|\frac{\varepsilon - \varepsilon_m}{\varepsilon + 2\varepsilon_m}|^2$$

$$C_{ext} = C_{abs} + C_{sca}$$

For a sphere of volume *V* and dielectric function $\varepsilon = \varepsilon_1 + i\varepsilon_2$ in the quasi-static limit, the explicit expression for the extinction cross-section is

$$C_{ext} = 9\frac{\omega}{c}\varepsilon_m^{3/2}V\frac{\varepsilon_2}{[\varepsilon_1 + 2\varepsilon_m]^2 + \varepsilon_2^2}$$

Another effect of this process is the confinement fields to the region well below the diffraction limit and hence the enhancement of electromagnetic (EM) at metal /dielectric interfaces.[35, 36]

2.4 References

1. Ye, X. et al. Improved Size-Tunable Synthesis of Monodisperse Gold Nanorods through the Use of Aromatic Additives. *ACS Nano* **6**, 2804-2817 (2012).

2. Nikoobakht, B. & El-Sayed, M.A. Preparation and Growth Mechanism of Gold Nanorods (NRs) Using Seed-Mediated Growth Method. *Chemistry of Materials* **15**, 1957-1962 (2003).

3. Smith, D.K. & Korgel, B.A. The Importance of the CTAB Surfactant on the Colloidal Seed-Mediated Synthesis of Gold Nanorods. *Langmuir* **24**, 644-649 (2008).

4. Groner, M.D., Fabreguette, F.H., Elam, J.W. & George, S.M. Low-Temperature Al2O3 Atomic Layer Deposition. *Chemistry of Materials* **16**, 639-645 (2004).

5. Su, K.H. et al. Interparticle Coupling Effects on Plasmon Resonances of Nanogold Particles. *Nano Letters* **3**, 1087-1090 (2003).

6. Funston, A.M., Novo, C., Davis, T.J. & Mulvaney, P. Plasmon Coupling of Gold Nanorods at Short Distances and in Different Geometries. *Nano Letters* **9**, 1651-1658 (2009).

7. Habteyes, T.G., Dhuey, S., Kiesow, K.I. & Vold, A. Probe-sample optical interaction: size and wavelength dependence in localized plasmon near-field imaging. *Optics Express* **21**, 21607-21617 (2013).

8. Kim, Z.H., Liu, B. & Leone, S.R. Nanometer-Scale Optical Imaging of Epitaxially Grown GaN and InN Islands Using Apertureless Near-Field Microscopy. *The Journal of Physical Chemistry B* **109**, 8503-8508 (2005).

9. Kim, Z.H. & Leone, S.R. High-Resolution Apertureless Near-Field Optical Imaging Using Gold Nanosphere Probes. *The Journal of Physical Chemistry B* **110**, 19804-19809 (2006).

10. Ocelic, N., Huber, A. & Hillenbrand, R. Pseudoheterodyne detection for background-free near-field spectroscopy. *Applied Physics Letters* **89**, 101124 (2006).

11. Kim, Z.H. & Leone, S.R. Polarization-selective mapping of near-field intensity and phase around gold nanoparticles using apertureless near-field microscopy. *Optics Express* **16**, 1733-1741 (2008).

12. Tuite, E.M. & Kelly, J.M. New trends in photobiology: Photochemical interactions of methylene blue and analogues with DNA and other biological substrates. *Journal of Photochemistry and Photobiology B: Biology* **21**, 103-124 (1993).

13. Dean, J.C. et al. Broadband Transient Absorption and Two-Dimensional Electronic Spectroscopy of Methylene Blue. *The Journal of Physical Chemistry A* **119**, 9098-9108 (2015).

14. Dean, J.C., Oblinsky, D.G., Rafiq, S. & Scholes, G.D. Methylene Blue Exciton States Steer Nonradiative Relaxation: Ultrafast Spectroscopy of Methylene Blue Dimer. *The Journal of Physical Chemistry B* **120**, 440-454 (2016).

15. Morgounova, E., Shao, Q., Hackel, B., Thomas, D. & Ashkenazi, S. Photoacoustic lifetime contrast between methylene blue monomers and self-quenched dimers as a model for dual-labeled activatable probes. *Journal of Biomedical Optics* **18**, 056004 (2013).

16. Patil, K., Pawar, R. & Talap, P. Self-aggregation of Methylene Blue in aqueous medium and aqueous solutions of Bu4NBr and urea. *Physical Chemistry Chemical Physics* **2**, 4313-4317 (2000).

17. Heger, D., Jirkovsk, J. & Kln, P. Aggregation of Methylene Blue in Frozen Aqueous Solutions Studied by Absorption Spectroscopy. *The Journal of Physical Chemistry A* **109**, 6702-6709 (2005).

18. Bergmann, K. & O'Konski, C.T. A SPECTROSCOPIC STUDY OF METHYLENE BLUE MONOMER, DIMER, AND COMPLEXES WITH MONTMORILLONITE. *The Journal of Physical Chemistry* **67**, 2169-2177 (1963).

19. Junqueira, H.C., Severino, D., Dias, L.G., Gugliotti, M.S. & Baptista, M.S. Modulation of methylene blue photochemical properties based on adsorption at aqueous micelle interfaces. *Physical Chemistry Chemical Physics* **4**, 2320-2328 (2002).

20. Agnez-Lima, L.F., Mascio, P.D., Napolitano, R.L., Fuchs, R.P. & Menck, C.F.M. Mutation Spectrum Induced by Singlet Oxygen in Escherichia coli Deficient in Exonuclease III. *Photochemistry and Photobiology* **70**, 505-511 (1999).

21. Severino, D., Junqueira, H.C., Gugliotti, M., Gabrielli, D.S. & Baptista, M.S. Influence of Negatively Charged Interfaces on the Ground and Excited State Properties of Methylene Blue ¶. *Photochemistry and Photobiology* **77**, 459-468 (2003).

22. Tardivo, J.P. et al. Methylene blue in photodynamic therapy: From basic mechanisms to clinical applications. *Photodiagnosis and Photodynamic Therapy* **2**, 175-191 (2005).

23. Danziger, R.M., Bar-Eli, K.H. & Weiss, K. The laser photolysis of methylene blue. *The Journal of Physical Chemistry* **71**, 2633-2640 (1967).

24. Ravanat, J.-L. et al. Damage to Isolated DNA Mediated by Singlet Oxygen. *Helvetica Chimica Acta* **84**, 3702-3709 (2001).

25. Harmatz, D. & Blauer, G. REACTIONS OF PHOTOEXCITED METHYLENE BLUE. *Photochemistry and Photobiology* **38**, 385-387 (1983).

26. NILSSON, R., MERKEL, P.B. & KEARNS, D.R. KINETIC PROPERTIES OF THE TRIPLET STATES OF METHYLENE BLUE AND OTHER PHOTOSENSITIZING DYES. *Photochemistry and Photobiology* **16**, 109-116 (1972).

27. Yamazaki, I., Tamai, N., Kume, H., Tsuchiya, H. & Oba, K. Microchannel-plate photomultiplier applicability to the time-correlated photon-counting method. *Review of Scientific Instruments* **56**, 1187-1194 (1985).

28. Beddard, G.S., Kelly, J.M. & van der Putten, W.J.M. Picosecond study of the luminescence and transient absorption of methylene blue–polynucleotide complexes. *Journal of the Chemical Society, Chemical Communications*, 1346-1347 (1990).

29. Acemioğlu, B., Arık, M., Efeoğlu, H. & Onganer, Y. Solvent effect on the ground and excited state dipole moments of fluorescein. *Journal of Molecular Structure: THEOCHEM* **548**, 165-171 (2001).

30. Chen, J., Cesario, T.C. & Rentzepis, P.M. Time resolved spectroscopic studies of methylene blue and phenothiazine derivatives used for bacteria inactivation. *Chemical Physics Letters* **498**, 81-85 (2010).

31. Ohno, T. & Lichtin, N.N. Mechanistic aspects of the quenching of triplet methylene blue by organic reductants. *The Journal of Physical Chemistry* **86**, 354-360 (1982).

32. Nie, S. & Emory, S.R. Probing Single Molecules and Single Nanoparticles by Surface-Enhanced Raman Scattering. *Science* **275**, 1102-1106 (1997).

33. Kleinman, S.L. et al. Single-Molecule Surface-Enhanced Raman Spectroscopy of Crystal Violet Isotopologues: Theory and Experiment. *Journal of the American Chemical Society* **133**, 4115-4122 (2011).

34. <Plasmonics _Fundamentals and application.pdf>.

35. Kreibig, U. & Vollmer, M. in Optical Properties of Metal Clusters 13-201 (Springer Berlin Heidelberg, Berlin, Heidelberg, 1995).

36. Kolwas, K. Decay Dynamics of Localized Surface Plasmons: Damping of Coherences and Populations of the Oscillatory Plasmon Modes. *Plasmonics* **14**, 1629-1637 (2019).

Chapter Three

3 Plasmon Enhanced Resonant Excitation and Demethylation of Methylene Blue[1]

3.1 Abstract

Using methylene blue (MB) as model system, we demonstrated surface plasmon-enhanced resonant excitation that leads to N-demethylation reaction under visible light (λ= 633 nm) illumination at low photon flux. The chemical changes are monitored by detecting the vibrational signatures of the reactant and product species in situ using surface-enhanced Raman scattering (SERS) spectroscopy. The SERS vibrational spectra acquired immediately after laser illumination are the same as the Raman spectrum of MB solid powder, whereas the spectra recorded few seconds later are remarkably similar to that of thionine solid powder, indicating complete N-demethylation of MB to form thionine (TH). However, resonant excitation of MB adsorbed on non-plasmonic surfaces and excitations of plasmon resonance at 532 and 808 nm lasers that do not overlap with molecular resonance of MB cannot yield complete N-demethylation. The mechanism of this photochemical transformation strongly depends on electronic excitation of adsorbate molecules that are pumped by strong field concentrated by metal nanoparticle via excitation of surface plasmon resonance. Both MB and TH give strong SERS signals due to combination of electronic and electromagnetic enhancement effects and make them a

[1] This Chapter is adapted from **Tesema T. E**.; Kafle, B.; Tadesse M. G, Habteyes, T. G., *The Journal of Physical Chemistry C* **2017,** 121, (13), 7421-7428

convenient model system for ultra-sensitivity application and for future mechanistic studies.

3.2 Introduction

Soon after the discovery of surface enhanced Raman scattering (SERS) spectroscopy[1, 2], surface enhanced photochemistry was proposed theoretically[3, 4] and demonstrated experimentally[5-11]. In particular, the work by Moskovits and co-workers revealed the ambiguity in the interpretations of earlier SERS data due to vibrational peaks of reaction products that could be wrongly assigned to the reactants[12]. More recent examples of plasmon-driven photochemical reactions include the azo-coupling of self-assembled para-aminothiophenol (PANP),[13-15] ethylene epoxidation,[16] dissociation of hydrogen molecules,[17] and conversion of aldehydes to esters.[18] The dual action of surface plasmons to enhance Raman scattering and photochemistry provides a unique technical convenience for investigating the mechanism of surface chemistry using SERS as a highly sensitive in situ vibrational spectroscopy.[19-21] However, there are limited model reaction systems particularly the conversion of self-assembled PANP to *p,p′*-dimercaptoazobenzene (DMAB) that can be monitored by probing the vibrational fingerprints of reactants and products using SERS. In addition, studies of plasmon-driven photochemical reactions have been based on excitation wavelengths that match the plasmon resonances but not the molecular resonances. Resonant electronic excitation where the excitation wavelength overlaps with the molecular and plasmon resonances can provide high sensitivity for detecting chemical transformations in situ as the combination of resonance Raman and electromagnetic enhancement effects.[22]

In this chapter, we discuss the first systematic study on N-demethylation of methylene blue (MB) initiated by plasmon-enhanced resonant excitation of MB at 633 nm wavelength. We propose that this demethylation reaction would be an excellent model system for mechanistic studies in plasmon driven photochemistry because of its high detection sensitivity and available background information. The photocatalytic degradation of MB has been investigated using different catalytic materials such as TiO_2,[23] Au-TiO_2 composite,[24] Cr-Ti binary oxide,[24] and Ag-In-Ni-S nanocomposites.[25] The solution phase excited state dynamics of MB is well documented.[26, 27] MB is also a common model system in SERS related studies[28-33] as well as in strong exciton-plasmon coupling,[34] and yet systematic investigation of its plasmon-driven surface photochemistry is lacking. Here, we demonstrate visible light induced chemical transformation of methylene blue adsorbed on gold nanorods (AuNRs) whose surface plasmon resonance (SPR) is matching its electronic transition as revealed from drastic temporal evolution of the SERS spectra. While the vibrational signatures acquired immediately after irradiation are identical to that of MB solid powder, the spectra recorded a few seconds later are similar to that of thionine solid powder, indicating a demethylation reaction at low incident photon flux.

3.3 Spectral overlap of the molecular and plasmon resonances

The experiment has been performed at ambient condition by adsorbing sub-monolayer of MB molecules on gold film (AuF) and depositing colloidal gold nanorods (AuNRs) on top (see **section 2.2.1** for details). The molecules are preferably adsorbed on gold film or silicon substrate with parallel orientation,[35, 36] and the gap between the AuNR and the AuF is estimated to be about 1 nm by taking into accounting for the MB on gold film and the surface ligand (cetyltrimethylammonium bromide) on the AuNRs. The interaction of the

AuNR with the AuF creates enhanced field that is localized in the gap (nanocavity) between AuF-AuNR.[37, 38]. See Error! Reference source not found. for the schematic of s ample preparation procedure.

The spectral overlap between the molecular and plasmon resonances is illustrated in **Figure 3.1**. The 633 nm excitation laser line as indicated by the dashed vertical line overlaps with the broad absorption band (red line) of MB adsorbed on ultrathin gold film shown in **Figure 3.1**a. Compared to the aqueous solution absorbance (green line), this band is red shifted and much broader, which improves spectral overlap with a very broad resonance (red line) of aggregated AuNRs (**Figure 3.1**b). We included the absorption (black line) and scattering (cyan line) spectra of single AuNRs for reference. In solution, the absorption spectrum of the AuNRs peaks at ~680 nm. Dark-field scattering measurement indicates that the average wavelength of maximum scattering of the individual AuNRs supported on gold film is the same (~680 nm) as that of the absorption maximum. All the studies presented here are based on very broad resonances of aggregates of the AuNRs.

The data in **Figure 3.1** show that the broad absorption band of MB adsorbed on gold film lies entirely within a very broad plasmon resonance of the AuNR aggregates. This spectral overlap between the molecular and plasmon resonances provides enormous amplification of the spectroscopic signature of the molecule and makes SERS capable of providing

highly resolved vibration signature of molecules for *in situ* detection of photochemical transformations.

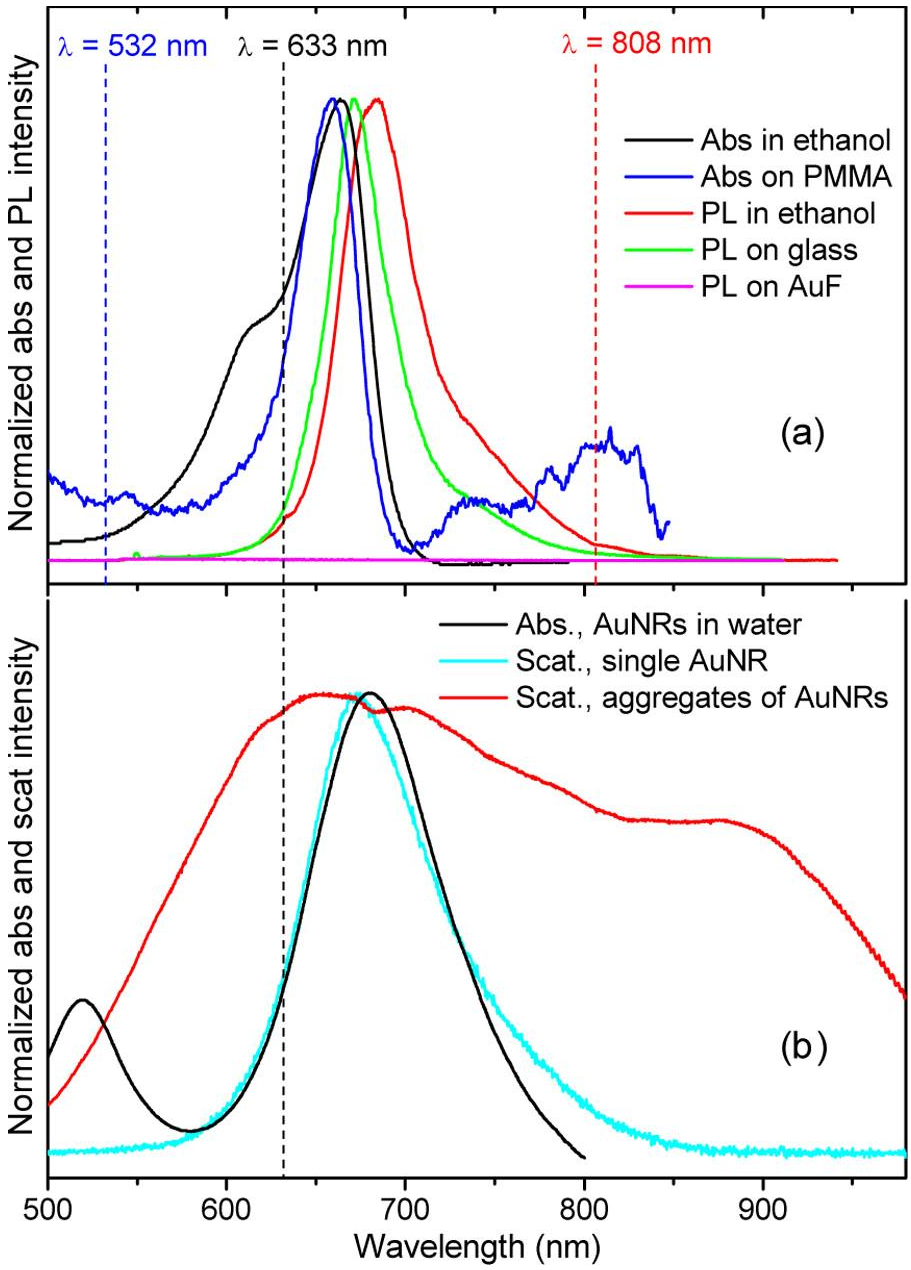

Figure 3.1: The absorption spectrum of 1x10^{-6} M methylene blue in ethanol solution (black line) and the corresponding fluorescence (FL) spectrum (red line). (c) The absorption (black line) and scattering (cyan and red lines) of gold nanorods (AuNRs) with nominal diameter of 40 nm and length 90 nm. The scattering spectra of a single (cyan line) and aggregates (red line) of AuNRs are obtained as the nanorods are adsorbed on MB coated gold film

3.4 Surface-Enhanced Raman Spectra to Monitor Photochemistry

The intensity map of a series of 80 SERS spectra that were acquired continuously with 0.5 s acquisition time and at an interval of 0.017 s is displayed in **Figure 3.2**a. Clearly, new vibrational bands have appeared a few seconds after the resonant excitation laser is on. In particular, a new strong band appears at 479 cm^{-1} within a few seconds upon continuous illumination.

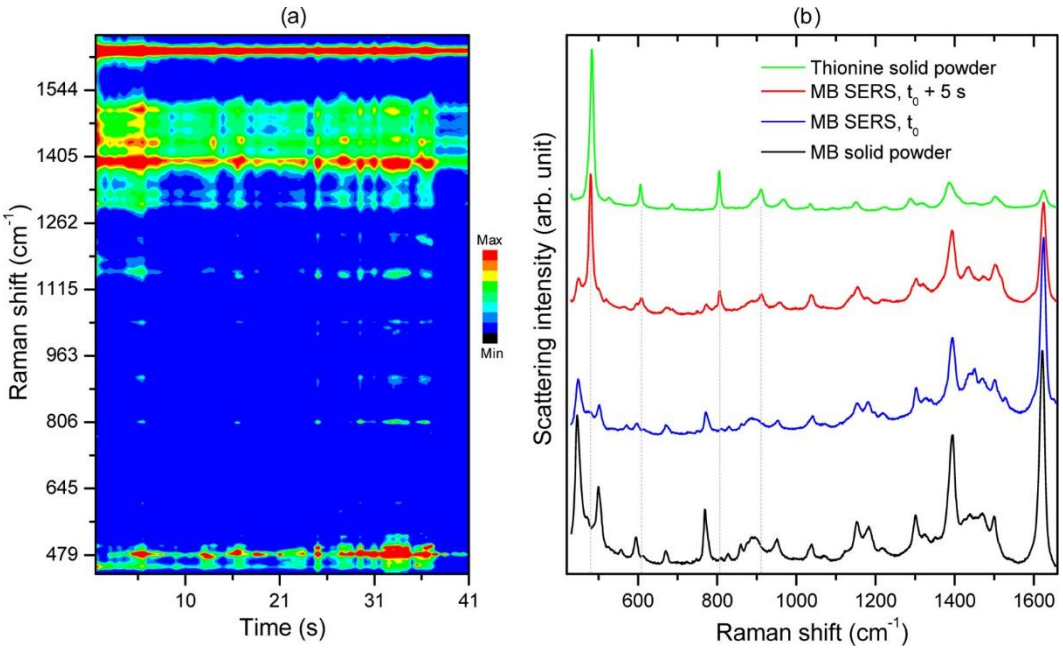

Figure 3.2 Temporal evolution of the SERS signal of methylene blue molecules in plasmonic cavities. (a) Intensity map representing 80 spectra acquired at different time delays after continuous irradiation with λ = 633 nm excitation source is turned on. (b) Representative SERS spectra of MB recorded at the time delays indicated on the plot ($t_0 \approx$ 0.5 s, acquisition time of a single spectrum) compared to the Raman spectra of methylene blue (black line) and thionine (green line) solid powders.

In particular, the peak at 804 cm^{-1} that has been assigned to NH_2 rocking vibrational motion of thionine by Hutchinson and Hester,[39] cannot be attributed to any vibrational features of methylene blue. Therefore, we propose that the spectral evolution is due to N-demethylation reaction that converts methylene blue to thionine. Our spectral assignment

is also supported by theoretical calculation as shown in **Figure 3.3** below. This plasmon-driven demethylation reaction is consistent with the observation in the photocatalytic decomposition of methylene blue in solution on semiconductor catalysts such as TiO_2[23, 40] with UV-radiation and on other semiconductor catalysts.[41]

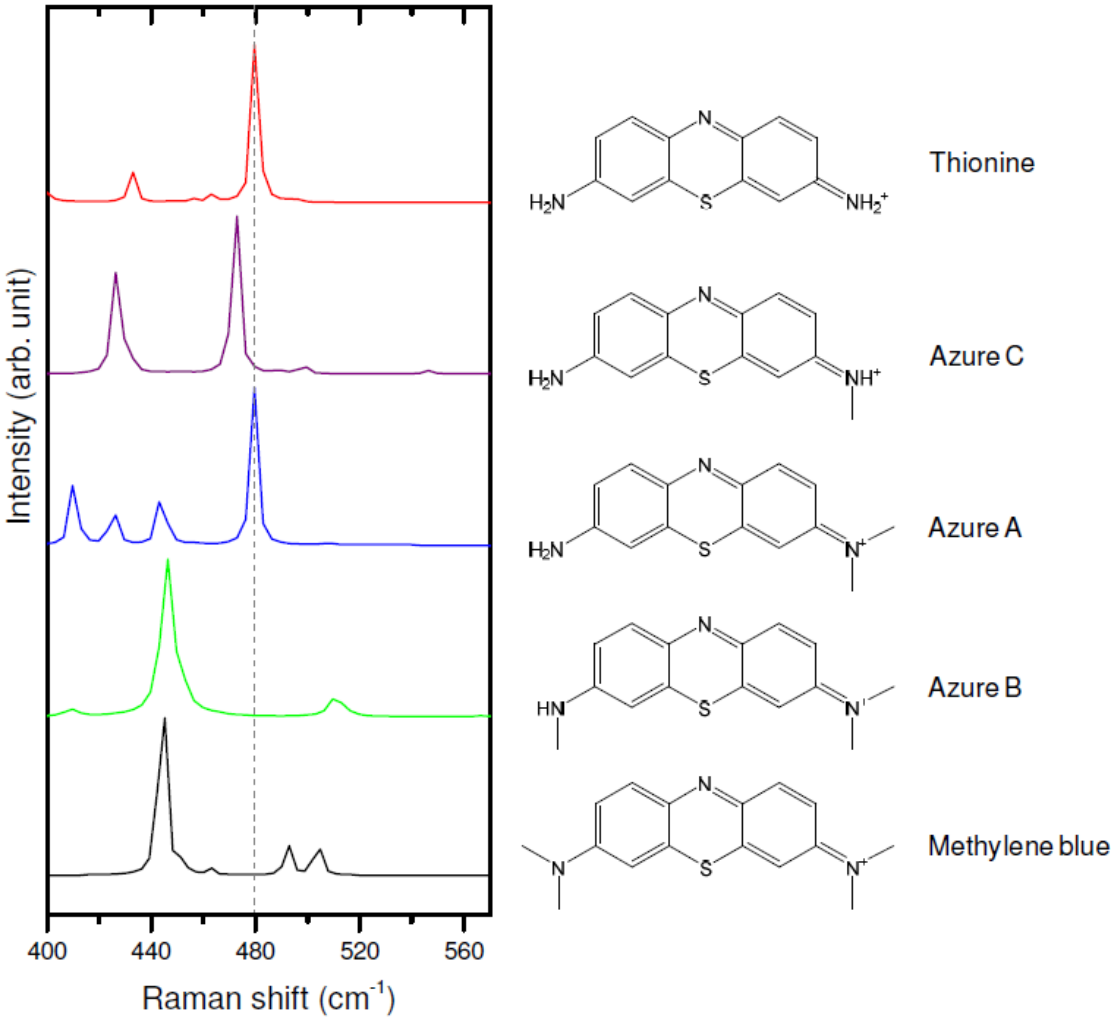

Figure 3.3 Calculated Raman Shifts showing the vibrational modes excited as the methyl groups are replaced with hydrogen atoms in going from MB (bottom spectrum) to TH (top spectrum). We used B3LYP density functional theory for the calculation with DGDZVP basis sets using Gaussian 09 software. The calculation agrees well with experiment in predicting the 479 cm^{-1}band TH but not for MB. The spectrum of Azure B is similar to that of MB. The 479 cm^{-1} band appears for Azure A confirming the excitation of the vibrational mode is triggered by at least complete N-demethylation of terminal N-atom. For Azure C the spectrum is similar to TH apart from small down shift of frequency

The significant time delay for the appearance of the product signals observed in **Figure 3.2a** is in contrast to other plasmon-driven photochemical reactions such as the oxidative coupling of PATP (in which the DMAB product signals appear instantly) as we have confirmed in a separate experiment under similar conditions.[37] However, the drastic intensity fluctuation observed in **Figure 3.2a** does not allow us to draw conclusion based on the temporal profile of the vibrational signals of molecules within a single focus area (~4×10^{-7} cm^2) on the sample. The intensity fluctuation can be minimized by repeating the time-dependent measurement on multiple areas so that mechanistic understanding may be obtained based on the trend of the average data.

3.5 Laser power dependence of temporal evolution of SERS signals

To have quantitative understanding of the temporal evolution of SERS signals we analyzed an average of 400 spectra that have been acquired with continuous illumination for about 207 s at 0.5 s acquisition time. We acquired each spectrum with time interval of 0.017 s from at least 10 different random locations on the sample. We used same procedure for incident laser powers dependent experiments. For the sake of clarity, the intensity map of the average spectra of the most prominent peaks are presented in **Figure 3.4**a,b, which represent the trend at 0.16 mW and 0.73 mW incident laser powers, respectively. The average data in **Figure 3.4**a,b show clearly the delay in the evolution of the 479 cm^{-1} product signal and its incident laser power dependence. The time delay may indicate that laser-induced adsorption is the prerequisite for the photochemical reaction.[42] Unlike molecules such as PATP that are chemically attached to the surface through Au-S bond, MB may be weakly adsorbed mainly through physical interactions. The fact that the vibrational frequencies in the SERS and regular Raman spectrum of the solid agree within

±3 cm^{-1} as can be seen by comparing the blue and black spectra in **Figure 3.2**b is characteristic of physisorption.[43] The heat released following the plasmon enhanced resonant excitation may increase molecule-surface interaction that facilitates the photochemistry.

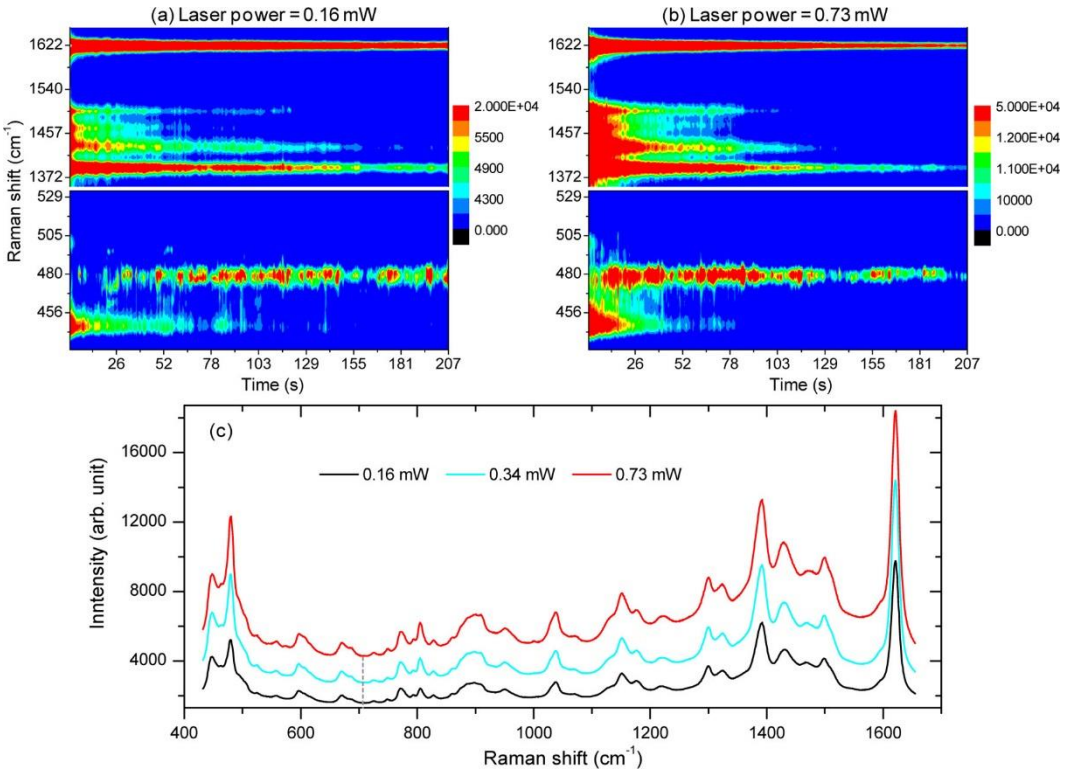

Figure 3.4 Average SERS spectra of AuF-MB-AuNR obtained at 633 nm excitation wavelength and incident laser power of (a) 0.16 mW, and (b) 0.73 mW. Each intensity map represents 400 spectra acquired within 207 seconds, and the spectra at each time point are the average of at least 10 spectra that represent different locations on the sample. (c) Average of the spectra acquired within 207 seconds at incident laser power of 0.16 mW (black line), 0.34 mW (cyan line) and 0.73 mW (red line). Note that with increasing laser power, both the background and the vibrational band intensities increase. The flat region at ~707 cm-1 marked with vertical dashed line is used for background correction and for studying the temporal evolution of the vibrational band intensities.

The average spectra plotted in **Figure 3.4c** show that increasing the laser power increases the intensity of the vibrational signal as well as that of the background.

3.6 Comprehensive analysis of the temporal evolution of SERS signals

For more comprehensive analysis of the vibrational intensities, we identified a relatively flat spectral region at ~707 cm^{-1}, marked with a vertical dashed line in **Error! Reference s ource not found.**c that can be used as a reference to correct for time dependent background intensity. That is, at any time, the vibrational intensity $[I_v(t)]$ of a given vibrational mode is adjusted as$[I_v(t) - I_b(t)]/I_b(t)$, where $I_b(t)$ is the background intensity at time t. This approach provides the relative change of the vibrational intensity with respect to the background. The stronger background at higher laser power can scale down the amplitude change but will not affect the rate of signal decay or rise.

The background corrected intensities of the bands at 1621 cm^{-1} and 479 cm^{-1} are extracted from the data presented in **Figure 3.4**a,b the results are plotted in **Figure 3.5**a,b. The 1621 cm^{-1} band intensity is further normalized by the corresponding average value at time t_0. We note that both MB and thionine have the 1621 cm^{-1} band but its relative intensity is much weaker for thionine (see **Figure 3.2**). This results in rapid decline of the 1621 cm^{-1} band intensity as the MB is converted to thionine. For laser power above 0.16 mW, the decay has a fast and slow components, and the relevant rate constants can be extracted by fitting an exponential function of the form $y = a + be^{-t/\tau_1} + ce^{-t/\tau_2}$, where τ_1 and τ_2 are the time constants for the fast and slow dynamics, respectively. A single exponential function of the form $y = a - be^{-t/\tau}$ fits the rising signal of the product reasonably as shown by the solid lines in **Figure 3.5**b**.**

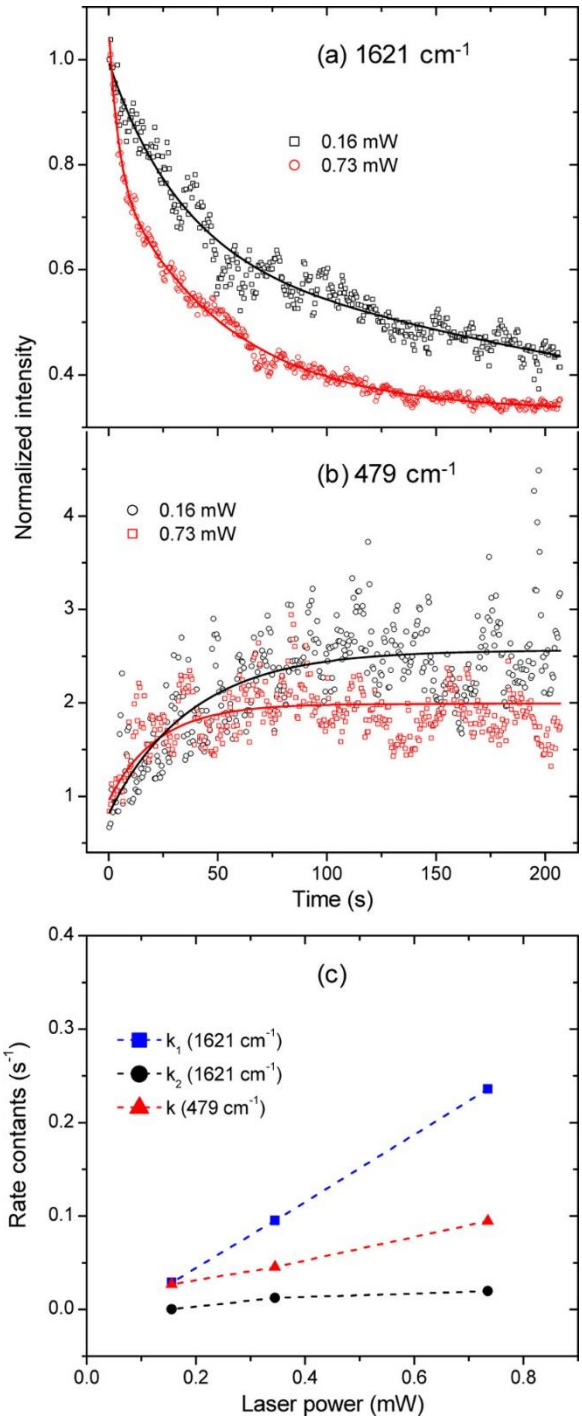

Figure 3.5: Comprehensive analysis of the temporal evolution of the SERS signals using representative vibrational bands of reactant and product species. (a) The peak intensity of the 1621 cm^{-1} band plotted as a function of time. The solid lines represent exponential function fit to the data.(b) The same as (a) but for 479 cm^{-1} band and a single exponential function is fit to the data. (c) The rate constants ($\boldsymbol{k = 1/\tau}$) extracted from the fitting procedure in (a) and (b) are plotted as a function of laser power.

This divergence of rate constants for the reactant signal decay and product signal rise with incident photon flux indicates contribution of additional process such as desorption and gradual photo bleaching of reactant molecules. These additional processes may be accounted by the constant k_2 that increases slowly with laser power.

3.7 Effect of excitation source and localized surface plasmon resonance on N-demethylation

We switched the excitation source from 633 nm to shorter (532 nm) and longer (808 nm) wavelength to study the wavelength dependence of the photochemical reaction. As is, the system does not give any SERS signal let alone probing the photochemical transformation. In fact, it requires tuning the localized surface resonance of gold nanoparticle placed on gold film to overlap the excitation source by varying size and shape of the particles. This take us back to the understanding of fundamentals of the optical responses of metal particles placed near to different substrates. We used gold nanorods of different aspect ratio and dielectric and metallic substrates to study these effects on plasmonic response as described in detail in the following sections.

3.7.1 Effect of supporting substrate on the spectral position of localized surface plasmon resonance

The characteristics of a plasmon resonance are determined by shape, size, and material properties of plasmonic metallic nanostructure as well as by the surrounding dielectric environment.[44] A typical example of such dependence is the red shift experienced by the plasmon resonance of a metallic nanostructure when placed near a dielectric substrate.[45] This plasmonic response is stronger if the substrate is metallic due to the coupling of conduction electrons of the substrate with that of the nanoparticle,[38, 46-49] which results in an extraordinary electric field concentrated in the gap separating the two systems.[50-54] This

field enhancement is particularly large when molecular spacers on the nanometer scale are used.[55] Due to this effect, coupled metallic particle−film structures have been the subject of extensive research in recent years[37, 55-60] as a promising platform for achieving ultrasensitive molecule detection,[61-63] single molecule optomechanics,[64] strong coupling,[65] enhanced emission, [66-68] and color printing.[69]

Albeit all these research effort and widespread applications of particle−film plasmonic systems, the interaction between a colloidal nanoparticle and metal film is not fully understood. These nanoparticles are inherently coated with surface ligands that provide a natural spacer of a thickness on the order of a few nanometers.[70-74] Plasmonic response of this coupled system and nature of their interaction depends strongly on the chemical and physical properties of the spacer layer. Notably, if the particles and the film are bridged by a conductive junction, it causes a distinct type of plasmonic resonances, commonly referred to as charge transfer plasmons.[75] This configuration enables the charges to oscillate between the two systems.[76] These modes have been extensively investigated in particle dimers due to their potential for sensing applications.[75, 77-79]

On a separate study, we report the investigation of how the optical response of colloidal metallic nanoparticles is modified as a result of the interaction with metallic substrates. For this, we measured and analyzed the scattering spectra of individual gold nanorods of different sizes deposited on both silica and gold substrates. Interestingly, we found that, when they are placed on the gold film, the scattering response of the gold nanorods is

weakly dependent on their size and width. This is in sharp contrast with the behavior shown by nanorods with similar sizes placed on the purely dielectric substrate.

3.7.2 Excitation wavelength Dependence

For understanding the role of the MB resonant excitation in the demethylation reaction, we have measured the SERS spectra at 532 and 808 nm excitation wavelengths such that the excitation energy overlaps with the plasmon resonances but not with the electronic transition energy of MB. **Figure 3.6**a shows the dark-field scattering spectra of MB functionalized aggregates of gold nanospheres (AuNSs) and AuNRs that are deposited on oxide coated silicon wafer. These AuNRs are longer (40 x 148 nm) than the AuNRs used to obtain the results in **Figure 3.1**−Error! Reference source not found. The plasmon r esonances of the AuNSs overlap more significantly with the 532 nm laser than with the 633 nm. Similarly, the plasmon resonances of the longer AuNRs overlap more significantly with the 808 nm laser than with the 633 nm laser line. However, the SERS spectra in **Figure 3.6**b show that neither 532 nm (blue spectrum) nor 808 nm (red spectrum) excitation wavelengths gave the prominent 479 and 804 cm^{-1} bands, which are the vibrational signatures of complete N-demethylation of MB to TH despite the more significant spectral overlap of the plasmon resonances with the corresponding wavelengths as illustrated in **Figure 3.6**a. In contrast, the SERS spectra obtained at 633 nm excitation wavelength for both the AuNSs (black line) and the AuNRs (green line) gave the characteristic bands of the product as indicated by the vertical dashed cyan lines.

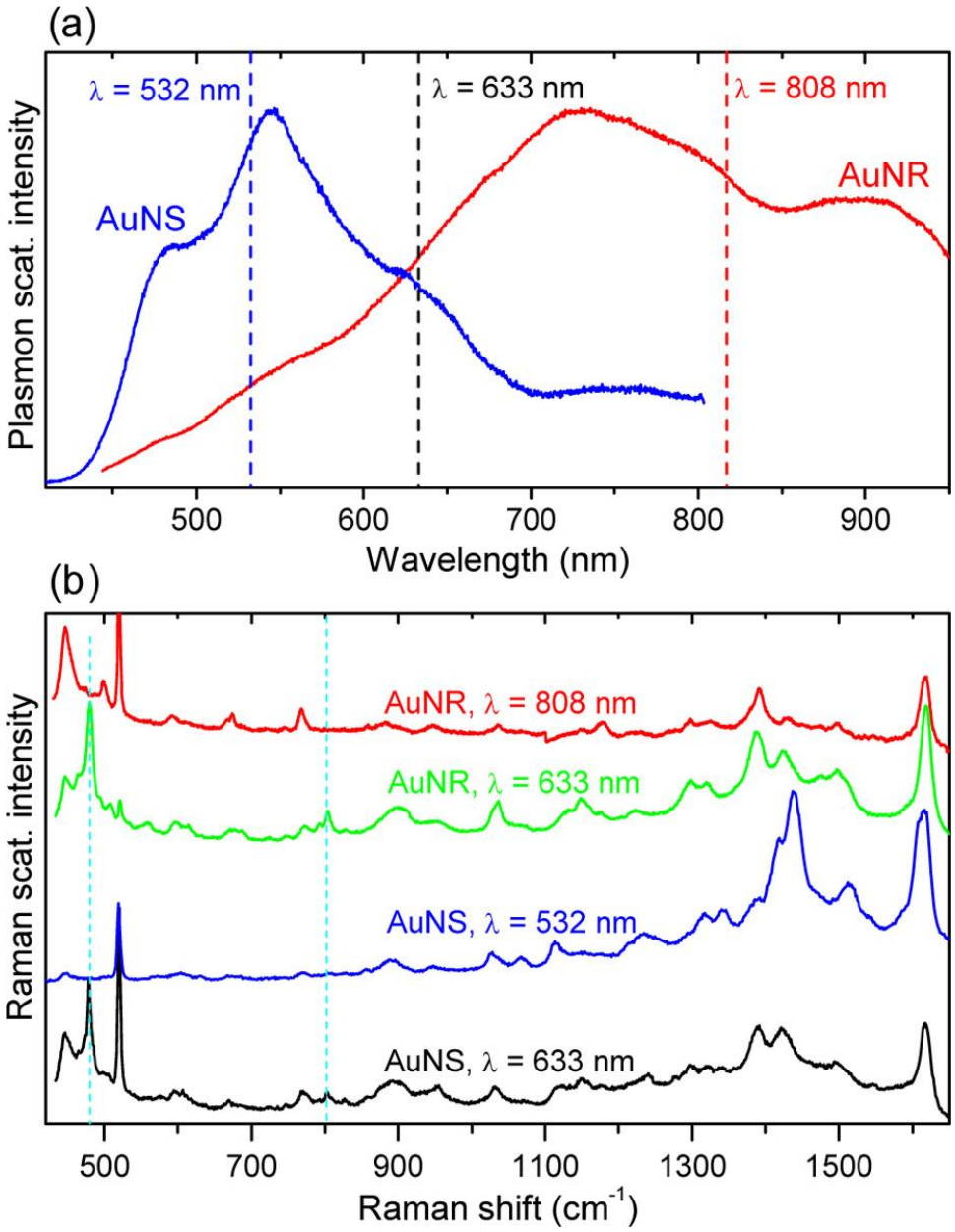

Figure 3.6 (a) Dark-field scattering spectra of aggregates of gold nanospheres (AuNSs, diameter 40 nm) (blue line) and gold nanorods (AuNRs, 40 nm × 148 nm) (red line) functionalized with MB and deposited on silica surface. (b) SERS spectra of MB adsorbed on the AuNS and AuNRs recorded 30 s after exposing to the lasers. The vertical dashed cyan lines indicate the vibrational frequencies of thionine at 479 and 804 cm^{-1}. The peak at 520 cm^{-1} in all the spectra in (b) is due to silicon.

On the other hand, resonant excitation of MB on non-plasmonic surfaces (glass, platinum, aluminum, and gold) does not show vibrational signatures of thionine. An example is

shown in **Figure 3.6**c, where MB is adsorbed on gold film, and the Raman spectra obtained after continuous exposure to the 633 nm laser. These observations indicate that excitation of both the molecular and the plasmon resonances is important for the N-demethylation reaction.

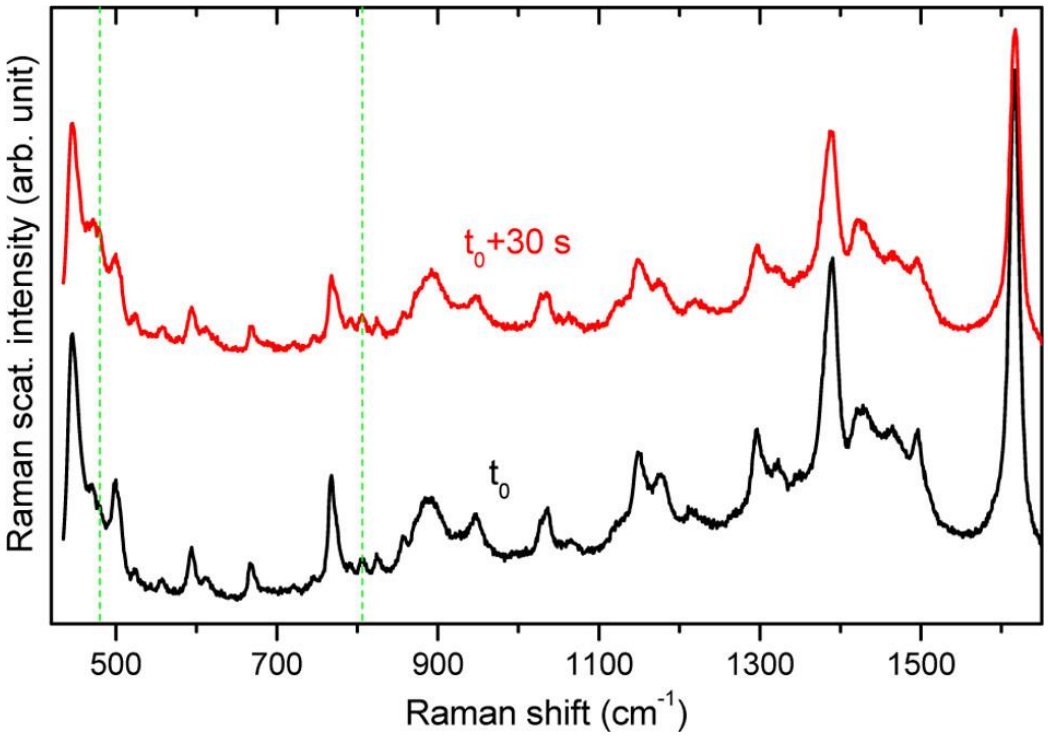

Figure 3.7 Raman spectra of MB adsorbed on gold film without plasmonic nanoparticles. More than a monolayer layer of MB was adsorbed so as to improve the signal-to-noise ratio of the Raman spectrum. The spectra were recorded with an acquisition time of 1 s at 633 nm excitation wavelength and intensity of ~100 kW/cm^2. The vertical dashed green lines indicate absence of vibrational frequencies of thionine at 479 and 804 cm^{-1}.

3.8 Mechanism of Plasmon-Enhanced Excitation and Demethylation

The mechanism of plasmon-driven photochemical reactions is believed to involve hot plasmon electron transfer from the nanocrystal to the adsorbed species.[1, 8, 19-21]. However, consistent with this charge transfer framework, several specific mechanisms can be proposed including: (i) direct excitation of the metal-molecule system that involves

electron transition from occupied to unoccupied adsorbate states, and (ii) hot electron transfer to other species such as adsorbed oxygen molecules that then initiate the reaction.[86]

Direct charge excitation has been implied on the basis of SERS results on MB that show an excitation wavelength-dependent anti-Stokes to Stokes Raman intensity ratio.[32, 87] Anti-Stokes to Stokes Raman intensity ratio as high as 34 has been observed at λ = 785 nm excitation wavelength, whereas the ratio is less than unity at λ = 532 nm excitation wavelength.[32] On the basis of this observation and the positive dependence of the ratio on the 785 nm photon flux, Boerigter et al. have proposed a direct resonant charge excitation mechanism that populates the excited vibrational energy levels of adsorbed MB. However, no chemical transformation of MB has been observed in the experiments by Boerigter et al.[32, 87] Also, it's noted that the resonant excitation wavelengths of adsorbed MB can range from 520 to 800 nm depending on the nature of the surface−molecule interaction and on the cluster size of MB (monomer, dimer, trimer, etc.).[29, 88, 89]

Our sample is prepared so that MB is adsorbed on the gold film as a monomer, and at 633 nm excitation wavelength, the anti-Stokes to Stokes Raman intensity remains very small and constant during the continuous illumination and acquisition of data for over 200 s as shown in **Figure 3.8**.

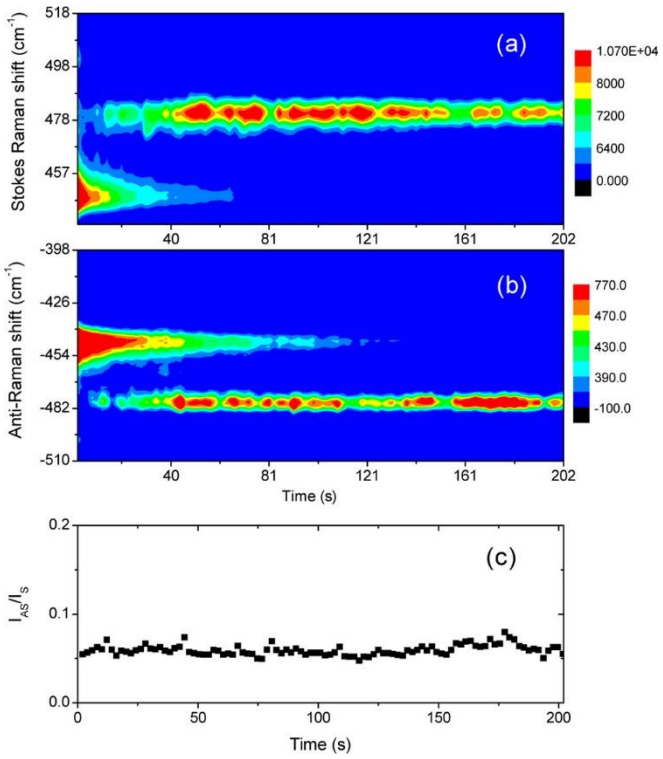

Figure 3.8: Comparison of the temporal evolution of the Stokes (a) and anti-Stokes (b) Raman intensities of the 448 cm^{-1} and 479 cm^{-1} bands. (c) Stokes to ant-Stokes intensity ratio of the 479 cm^{-1} band plotted as a function of time.

It has been reported that photocatalytic N-demethylation requires the presence of oxygen.[23, 40, 41] In particular, Takizawa et al. demonstrated systematically that anionic oxygen is responsible for initiating the demethylation of MB and Rhodamine B on CdS catalyst.[41]

Transient anionic oxygen created via hot plasmon electron injection has also been implicated in the surface photochemistry of PATP.[86, 90, 91].

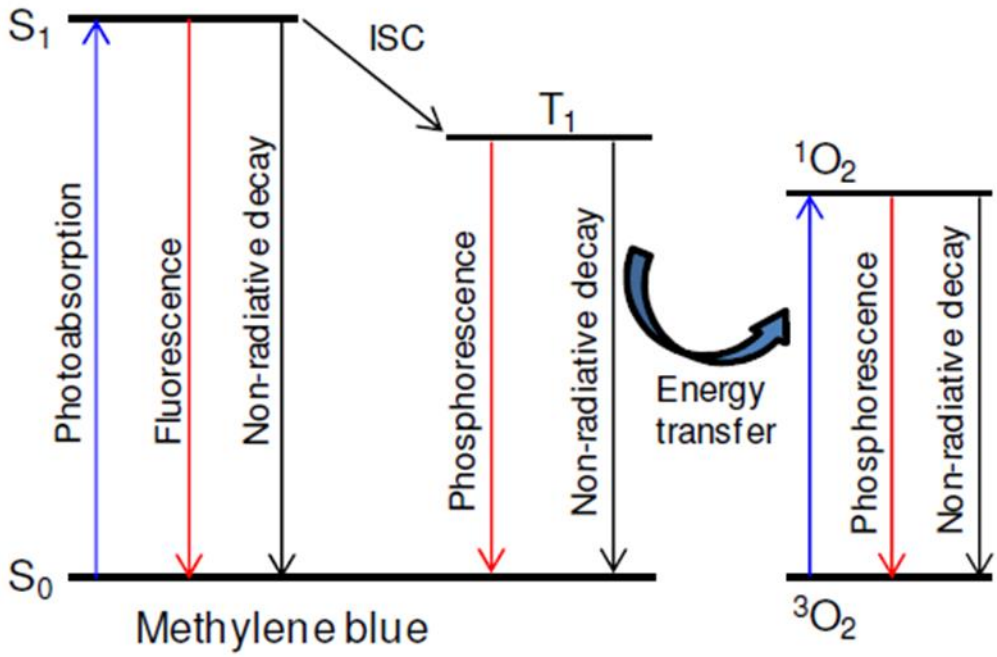

Figure 3.9: Energy diagram showing excitation and decay channels of methylene blue. The singlet ground state (S_0) to single excited state (S_1) transition is accessible at 633 nm excitation. After intersystem crossing (ISC), the triplet state population can be annihilated via efficient energy transfer (ET) to molecular oxygen in the ground state ($^3O_2$) that leads to excitation to singlet oxygen ($^1O_2$)

To propose the mechanism of excitation of N-demethylation of MB, it is very important to emphasize a detailed description of the mechanism that requires understanding the excited-state dynamics of MB adsorbed on metal surfaces. As shown in **Figure 3.9**, initial excitation of MB can be followed by singlet to triplet intersystem crossing (quantum yield ~0.5)[92] that can lead to generation of singlet oxygen through efficient energy transfer from the triplet MB to triplet molecular oxygen,[93] a reason for wide use of MB as photosensitizer in photodynamic therapy. The singlet oxygen can interact with the terminal nitrogen atoms

of MB, and hydrogen abstraction from water can lead to the transformation of methylene blue to thionine and another side product, possibly formaldehyde.[41] The fact that the demethylation of MB is observed at 633 excitation wavelength (that can promote MB from ground to excited electronic state) but not at 532 and 808 nm is consistent with the involvement of singlet oxygen in the photochemical transformation. On the other hand, the demethylation reaction does not take place on nonplasmonic surfaces, indicating the importance plasmon resonance excitation. Understanding these excited-state dynamics of molecules in the proximity of metal surfaces is a grand challenge that may invite future experiments.

3.9 Conclusion

In summary, we have presented the first systematic study of plasmon driven demethylation reaction that transforms methylene blue to thionine under visible light irradiation at room temperature without the use of any semiconductor catalysts. Upon continuous irradiation, the SERS spectra evolve from that of methylene blue to thionine as a function of time. Irradiation of MB adsorbed on non-plasmonic surfaces at 633 nm excitation wavelength does not lead to the demethylation reaction. We find that substrates have significant effect on tuning the surface plasmon resonance with respect to the electronic absorption band of the molecule.

Similarly, excitation wavelengths 532 nm and 808 nm that overlap with plasmon resonances but not with the electronic absorption band of MB do not transform MB to thionine. These observations suggest that excitations of both the molecular and the plasmon resonances are important for observing the reaction. The photochemical transformation is likely initiated by transient hot plasmon electron transfer to adsorbed species. However,

identifying transient intermediates and a detailed understanding of the mechanism require further experiments under controlled atmosphere as well as elucidating the potential energy landscape of MB adsorbed on metal surfaces. At visible excitation wavelengths, both MB and thionine have large SERS cross sections due to the combination of resonance Raman and electromagnetic enhancement effects, and therefore we suggest that this demethylation reaction serves as a convenient model system for future mechanistic studies in plasmon driven photochemical reactions.

3.10 References

1. Jeanmaire, D.L. & Vanduyne, R.P. Surface Raman Spectroelectrochemistry 0.1. Heterocyclic, Aromatic, and Aliphatic-Amines Adsorbed on Anodized Silver Electrode. *J. Electroanal. Chem. Interfacial Electrochem.* **84**, 1 (1977).

2. Moskovits, M. Surface-Roughness and Enhanced Intensity of Raman-Scattering by Molecules Adsorbed on Metals. *J. Chem. Phys.* **69**, 4159 (1978).

3. Nitzan, A. & Brus, L.E. Can Photochemistry Be Enhanced on Rough Surfaces? *J. Chem. Phys.* **74**, 5321 (1981).

4. Nitzan, A. & Brus, L.E. Theoretical-Model for Enhanced Photochemistry on Rough Surfaces. *J. Chem. Phys.* **75**, 2205 (1981).

5. Bunding, K.A., Durst, R.A. & Bell, M.I. Surface-Enhanced Raman-Spectroscopy of N-Methylpyridinium Cation and Pyridine - Identification of Surface Species. *J. Electroanal. Chem. Interfacial Electrochem.* **150**, 437 (1983).

6. Goncher, G.M. & Harris, C.B. Enhanced Photofragmentation on a Silver Surface. *J. Chem. Phys.* **77**, 3767 (1982).

7. Goncher, G.M., Parsons, C.A. & Harris, C.B. Photochemistry on Rough Metal-Surfaces. *J. Phys. Chem.* **88**, 4200 (1984).

8. Lu, T., Birke, R.L. & Lombardi, J.R. Surface Raman-Spectroscopy of the 3 Redox Forms of Methylviologen. *Langmuir* **2**, 305 (1986).

9. Sun, S.C., Birke, R.L., Lombardi, J.R., Leung, K.P. & Genack, A.Z. Photolysis of Para-Nitrobenzoic Acid on Roughened Silver Surfaces. *J. Phys. Chem.* **92**, 5965 (1988).

10. White, J.M. Photochemistry at Adsorbate Metal Interfaces - Issues and Examples. *J. Vac. Sci. Technol., B: Microelectron. Process. Phenom.* **10**, 191 (1992).

11. Wolkow, R.A. & Moskovits, M. Enhanced Photochemistry on Silver Surfaces. *J. Chem. Phys.* **87**, 5858 (1987).

12. Suh, J.S., Jang, N.H., Jeong, D.H. & Moskovits, M. Adsorbate Photochemistry on a Colloid Surface: Phthalazine on Silver. *J. Phys. Chem.* **100**, 805 (1996).

13. Fang, Y.R., Li, Y.Z., Xu, H.X. & Sun, M.T. Ascertaining P,P ′-Dimercaptoazobenzene Produced from P-Aminothiophenol by Selective Catalytic Coupling Reaction on Silver Nanoparticles. *Langmuir* **26**, 7737 (2010).

14. Huang, Y.F. et al. When the Signal Is Not from the Original Molecule to Be Detected: Chemical Transformation of Para-Aminothiophenol on Ag During the SERS Measurement. *J. Am. Chem. Soc.* **132**, 9244 (2010).

15. Yan, X.F., Wang, L.Z., Tan, X.J., Tian, B.Z. & Zhang, J.L. Surface-Enhanced Raman Spectroscopy Assisted by Radical Capturer for Tracking of Plasmon-Driven Redox Reaction. *Sci. Rep.* **6**, 30193 (2016).

16. Christopher, P., Xin, H.L. & Linic, S. Visible-Light-Enhanced Catalytic Oxidation Reactions on Plasmonic Silver Nanostructures. *Nat. Chem.* **3**, 467 (2011).

17. Mukherjee, S. et al., Hot Electrons Do the Impossible: Plasmon-Induced Dissociation of H-2 on Au. *Nano Lett.* **13**, 240 (2013).

18. Zhang, Y. et al. Direct Photocatalytic Conversion of Aldehydes to Esters Using Supported Gold Nanoparticles under Visible Light Irradiation at Room Temperature. *J. Phys. Chem. C* **118**, 19062 (2014).

19. Kleinman, S.L. et al. Single-Molecule Surface-Enhanced Raman Spectroscopy of Crystal Violet Isotopologues: Theory and Experiment. *J. Am. Chem. Soc.* **133**, 4115 (2011).

20. Kneipp, K. et al. Single Molecule Detection Using Surface-Enhanced Raman Scattering (SERS). *Phys. Rev. Lett.* **78**, 1667 (1997).

21. Nie, S. & Emory, S.R. Probing Single Molecules and Single Nanoparticles by Surface-Enhanced Raman Scattering. *Science* **275**, 1102 (1997).

22. Lombardi, J.R. & Birke, R.L. A Unified Approach to Surface-Enhanced Raman Spectroscopy. *J. Phys. Chem. C* **112**, 5605 (2008).

23. Zhang, T.Y. et al. Photooxidative N-Demethylation of Methylene Blue in Aqueous TiO2 Dispersions under Uv Irradiation. *J. Photochem. Photobiol., A* **140**, 163 (2001).

24. Rauf, M.A., Meetani, M.A., Khaleel, A. & Ahmed, A. Photocatalytic Degradation of Methylene Blue Using a Mixed Catalyst and Product Analysis by LC/MS. *Chem. Eng. J.* **157**, 373 (2010).

25. Molla, A., Sahu, M. & Hussain, S. Under Dark and Visible Light: Fast Degradation of Methylene Blue in the Presence of Ag-In-Ni-S Nanocomposites. *J. Mater. Chem. A* **3**, 15616 (2015).

26. Chen, J., Cesario, T.C. & Rentzepis, P.M. Time Resolved Spectroscopic Studies of Methylene Blue and Phenothiazine Derivatives Used for Bacteria Inactivation. *Chem. Phys. Lett.* **498**, 81 (2010).

27. Dean, J.C., Oblinsky, D.G., Rafiq, S. & Scholes, G.D. Methylene Blue Exciton States Steer Nonradiative Relaxation: Ultrafast Spectroscopy of Methylene Blue Dimer. *J. Phys. Chem. B* **120**, 440 (2016).

28. Naujok, R.R., Duevel, R.V. & Corn, R.M. Fluorescence and Fourier-Transform Surface-Enhanced Raman-Scattering Measurements of Methylene-Blue Adsorbed onto a Sulfur-Modified Gold Electrode. *Langmuir* **9**, 1771 (1993).

29. Rubim, J.C., Sousa, M.H., Silva, J.C.O. & Tourinho, F.A. Raman Spectroscopy as a Powerful Technique in the Characterization of Ferrofluids. *Braz. J. Phys.* **31**, 402 (2001).

30. Nicolai, S.H.A. & Rubim, J.C. Surface-Enhanced Resonance Raman (SERR) Spectra of Methylene Blue Adsorbed on a Silver Electrode. *Langmuir* **19**, 4291 (2003).

31. Xiao, G.N. & Man, S.Q. Surface-Enhanced Raman Scattering of Methylene Blue Adsorbed on Cap-Shaped Silver Nanoparticles. *Chem. Phys. Lett.* **447**, 305 (2007).

32. Boerigter, C., Campana, R., Morabito, M. & Linic, S. Evidence and Implications of Direct Charge Excitation as the Dominant Mechanism in Plasmon-Mediated Photocatalysis. *Nat. Commun.* **7**, 10545 (2016).

33. Fazio, B. et al. Re-Radiation Enhancement in Polarized Surface-Enhanced Resonant Raman Scattering of Randomly Oriented Molecules on Self-Organized Gold Nanowires. *ACS Nano* **5**, 5945 (2011).

34. Chikkaraddy, R. et al. Single-Molecule Strong Coupling at Room Temperature in Plasmonic Nanocavities. *Nature* **535**, 127 (2016).

35. Anderson, S. Orientation of Methylene Blue Molecules Adsorbed on Solids. *J. Opt. Soc. Am.* **39**, 49 (1949).

36. Greathouse, J.A. et al. Methylene Blue Adsorption on the Basal Surfaces of Kaolinite: Structure and Thermodynamics from Quantum and Classical Molecular Simulation. *Clays Clay Miner.* **63**, 185 (2015).

37. Kafle, B., Poveda, M. & Habteyes, T.G. Surface Ligand-Mediated Plasmon-Driven Photochemical Reactions. *J. Phys. Chem. Lett.* **8**, 890 (2017).

38. Mock, J.J. et al. Distance-Dependent Plasmon Resonant Coupling between a Gold Nanoparticle and Gold Film. *Nano Lett.* **8**, 2245 (2008).

39. Hutchinson, K., Hester, R.E., Albery, W.J. & Hillman, A.R. Raman-Spectroscopic Studies of a Thionine-Modified Electrode. *J. Chem. Soc., Faraday Trans. 1* **80**, 2053 (1984).

40. Yogi, C. et al. Photocatalytic Degradation of Methylene Blue by TiO2 Film and Au Particles-TiO2 Composite Film. *Thin Solid Films* **516**, 5881 (2008).

41. Takizawa, T., Watanabe, T. & Honda, K. Photocatalysis through Excitation of Adsorbates 0.2. Comparative-Study of Rhodamine-B and Methylene-Blue on Cadmium-Sulfide. *J. Phys. Chem.* **82**, 1391 (1978).

42. Fox, M.A. & Dulay, M.T. Heterogeneous Photocatalysis. *Chem. Rev.* **93**, 341 (1993).

43. Otto, A., Mrozek, I., Grabhorn, H. & Akemann, W. Surface-Enhanced Raman-Scattering. *J. Phys.: Condens. Matter* **4**, 1143 (1992).

44. Myroshnychenko, V. et al. Modelling the optical response of highly faceted metal nanoparticles with a fully 3D boundary element method. *Adv. Mater.* **20**, 4288 (2008).

45. Knight, M.W., Wu, Y., Lassiter, J.B., Nordlander, P. & Halas, N.J. Substrates Matter: Influence of an Adjacent Dielectric on an Individual Plasmonic Nanoparticle. *Nano Lett.* **9**, 2188 (2009).

46. Aravind, P.K. & Metiu, H. Use of a perfectly conducting sphere to excite the plasmon of a flat surface. 1. Calculation of the local field with applications to surface-enhanced spectroscopy. *J. Phys. Chem.* **86**, 5076 (1982).

47. Esteban, R. et al. The Morphology of Narrow Gaps Modifies the Plasmonic Response. *ACS Photonics* **2**, 295 (2015).

48. Lévêque, G. & Martin, O.J.F. Optical interactions in a plasmonic particle coupled to a metallic film. *Opt. Express* **14**, 9971 (2006).

49. Sobhani, A. et al. Pronounced Linewidth Narrowing of an Aluminum Nanoparticle Plasmon Resonance by Interaction with an Aluminum Metallic Film. *Nano Lett.* **15**, 6946 (2015).

50. Chikkaraddy, R. et al. How Ultranarrow Gap Symmetries Control Plasmonic Nanocavity Modes: From Cubes to Spheres in the Nanoparticle-on-Mirror. *ACS Photonics* **4**, 469 (2017).

51. Ciracì, C. et al. Probing the ultimate limits of plasmonic enhancement. *Science* **337**, 1072 (2012).

52. Huang, S. et al. Ultrasmall Mode Volumes in Plasmonic Cavities of Nanoparticle-on-Mirror Structures. *Small* **12**, 5190 (2016).

53. Lassiter, J.B. et al. Plasmonic Waveguide Modes of Film-Coupled Metallic Nanocubes. *Nano Lett.* **13**, 5866 (2013).

54. Tserkezis, C. et al. Hybridization of plasmonic antenna and cavity modes: Extreme optics of nanoparticle-on-mirror nanogaps. *Phys. Rev. A: At., Mol., Opt. Phys.* **92**, 053811 (2015).

55. Mertens, J. et al. Controlling Subnanometer Gaps in Plasmonic Dimers Using Graphene. *Nano Lett.* **13**, 5033 (2013).

56. Hu, M., Ghoshal, A., Marquez, M. & Kik, P.G. Single Particle Spectroscopy Study of Metal-Film-Induced Tuning of Silver Nanoparticle Plasmon Resonances. *J. Phys. Chem. C* **114**, 7509 (2010).

57. Huh, J.H., Lee, J. & Lee, S. Comparative Study of Plasmonic Resonances between the Roundest and Randomly Faceted Au Nanoparticles-on-Mirror Cavities. *ACS Photonics* **5**, 413 (2018).

58. Lumdee, C., Toroghi, S. & Kik, P.G. Post-fabrication Voltage Controlled Resonance Tuning of Nanoscale Plasmonic Antennas. *ACS Nano* **6**, 6301 (2012).

59. Mock, J.J., Hill, R.T., Tsai, Y.J., Chilkoti, A. & Smith, D.R. Probing Dynamically Tunable Localized Surface Plasmon Resonances of Film-Coupled Nanoparticles by Evanescent Wave Excitation. *Nano Lett.* **12**, 1757 (2012).

60. Moreau, A. et al. Controlled-reflectance surfaces with film-coupled colloidal nanoantennas. *Nature* **492**, 86 (2012).

61. Benz, F. et al. Nanooptics of Molecular-Shunted Plasmonic Nanojunctions. *Nano Lett.* **15**, 669 (2015).

62. Liu, P., Chulhai, D.V. & Jensen, L. Single-Molecule Imaging Using Atomistic Near-Field Tip-Enhanced Raman Spectroscopy. *ACS Nano* **11**, 5094 (2017).

63. Taylor, R.W. et al. Watching individual molecules flex within lipid membranes using SERS. *Sci. Rep.* **4**, 5940 (2015).

64. Benz, F. et al. Single-molecule optomechanics in “picocavities. *Science* **354**, 726 (2016).

65. Kleemann, M.E. et al. Strong-coupling of WSe2 in ultra-compact plasmonic nanocavities at room temperature. *Nat. Commun.* **8**, 1296 (2017).

66. Akselrod, G.M. et al. Probing the mechanisms of large Purcell enhancement in plasmonic nanoantennas. *Nat. Photonics* **8**, 835 (2014).

67. Hoang, T.B. et al. Ultrafast spontaneous emission source using plasmonic nanoantennas. *Nat. Commun.* **6**, 7788 (2015).

68. Huang, J., Akselrod, G.M., Ming, T., Kong, J. & Mikkelsen, M.H. Tailored Emission Spectrum of 2D Semiconductors Using Plasmonic Nanocavities. *ACS Photonics* **5**, 552 (2018).

69. Stewart, J.W., Akselrod, G.M., Smith, D.R. & Mikkelsen, M.H. Toward Multispectral Imaging with Colloidal Metasurface Pixels. *Adv. Mater.* **29**, 1602971 (2017).

70. Chen, X., Moore, J.E., Zekarias, M. & Jensen, L. Atomistic electrodynamics simulations of bare and ligand-coated nanoparticles in the quantum size regime. *Nat. Commun.* **6**, 8921 (2015).

71. Gómez-Graña, S. et al. Surfactant (Bi)Layers on Gold Nanorods. *Langmuir* **28**, 1453 (2012).

72. Hore, M.J.A. et al. Probing the Structure, Composition, and Spatial Distribution of Ligands on Gold Nanorods. *Nano Lett.* **15**, 5730 (2015).

73. Martin, J.E., Wilcoxon, J.P., Odinek, J. & Provencio, P. Control of the Interparticle Spacing in Gold Nanoparticle Superlattices. *J. Phys. Chem. B* **104**, 9475 (2000).

74. Sau, T.K. & Murphy, C.J. Self-Assembly Patterns Formed upon Solvent Evaporation of Aqueous Cetyltrimethylammonium Bromide-Coated Gold Nanoparticles of Various Shapes. *Langmuir* **21**, 2923 (2005).

75. Pérez-González, O. et al. Optical Spectroscopy of Conductive Junctions in Plasmonic Cavities. *Nano Lett.* **10**, 3090 (2010).

76. Pérez-González, O., Zabala, N. & Aizpurua, J. Optical characterization of charge transfer and bonding dimer plasmons in linked interparticle gaps. *New J. Phys.* **13**, 083013 (2011).

77. Pérez-González, O., Aizpurua, J. & Zabala, N. Optical transport and sensing in plexcitonic nanocavities. *Opt. Express* **21**, 15847 (2013).

78. Wang, Y. et al. Substrate-mediated charge transfer plasmons in simple and complex nanoparticle clusters. *Nanoscale* **5**, 9897 (2013).

79. Wen, F. et al. Charge Transfer Plasmons: Optical Frequency Conductances and Tunable Infrared Resonances. *ACS Nano* **9**, 6428 (2015).

80. Johnson, P.B. & Christy, R.W. Optical constants of the noble metals. *Phys. Rev. B* **6**, 4370 (1972).

81. Habteyes, T.G. Direct Near-Field Observation of Orientation-Dependent Optical Response of Gold Nanorods. *J. Phys. Chem. C* **118**, 9119 (2014).

82. Maier, S.A. Plasmonics: Fundamentals and Applications (2007).

83. Novo, C. et al. Contributions from radiation damping and surface scattering to the linewidth of the longitudinal plasmon band of gold nanorods: a single particle study. *Phys. Chem. Chem. Phys.* **8**, 3540 (2006).

84. Sönnichsen, C. et al. Drastic Reduction of Plasmon Damping in Gold Nanorods. *Phys. Rev. Lett.* **88**, 077402 (2002).

85. Novotny, L. & Hecht, B. Principles of Nano-Optics (2006).

86. Xu, P. et al. Mechanistic Understanding of Surface Plasmon Assisted Catalysis on a Single Particle: Cyclic Redox of 4-Aminothiophenol. *Sci. Rep.* **3**, 2997 (2013).

87. Boerigter, C., Aslam, U. & Linic, S. Mechanism of Charge Transfer from Plasmonic Nanostructures to Chemically Attached Materials. *ACS Nano* **10**, 6108 (2016).

88. Cenens, J. & Schoonheydt, R.A. Visible Spectroscopy of Methylene-Blue on Hectorite, Laponite-B, and Barasym in Aqueous Suspension. *Clays Clay Miner.* **36**, 214 (1988).

89. Jacobs, K.Y. & Schoonheydt, R.A. Time Dependence of the Spectra of Methylene Blue-Clay Mineral Suspensions. *Langmuir* **17**, 5150 (2001).

90. Huang, Y.F. et al. Activation of Oxygen on Gold and Silver Nanoparticles Assisted by Surface Plasmon Resonances. *Angew. Chem., Int. Ed.* **53**, 2353 (2014).

91. Zhao, L.B. et al. Surface Plasmon Catalytic Aerobic Oxidation of Aromatic Amines in Metal/Molecule/Metal Junctions. *J. Phys. Chem. C* **120**, 944 (2016).

92. Redmond, R.W. & Gamlin, J.N. A Compilation of Singlet Oxygen Yields from Biologically Relevant Molecules. *Photochem. Photobiol.* **70**, 391 (1999).

93. Tardivo, J.P. et al. Methylene Blue in Photodynamic Therapy: From Basic Mechanisms to Clinical Applications. *Photodiagn. Photodyn. Ther.* **2**, 175 (2005).

Chapter Four:

4 Plasmon-Enhanced Autocatalytic N-Demethylation of Methylene Blue[2]

4.1 Abstract

Many studies in the last decades have been indicated that optically excited plasmonic metal nanoparticles can drive photochemical reactions at photon flux comparable to that of solar radiation. However, evidences that provide insight into the mechanism of the reactions on plasmonic surfaces has been limited. Here, using plasmon-enhanced N-demethylation (PEND) of methylene blue (MB) as model reaction, we report mechanistic analysis of photochemical reactions on plasmonic gold nanoparticles under different adsorption and atmospheric conditions using surface-enhanced Raman scattering as operando spectroscopy to monitor the reaction as a function of exposure time to the light source. We found that in air and oxygen atmospheres and in the presence of co-adsorbed water molecules, MB undergoes photochemical N-demethylation to yield thionine (complete N-demethylation product) and other partial N-demethylation products that have distinct vibrational signatures. The product signals are negligible when the MB-particle system is illuminated in nitrogen atmosphere. Consistent with the well-studied mechanism in solution, the PEND reaction appears to be initiated by singlet oxygen generated via energy transfer from the excited state of MB to oxygen molecule, and therefore the reaction may tentatively be described as an autocatalytic photochemical process. The results of this study

---

[2]This chapter is adapted from: **Tefera E. Tesema**, Bijesh Kafle and Terefe G. Habteyes, *J. Phys. Chem. C*, **2019**, 123, 14, 8469-8483, Invited Feature Article, and **Tefera E. Tesema**, Christopher Annesley, and Terefe G. Habteyes, *J. Phys. Chem. C,* **2018,** 122, 19831.

provide an important insight that electronic excitations of adsorbates pumped by the localized surface plasmon field can lead to selective reaction pathways.

4.2 Introduction

Localized surface plasmon resonances of metal nanoparticles can drive photochemical reactions[1] and enhance spectroscopic signals[2] simultaneously, combining surface chemistry and operando spectroscopy to obtain fundamental understanding of surface-molecule interaction and heterogeneous catalysis[3-6] by probing the light-driven chemical and physical processes in situ. There has been increasing research interest in photochemical reactions on optically excited plasmonic metal nanoparticles.[7-19] The mechanism of the reactions on the plasmonic nanoparticles can vary depending on many factors. Excitation of surface plasmon resonances generates hot charge carriers[20] that can initiate chemical reactions,[21, 22] and at the same time the plasmon resonances can cause local heating[23-26] that may assist the surface reaction.[27-29] Surface-bound ligands that are inherent to colloidal metal nanoparticles can play critical role in mediating charge-transfer and reaction pathways.[30] In cases where the plasmon resonance frequency overlaps with the electronic transition energy of the adsorbate, the intense plasmon local field can enhance the rate of photoexcitation of adsorbate states[13, 31, 32] that can lead to generation of reactive species, such as singlet oxygen,[33-36] which is known to initiate chemical transformation of organic molecules.[37, 38] It has also been reported that photoexcitation of small metal nanoparticles as well produces singlet oxygen directly.[39, 40] In addition, the involvement of excited oxygen in plasmon-driven photochemical reactions are well documented in literature.[8, 41] The mechanisms of photochemical reactions on plasmonic metal nanoparticles are mainly discussed in terms of hot electron transfer to adsorbates, as detailed in several recent

reviews.[1, 22, 42, 43] Particle-molecule charge-transfer processes have been studied intensively in the mechanism of surface-enhanced Raman scattering (SERS), focusing on molecules that are chemically linked to the surface through specific atoms, such as nitrogen, sulfur, or oxygen.[44-47] On the other hand, the involvement of hot electrons in photochemical reactions is broadly implied even when there is no certainty in the adsorption geometry. For example, resonant charge transfer excitation to unoccupied electronic state of methylene blue (MB) adsorbed on silver nanocube has been claimed based on an assumption that MB is chemically bonded to Ag through the N atom in the thiazine ring in a butterfly orientation.[48, 49] With this geometry, it has been implied that 785 nm excitation is in resonance with charge transfer state of the Metal-adsorbate system and this leads to faster rate of photochemical transformation than at 532 nm excitation source even though it has stronger spectral overlap with intense LSPR associated with the dipolar mode of single silver nanocube. However, theoretical calculations show that MB adsorbs on gold and silver through weak dispersion forces, where the molecule orients flat and parallel to the surface.[50-52] Furthermore, there are disagreements in vibration bands obtained at 532 and 785 nm excitation wavelengths provided in Table 1 of ref [48, 49], which is a clear indication of complete N-demethylation of MB adsorbed on plasmonic nanoparticles at 532 nm excitation.[16, 53] Hence, the claim that resonance charge transfer excitation mechanism at 785 nm excitation wavelength result in selective photochemical transformation lacks strong experimental evidence. This suggests the critical importance of other factors and processes, such as near-field-enhanced electronic transition of adsorbates. In fact, it has recently been demonstrated that the dissociation of $(CH_3S)_2$ on

gold and silver nanoparticles is initiated by plasmon-pumped electronic transition of the adsorbate.[13]

Herein, we use plasmon-enhanced N-demethylation of MB (PEND-MB) as model system to shed light on the underlying physical mechanisms leading to photochemical reactions on resonantly excited plasmonic gold nanoparticles. From our previous work reported in **Chapter 3**, we know that PEND-MB on gold nanoparticles takes place when the excitation energy overlaps with both the electronic transition energy of the molecule and the plasmon resonance of the nanoparticles.[16] However, it was difficult to propose plausible mechanism as the study was performed in open air and hence uncontrolled involvement of atmospheric gases. Here, we systematical investigated the mechanism of the photochemical N-demethylation on resonantly excited gold nanoparticles in reactive (air and oxygen) and inert (nitrogen) atmospheres at different adsorption conditions. We find that in air and oxygen atmospheres and in the presence of co-adsorbed water molecules, PEND-MB to yield thionine (TH) and other intermediate N-demethylation products (Azure A and Azure B) that exhibit distinct vibrational bands in the SERS spectra. The photochemical reaction does not take place in nitrogen atmosphere. Consistent with the N-demethylation initiated by thermally generated singlet oxygen in solution phase chemistry,[38, 54, 55] the mechanism of the PEND-MB on gold nanoparticles may be initiated by singlet oxygen that can be generated via energy transfer from triplet excited state of MB to triplet ground state oxygen. Since the proposed mechanism involves generation of singlet oxygen by the reactant (MB) itself, it may be described as an autocatalytic chemical process. Only N-demethylation products are detected in our experiment, indicating plasmon-pumped electronic excitations of adsorbates can selectively affect specific chemical bonds.

4.3 Results and Discussion

4.3.1 Plasmon-enhanced photochemistry in ambient condition

Under this sub-section the author presents photochemistry of MB and its N-demethylation analogue under normal (ambient) atmospheric condition. The section starts with the absorption of the dyes in solution and scattering spectrum of gold nanorod film deposited on a cover glass. Then the section follows with the comparison of Raman spectra of each dye with corresponding initial SERS. The subsequent spectra are presented after proper background correction procedures to get comprehensive analysis of the temporal evolution SERS signals under different atmospheric conditions. Same procedure will be applied through the chapter.

4.3.2 Scattering spectrum of gold nanorods and absorption spectra of methylene blue and its N-demethylation derivatives

The chemical and structural properties of methylene blue and its N-demethylated derivatives are described in detail in **section 2.3.1** of **chapter 2**. **Figure 4.1** shows the absorption bands of aqueous solutions of MB and its N-demethylated derivatives.

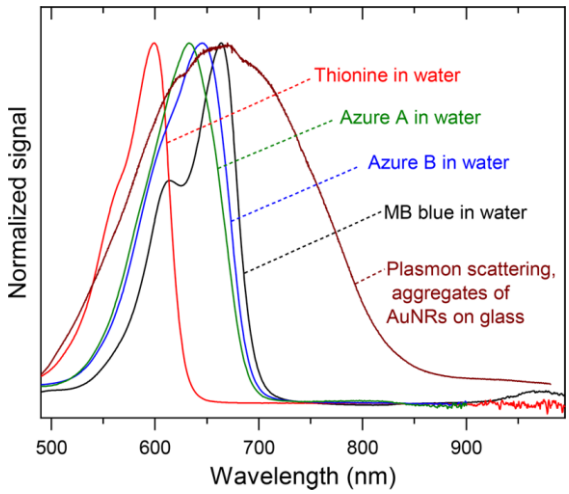

Figure 4.1 The absorption spectra of MB, azure B, azure A, and thionine in water and the plasmon scattering spectrum of AuNRs (Diameter 40 nm and length 90 nm) aggregated on coverslip

MB in aqueous solution had an absorption peak at 663- 664 nm and a molar extinction coefficient in this peak equal to $9.0x10^4$. The N-demethylated derivatives of MB (Azure A (AZA), Azure B (AZB), and Thionine (TH)) have also strong absorption bands in the visible region of electromagnetic spectrum. The scattering spectrum shown by the brown line in **Figure 4.1** shows that the plasmon resonances of AuNRs (∼40 nm diameter and ∼90 nm length) aggregated on a cover glass overlap with the entire absorption bands of MB and its N-demethylation derivatives. Adsorption on metal surface perturbs the electronic structure of the adsorbates and induces peak energy shift and line width broadening to an extent that depends on the nature of the surface−molecule interaction compared to that in solution and isolated molecules.[47, 56, 57] These adsorption effects cause red shift and hence more significant overlap of the excitation wavelength with the absorption band of TH. Similarly, the adsorption effect improves the extent of overlap of the absorption band of MB with the excitation wavelength (632.8 nm laser) and the broad aggregated nanoparticle surface plasmon resonance.[47, 57]

4.3.3 Raman and SERS spectra of MB and its N-demethylation derivatives

The significant overlap of the excitation wavelength (632.8 nm laser) with adsorbate absorption bands and LSPR of gold nanorods depicted in Error! Reference source not f ound.**,** enormously amplifies the SERS cross-section of MB (reactant) and TH (product) due to resonance Raman and electromagnetic enhancement effects plus the absence of sharp and strongest Raman spectrum of TH at 479 cm^{-1} in that of MB makes SERS very suitable to monitor the plasmon-enhanced photochemical reaction. In addition, the Raman vibrational spectra of azure B and azure A display characteristic features that can be used to identify these species if they are formed due to partial N-demethylation of MB. In the

following section, we use these spectral contrasts between reactant and product species to investigate the effects of atmospheric and adsorption conditions on the photochemical reaction.

For MB and its N-demethylated derivatives on the gold surface, the surface−molecule interaction is dominated by weak dispersion forces as recent theoretical calculations indicate.[52] Consistent with the physisorption nature of the interaction, the peak positions in the SERS spectra agree very closely with the corresponding peak positions in the regular Raman spectra of powders as shown in **Figure 4.2**. The data are obtained at 633 nm excitation wavelength, and the SERS signals for MB and its derivatives (azure B, azure A, and thionine) are comparably strong suggesting similar contribution of molecular resonance effects as the spectral broadening upon adsorption can lead to the overlap of the excitation wavelength with the absorption bands for all the adsorbates. As a result, the reactant and product species can be monitored with high sensitivity by taking advantage of the large SERS cross-section that results from resonance Raman and electromagnetic enhancement effects as discussed in **section 4.2** above.[45, 58-60]

In the discussion of PEND-MB photochemical reaction, the spectra presented in **Figure 4.2** will be used as reference. The prominent peaks at **479** and **804** cm^{-1} in the TH spectrum can be used to quantify the complete N-demethylation and the downshift of the 1435 cm^{-1} peak will be used to ascertain partial N-demethylation MB.

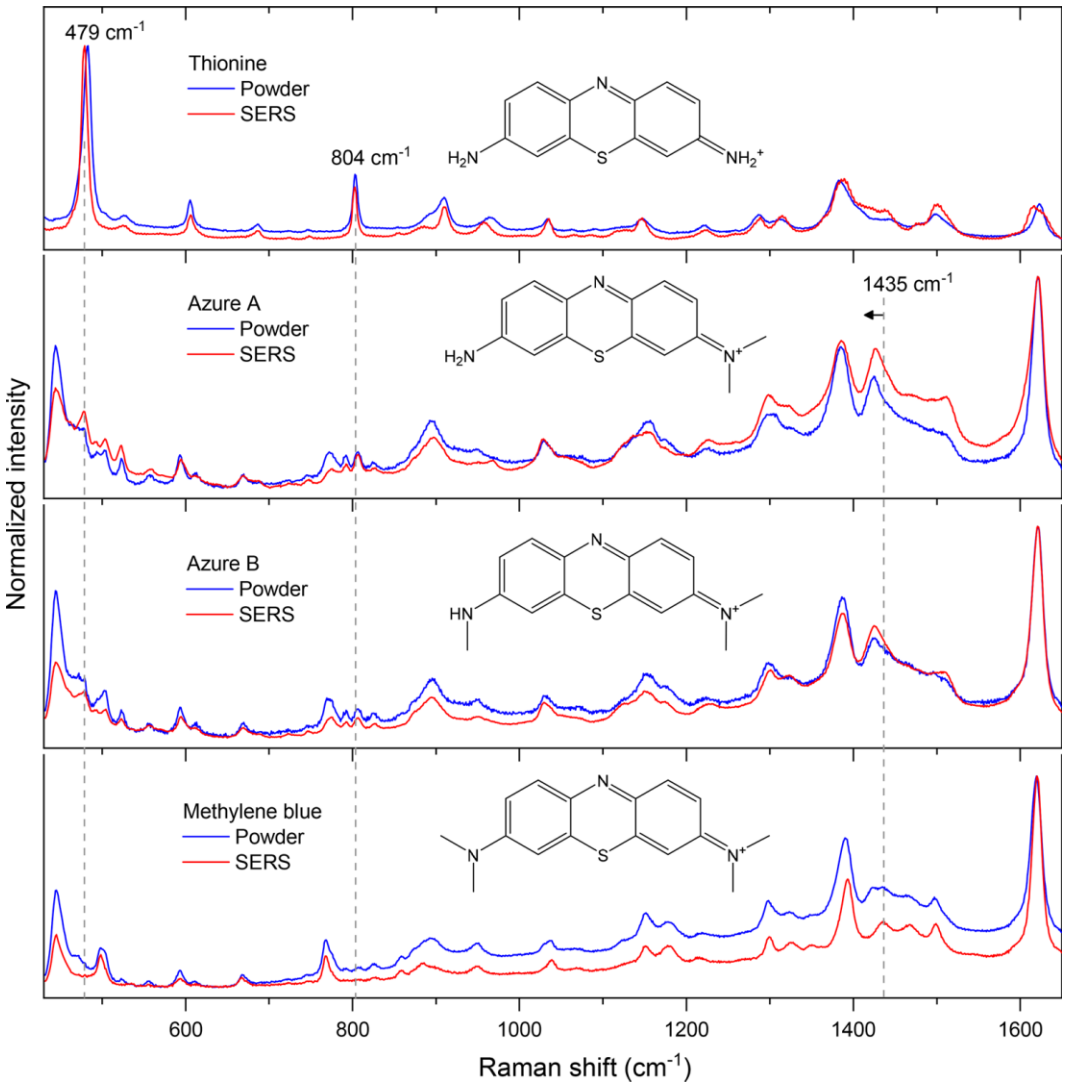

Figure 4.2 Normal Raman spectra of solid powders (blue lines) and SERS spectra (red lines) of methylene blue, azure B, azure A, and thionine as labeled.

The data in **Figure 4.3**. Show temporal evolution of MB SERS spectra obtained under continuous illumination of 632.8 nm excitation wavelength in ambient atmosphere at room temperature. The change is Prominent when the spectra recorded at 0.5 and 200 s exposure times are compared (see **Figure 4.3**a). The intensity map (**Figure 4.3**b) that represents 400 spectra acquired sequentially shows the appearance of new vibrational bands as a function of exposure time. Based on the SERS and Raman spectra of the reactants in the initial state, the spectral changes can be interpreted as follows.[61](1) The new peak that appears at **479**

cm^{-1} can be assigned to the skeletal deformation mode of TH (product). (2) The new peak at **804 cm^{-1}** can be assigned to the NH_2 rocking vibration that requires complete N-demethylation of MB at least at one N-atom terminal of the dimethyl amine groups.

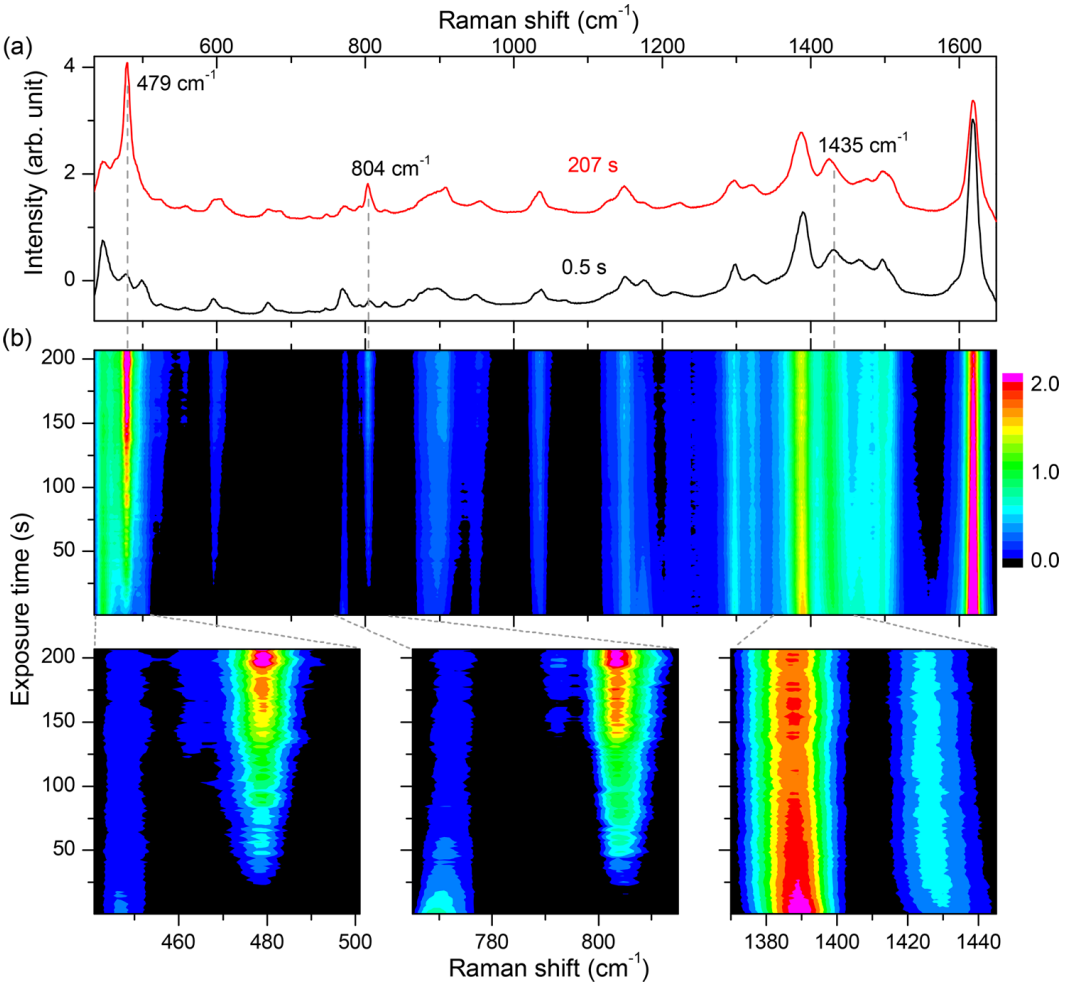

Figure 4.3 *Temporal evolution of SERS spectra demonstrating PEND-MB. (a) Representative SERS spectra recorded in ambient atmosphere at the beginning (black line) and after 200 s of illumination using 633 nm excitation wavelength. (b) Intensity map representing 400 spectra acquired sequentially during illumination for about 207 s. The zoom-in intensity maps at the bottom show the important spectral changes with time. Each spectrum is recorded with 0.5 s acquisition time at 0.4 mW incident power focused with 0.7 NA objective.*

(3) The red-shift from the **1435 cm^{-1}** initial peak position can be attributed to partial N-demethylation products that include azure B, azure A, and azure C. We note that the

prominent vibrational bands at 479 and 804 cm^{-1} are completely absent in the MB spectrum (see **Figure 4.3**), providing high contrast for reactant and product signals.

So far, we discussed the results of PEND-MB obtained at ambient conditions. To develop a more comprehensive understanding of the mechanism of PEND-MB, we have performed experiments under different combination of atmospheric and adsorption conditions. These controlled experiments provide deep insight into the mechanism of photochemistry and develop a greater understanding of the role of atmospheric gases and adsorption condition in the partial or complete N-demethylation processes.

4.4 Photochemical reaction in reactive and inert atmosphere

The photochemical reaction progress is monitored by recording the SERS spectra continuously as a function of exposure time. However, in addition to the vibrational signals, the fluorescence background changes with exposure time as illustrated in panels (a) and (b), **Figure 4.4**. To facilitate comparison of relative intensity (*I*) of vibrational bands, the fluorescence background is removed using the following relation.

$$I_{corrected} = \frac{I(t) - I_b(t)}{I_b(t)} \qquad 4.1.$$

Where $I_b(t)$ represent time dependent background signal. A flat spectral position labeled 1, 2, and 3 in **Figure 4.4**a were chosen as background signal and the baseline of the spectrum acquired at beginning (0.5 s, black line) is higher than that obtained after exposure of sample to laser source for about 207 s (red line). **Figure 4.4b** show a decreasing in the background signal with time. After the background

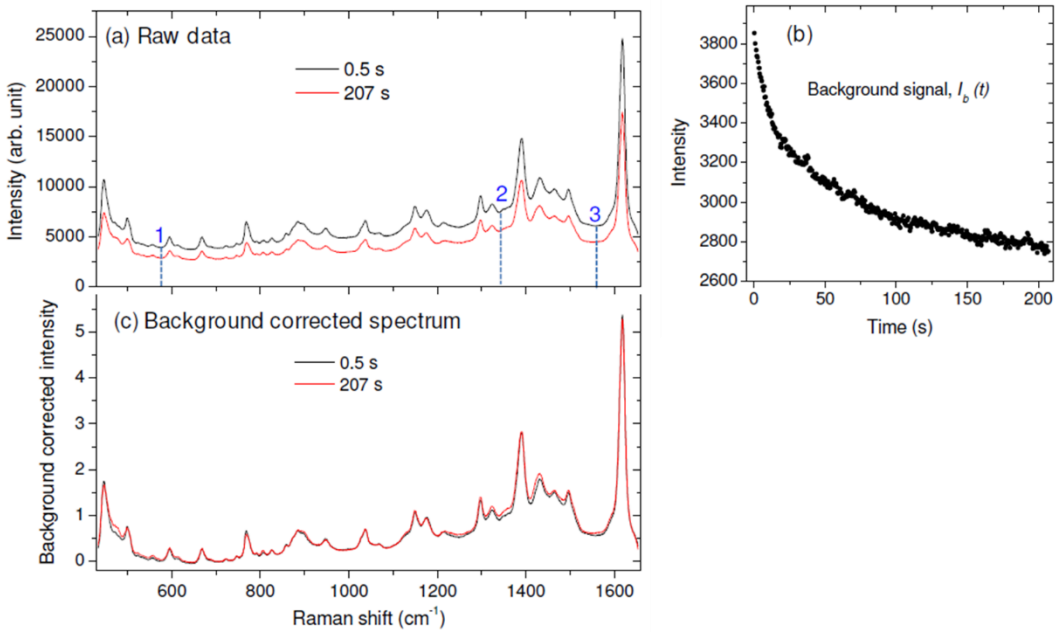

Figure 4.4 Illustration of background signal change as a function of continuous illumination. (a) Spectra at the beginning of illumination (black line) and after 207 seconds (red line). (b) Time dependence of the background signal where there is no vibrational band (at position ~707 cm^{-1}). The trend is the same if other locations labeled 1, 2 or 3 in (a) are used. (c) The spectra acquired at 0.5 s and 207 s exposure time after background correction

The SERS spectra presented in **Figure 4.4** are obtained in N_2 atmosphere. In air and oxygen atmospheres, the background signal decreases with slightly different rates in the different regions of the spectral window. To avoid any bias this background asymmetry may cause in comparing the time dependence of different vibrational band intensities, background reference points close to the bands are used. For example, for the band at 479 cm^{-1}, the position marked as 1 in **Figure 4.4** (a) is used as background reference point. Similarly, position 2 is used for bands at 1392 cm^{-1} and 1435 cm^{-1}, and position 3 is used for the band at 1620 cm^{-1}.

The photochemistry of MB on plasmonic surfaces is studied at room temperature in a closed chamber (Warner Instruments Inc., RC-21B, see chapter 2 method section for detail)

that is sealed by bare coverslip from the top side and sample containing coverslip (with the sample side facing upward) from bottom side of the chamber, as illustrated by the schematics in **Figure 4.5**. The coverslips are placed on the recessed grooves to which vacuum grease is applied to create a tight seal of the coverslips. SERS measurements are performed at ambient atmosphere, or under continuous flow of pure O_2 or N_2 gas. At the chamber output, a length of tube is used as a back-pressure control to ensure smooth flow of gases. The importance of water molecules in the gas phase is studied by expanding the N_2 or O_2 gas through a bubbler filled with ultrapure water. The photochemical reaction is initiated using 632.8 nm excitation wavelength that overlaps with the plasmon resonances of the gold nanoparticles and electronic transition energy of MB. The reaction is monitored using SERS signal of the reactant and product species by collecting the scattered light through the coverslip using 0.7 NA objective. About 90% of the signal collected from the sample is directed to a spectrometer (IsoPlane Spectrograph of Princeton Instruments) that uses thermoelectrically cooled (−75 °C) and back illuminated deep depletion charge-coupled device camera, whereas the remaining 10% of the signal is directed to the Olympus UC30 camera attached to the GX51 microscope for monitoring the focus and inspecting the sample. The comparison of Stokes and anti-Stokes Raman intensities was carried out using our atomic force/near-field microscope that has been described elsewhere,[62, 63]but the same spectrometer mentioned above is used for detection (see chapter 2 for detail).

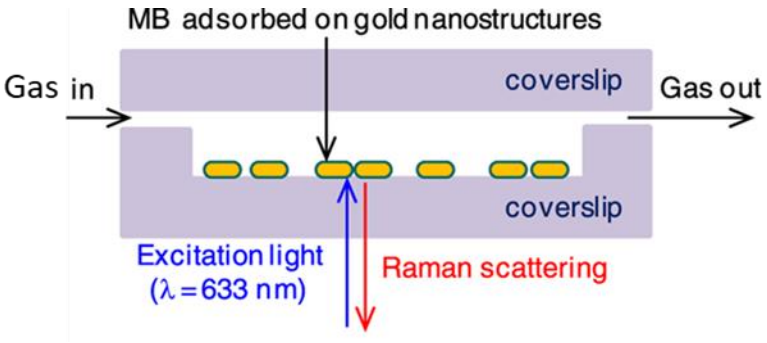

Figure 4.5 Schematic showing the experimental setup of the photochemical reaction under the flow of different gases over the solid thin film of sample (MB adsorbed on gold nanostructures).

The results on the PENDMB discussed so far are obtained at ambient conditions. Mechanistic understanding of the reaction requires determining all the reactants by controlling the atmospheric condition. To this end, we have performed the photochemical reaction under reactive (in pure oxygen and air) and inert (in nitrogen) atmospheres.[61, 64] To compare this, we have acquired and compiled the temporal evolutions of SERS data at different atmospheric conditions as shown in **Figure 4.6**.

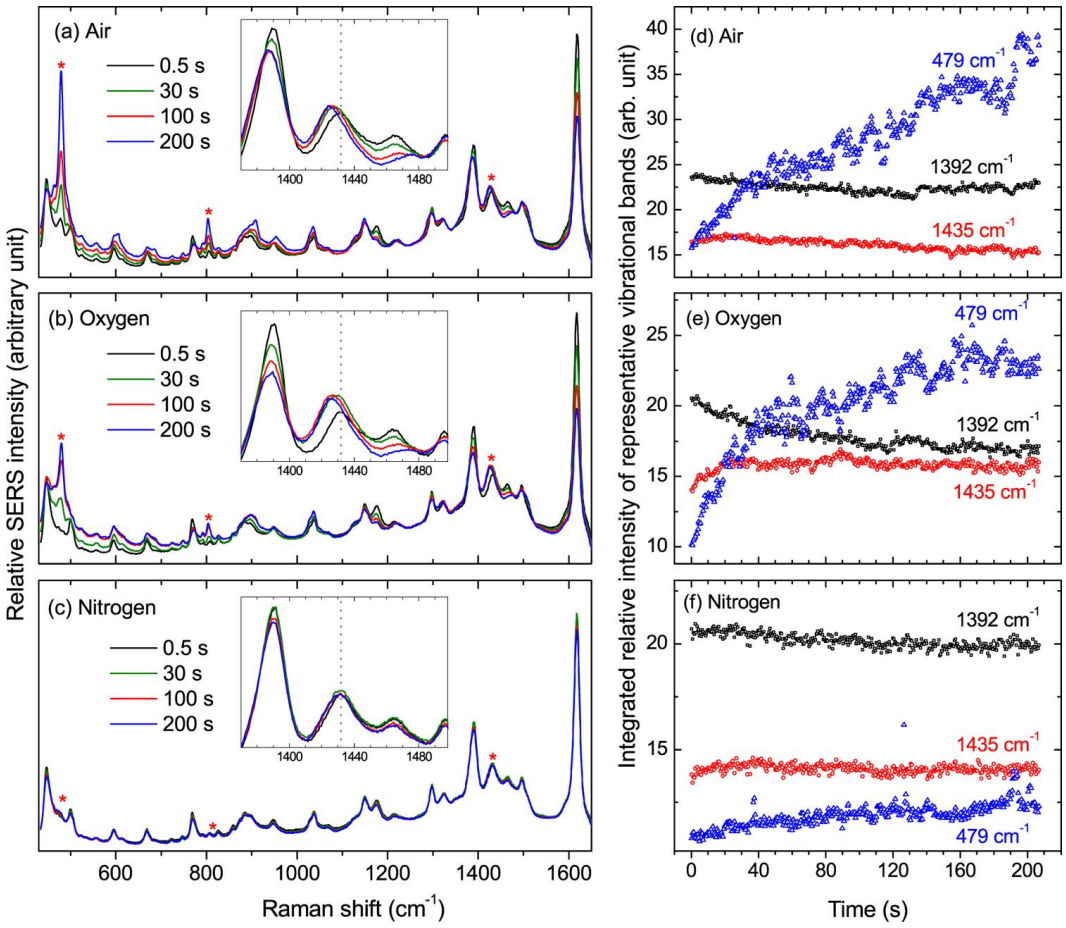

Figure 4.6 Temporal evolution of the SERS signal of MB adsorbed on AuNRs and illuminated with 0.4 mW of 633 nm CW laser (focused with 0.7 NA objective) in air (a, d), oxygen (b, e), and nitrogen (c, f) atmospheres. The SERS spectra are acquired continuously with 0.5 s acquisition time for over 200 s of continuous illumination, and the black, green, red, and blue lines in (a)−(c) represent average spectra of at least 10 different spots on the same sample at different exposure times, as labeled. (d) & (f) Integrated intensities of representative vibrational bands plotted as a function of exposure time.

The data in **Figure 4.6** (a,b) show similar results in ambient and oxygen atmosphere in that new prominent peak at 479 cm^{-1} and 804 cm^{-1} appear and grow with time upon continuous exposure of sample to the excitation source. In contrast, those collected in nitrogen atmosphere, the intensities at the corresponding peak positions are within the background level (see **Figure 4.6**c) indicating the involvement of oxygen in the PEND reaction. We have selected new (479 cm^{-1}) and original (1392 cm^{-1} and 1435 cm^{-1}) representative

vibrational bands and plotted integrated intensities of the band peaks as a function of time (**Figure 4.6**(d-f)). We use 1392 cm^{-1} as a reference in this analysis because it has comparable signal intensity in both the reactant (MB) and the product (TH). Data in **Figure 4.6**(d, e), show that intensity of band corresponding to TH (the complete N-demethylation product) increases with time and becomes higher than that of the 1392 cm^{-1} band after about 40 s in the reactive atmospheres. However, in the inert (nitrogen) atmosphere, the relative intensity at the 479 cm^{-1} band remains within the background level during the continuous illumination of the sample (**Figure 4.6**f), This confirms that conversion of MB to TH is negligible in the absence of oxygen.

For more detailed analysis of the photochemical transformation, we zoomed into spectral region containing representative signal from reactant and product and compared the signal intensity in specific time in a given experiment runtime i.e. first spectrum (0.5 s) with last spectrum in the run (207 s). The rise in the intensity (concentration) of the thionine correlates well with the decrease in the intensity (concentration) of methylene blue as a function of exposure time in different atmospheres as reactant to product (**Figure 4.7**).

SERS vibrational mode at 1435 cm^{-1} red shifts with increasing exposure time, and the shift is accompanied by a relative intensity increase depending on the atmospheric condition. This vibrational mode has been assigned to the in-plane NCH bending vibration of MB[65] and, therefore, should disappear upon complete N-demethylation.

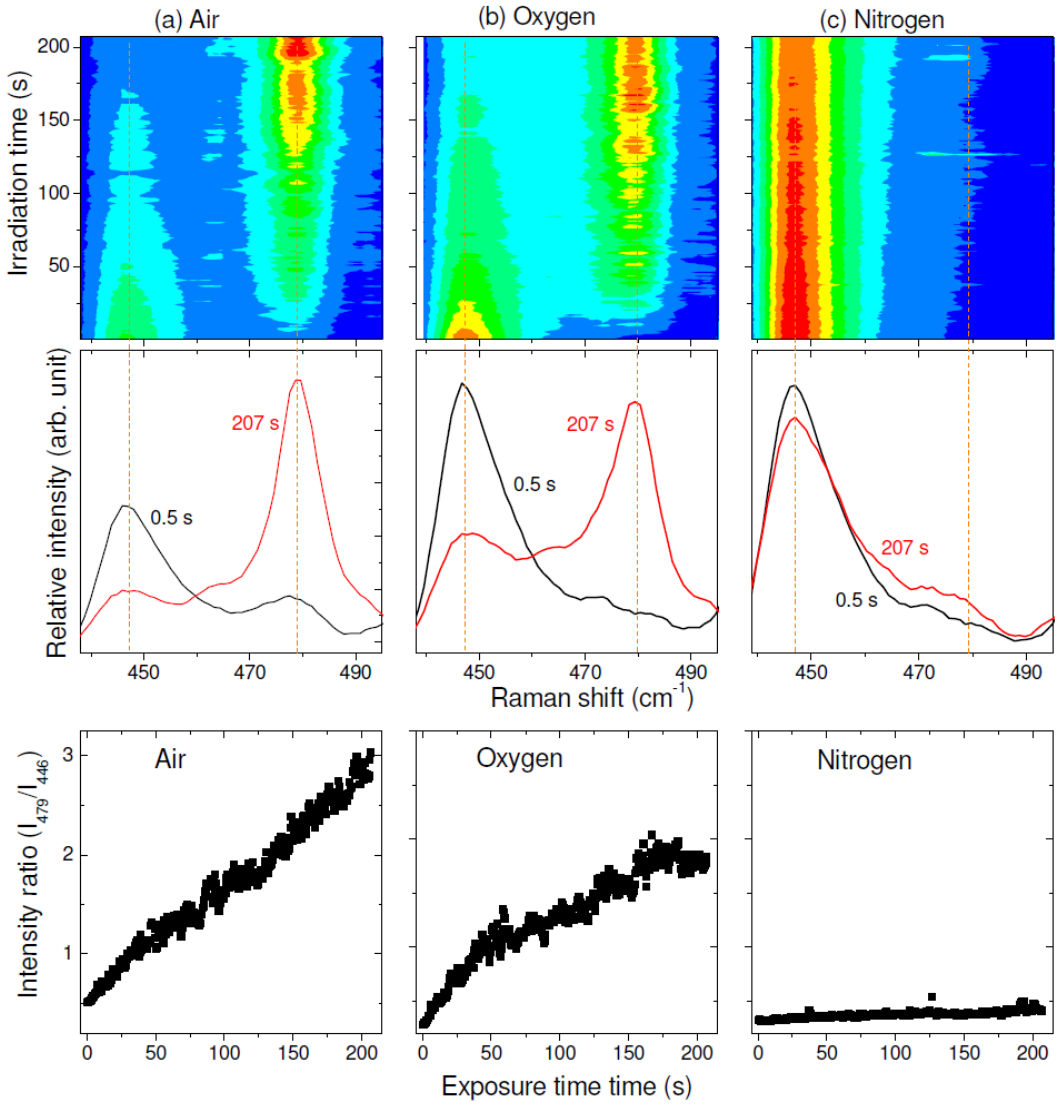

Figure 4.7 Top panels: Intensity map representing 400 spectra showing the decline of MB reactant signal at 446 cm-1 and growth of thionine product signal at 479 cm-1 as a function of exposure time in (a) air, (b) oxygen and (c) nitrogen atmospheres. Middle panels: spectra showing the relative intensities of the 446 cm-1 (reactant) and 479 cm-1 (product) peaks at the beginning (black line) and end (red line) of illumination for 207 seconds in air, oxygen and nitrogen atmospheres. Bottom panels: product to reactant peak intensity ratios in air, oxygen and nitrogen atmospheres.

Hence, the frequency red shift and intensity rise with exposure time can be attributed to partial N-demethylation products such as azure B, azure A, or azure C, which is consistent with the reference spectra shown in **Figure 4.2**

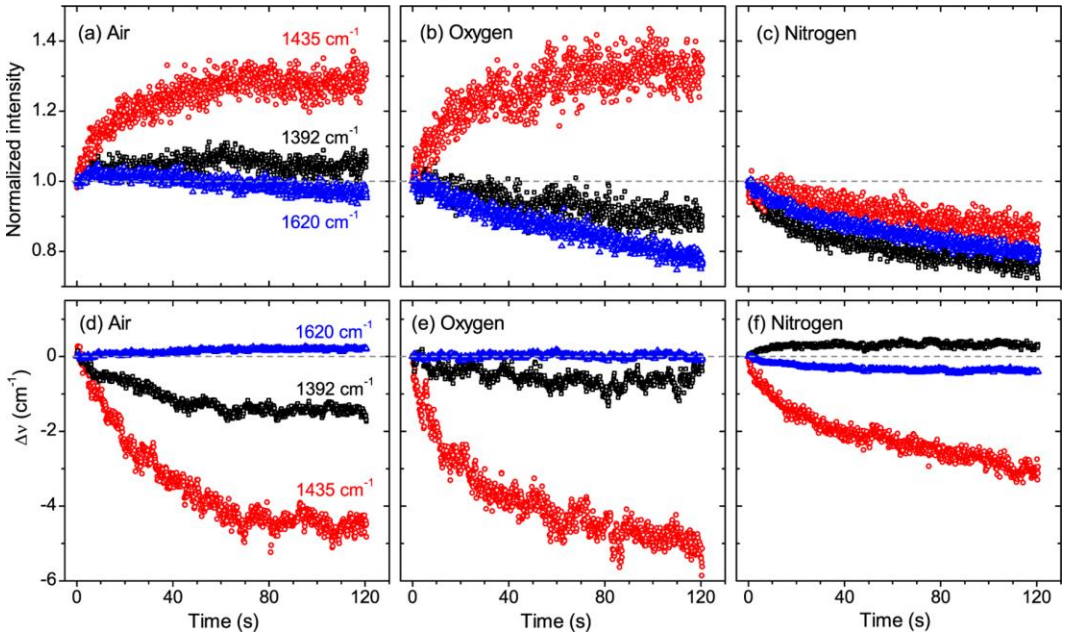

Figure 4.8 (a−c) Integrated and normalized relative intensities of representative vibrational bands plotted as a function of exposure time in (a) air, (b) oxygen, and (c) nitrogen atmospheres. (d−f) Vibrational frequency shift of the different bands as labeled based on the initial peak frequencies. The peak vibrational frequencies are determined by fitting a Gaussian function to the spectra. The integrated intensities and frequencies are extracted from 1000 spectra each recorded with 0.1 s acquisition time within 120 s of continuous exposure time using 0.2 mW of 632.8 nm CW laser that is focused with 0.7 NA objective.

For more comprehensive analysis of the partial N-demethylation, we have closely analyzed the integrated intensities and frequency shifts of the representative bands plotted in **Figure 4.8**. In air and oxygen atmospheres, the relative intensity of the 1435 cm^{-1} band increases with exposure time, whereas that of the other selected bands remains nearly constant in air and decreases slightly in oxygen as shown in **Figure 4.8**(a, b). For peak, the intensity rise is accompanied by significant frequency red shift depending on the atmospheric conditions

(**Figure 4.8**(d-f)).Within 120 s exposure time, red shifts of about 5 and 3 cm^{-1} are observed in reactive and inert atmospheres, respectively. Again, based on the reference spectra discussed in above, the frequency shift is attributed to partial N-demethylation of MB. The shift in the nitrogen atmosphere indicates non-negligible reaction possibly due to the presence of trace amounts of oxygen as adsorbate.

In nitrogen atmosphere, the relative intensities of all the bands decrease gradually with exposure time. However, it is interesting to note that the intensity decline for the 1435 cm^{-1} band is the slowest, whereas the decline rates for 1392 and 1620 cm^{-1} bands are reversed in nitrogen atmosphere from that in air and oxygen. The reversal of the intensity trend for the 1392 and 1620 cm^{-1} is also observed in the frequency shift as we go from air/oxygen to nitrogen. The 1620 cm^{-1} vibration mode, which is due to stretching vibrations of the CC and CN bonds of the fused aromatic ring,[66] slightly blue shifts in air, remains nearly constant in oxygen, and red shifts in nitrogen atmosphere. In addition, the 1392 cm^{-1} mode of the CN stretching vibration of the $-N(CH3)_2$ functional groups coupled to that of CN and CC of the fused aromatic ring[66] red shifts in air and oxygen compared to slight blue shift in nitrogen atmosphere. That is, in nitrogen atmosphere, the 1392 and 1620 cm^{-1} bands shift in opposite direction by about the same magnitude, albeit the shifts are very small (see **Figure 4.8**). This trend is reproducible at low laser intensity in nitrogen atmosphere (**see appendix A 3 for a different sample**), and it may be attributed to light-induced surface−molecule interaction[45] and stark effects.[67] The effect disappears when the incident laser power is increased possibly due to the overwhelming effect of the photochemical N-demethylation. For the 1435 cm^{-1} band, partial N-demethylation and light-induced surface−molecule interaction may shift the peak position in the same

direction. However, as mentioned earlier, based on the agreement between the peaks position in the SERS and normal Raman spectra of solid powders and hence the frequency shift due to light-induced surface-molecule interaction may not be significant. Therefore, the substantial frequency shift observed for the band that initially peaks at 1435 cm^{-1} can be attributed to partial N-demethylation due to the presence of trace amount of adsorbed oxygen molecules in the system. If there was strictly no demethylation reaction occurring, the shifts for the bands that initially peak at 1392 and 1620 cm^{-1} might be more significant.

The data in **Figure 4.9** provide more evidences for the association of partial N-demethylation process with the observed relative intensity and frequency shifts. In this experiment, we have measured SERS of MB (N,N,N',N'-tetramethylthionine) and AZB (N,N,N' N'-trimethylthionine) in nitrogen atmosphere. As illustrated in **Figure 4.9**, the peak at 1386 cm^{-1} and 1426 cm^{-1} of AZB appear to the red side of the corresponding frequency of MB (1392 cm^{-1} and 1435 cm^{-1}), which is in good agreement with the frequency shifts observed (**Figure 4.8**) due to photochemical conversion of MB in in air and oxygen.

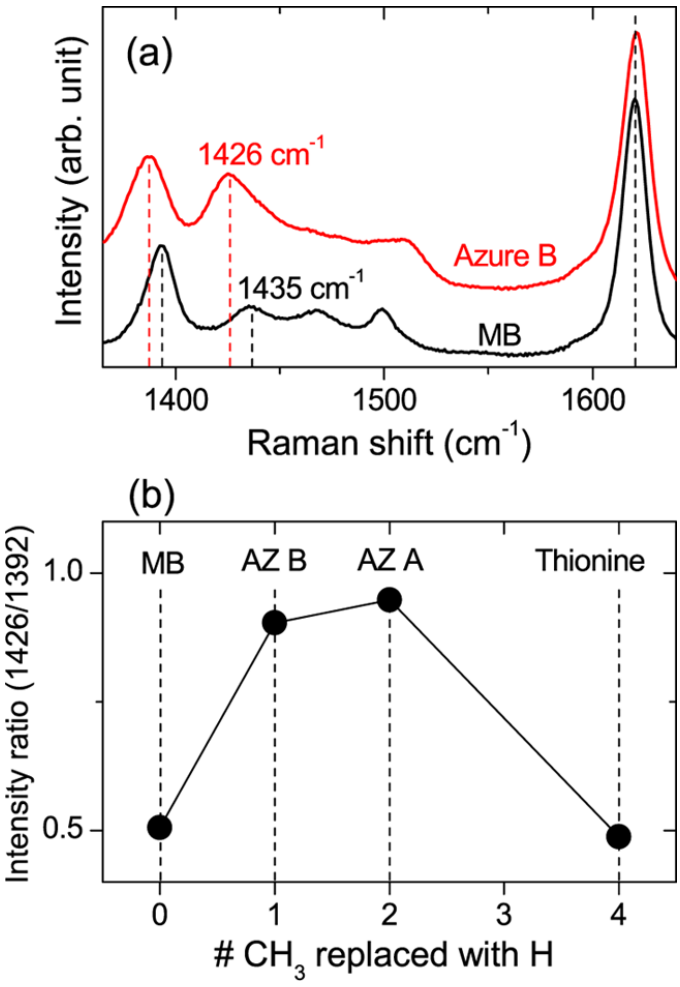

Figure 4.9 (a) SERS spectra of methylene blue (black line) and azure B (red line) recorded at 0.4 mW of 633 nm CW laser and 0.5 s acquisition time in nitrogen atmosphere. The spectra are recorded one after another at the same optical settings so that exactly the same reference point is used in determining the Raman shifts for the two compounds. (b) Ratio of the intensity at 1426 cm^{-1} to the peak intensity at ~1392 cm^{-1} (MB) or ~1386 cm^{-1} (azure B, azure A, and thionine).

4.5 Effect of spacer layer on photochemical N-demethylation

In an effort to develop the dependence of photochemical N-demethylation on the energy of the excitation source we observed that the1424 cm^{-1} to 1392 cm^{-1} peak intensity ratio is higher for MB adsorbed on gold spheres with citrate surface ligand than that on AuNRs with CTAB surface ligand (see chapter 3). This observation suggests that the adsorption on gold spheres favors partial N-demethylation as can be inferred based on the patterns in

reference spectra above. To obtain further evidence, the SERS properties of MB adsorbed directly on the on bare gold nanoisland (AuNI) prepared using electron-beam evaporation (MB-Au) are compared with that obtained by adsorbing on similarly prepared gold nanostructures coated with a monolayer of poly(sodium4-styrenesulfonate) (MB-PSS-Au) as shown in **Figure 4.10**. For the MB-Au sample, two peaks at 1421 cm^{-1} and 1435 cm^{-1} are observed, and the relative intensity of the 1421 cm^{-1} increases with exposure time. Whereas for the MB-PSS-Au sample, the 1421 cm^{-1} peak has shifted to ~1426 cm^{-1}, and its relative intensity increases with exposure time. Based on the results presented in **section 4.3.3** above, the 1426 cm^{-1} peak position can be assigned to azure B or C, and the red shift to 1421 cm^{-1} for the MB-Au sample can be attributed to surface-molecule interaction because of direct coupling to the gold surface.

As shown in **Figure 4.10**, the intensity ratio of the 1421 cm^{-1} to 1392 cm^{-1} peaks for the MB-Au sample (open circles) is higher than the corresponding peak intensity ratio for the MB-PSS-Au sample (solid circles). On the other hand, the intensity ratio of 479 cm^{-1} to 446 cm^{-1} peaks is higher for the MB-PSS-Au sample (solid triangles) than for the MB-Au sample (open triangles), indicating that the conversion of MB to thionine is favored in the presence of PSS. The observation of stronger thionine product signal in the presence of PSS may indicate optimal surface-molecule proximity to minimize competing radiative and nonradiative processes as predicted by Nitzan and Brus.[31] In other words, it can be argued that the trend observed in **Figure 4.10** supports our proposed mechanism that involves plasmon-pumped HOMO−LUMO electronic transition. However, the PSS may also influence the charge carrier separation and their lifetimes.

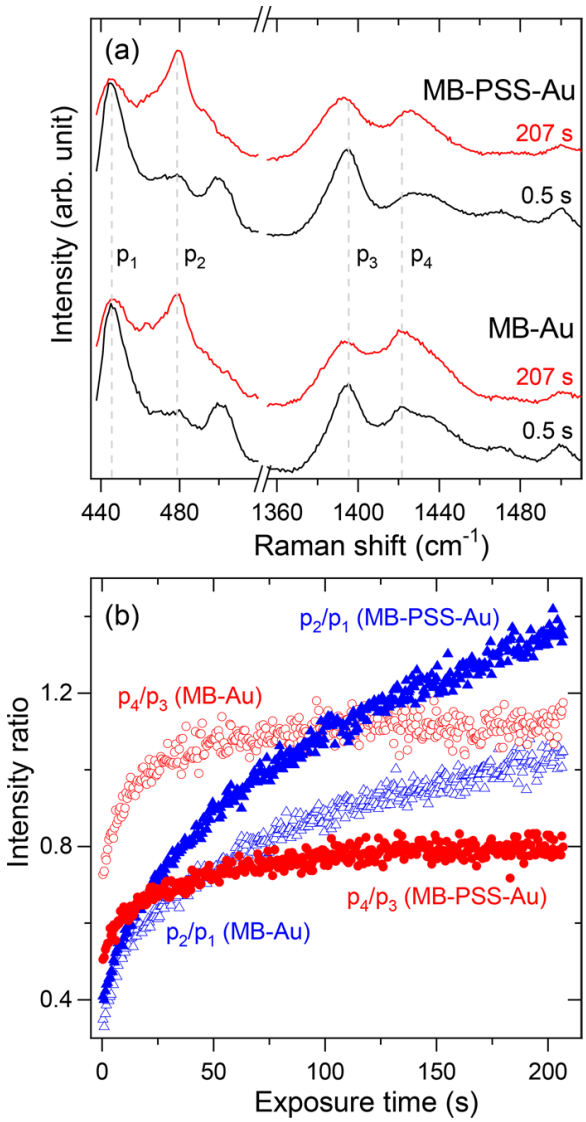

Figure 4.10 (a) Representative spectra showing the relative intensities of the peaks labeled p1−p4 at the beginning (black line) and end (red line) of illumination at 633 nm for 207 s in the presence (upper two spectra) and absence (lower two spectra) of poly(sodium 4-styrenesulfonate) (PSS) coating on e-beam evaporated gold nanostructures as labeled. Each spectrum represents an average of at least 10 different spots on the same sample. (b) Peak intensity ratios as a function of exposure time.

4.6 4.5 Effect of dehydration.

The results presented so far are for MB adsorbed on the colloidal gold nanorods and evaporated gold nanostructures in aqueous solution, which could result in the adsorption of hydrated MB in the dried sample. Adsorbed water maybe involved in the photochemical

N-demethylation reaction. To obtain experimental evidence for the involvement of water molecules in the reaction, the water molecules in the surface-molecule complex (water in the inner coordination sphere) have been minimized by suspending both the molecule and the gold nanorods in ethanol during the solution processes, and the results are summarized in **Figure 4.11**.

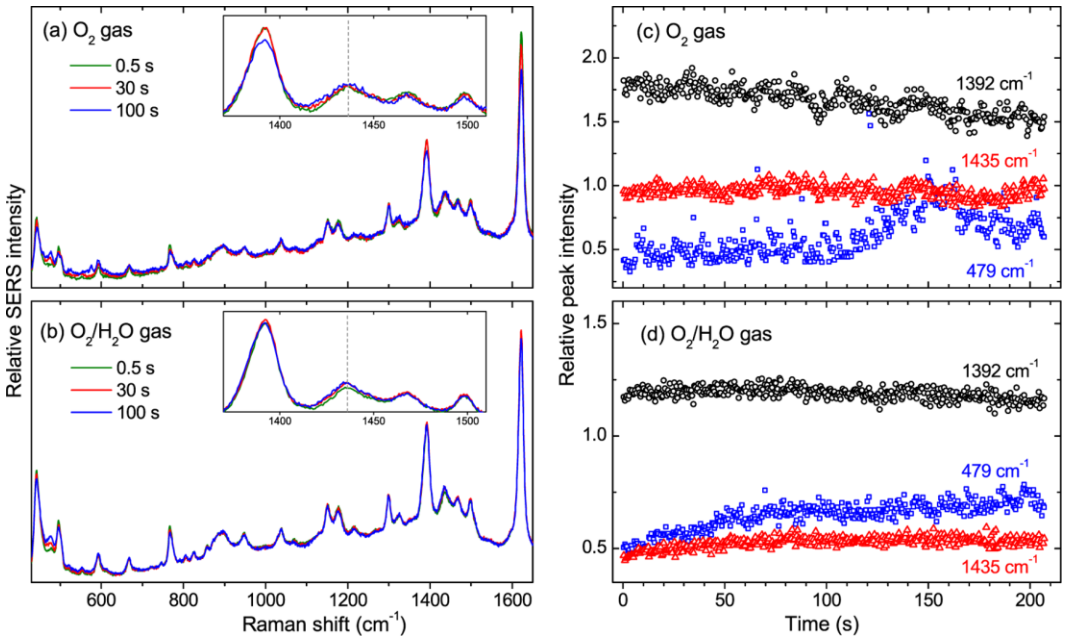

Figure 4.11 Temporal evolution of the SERS signal for dehydrated MB−AuNR complex. The amount of adsorbed water is minimized by using ethanol solution of MB and AuNRs during the sample preparation. Representative spectra acquired under the flow of (a) dry O_2 gas and (b) O_2/ H_2O gas formed by passing the O_2 gas through a water bubbler (c, d) relative peak intensities extracted from the spectra acquired under the flow of (c) dry O_2 gas and (d) O_2/H_2O gas.

We have compared the relative intensity of the bands at 479 cm^{-1} and 804 cm^{-1}, which is obtained under a flow of oxygen over dehydrated surface-molecule with the corresponding intensities obtained under the flow of oxygen over hydrated surface-molecule complex. The data in **Figure 4.11**(a) & (b) show that the N-demethylation reaction is suppressed significantly when the surface−molecule complex is dehydrated. We have repeated the

experiment after introducing water molecules in the gas phase by expanding oxygen gas through a water bubbler, and plotted representative spectra obtained under this condition as shown in **Figure 4.11**b and the vibrational signatures of thionine remain very weak in this case as well. The peak intensities plotted in **Figure 4.11**(c, d) show that the relative intensity of the 479 cm^{-1} band remains significantly lower than the intensity of the 1392 cm^{-1} band throughout the exposure time. This trend is in contrast to that observed in **Figure 4.6**(d, e) where the relative intensity of the 479 cm^{-1} band becomes larger than that of the 1392 cm^{-1} band after some time of exposure. In addition, the frequency shifts for the bands in the 1360−1450 cm^{-1} region are negligible as can be seen in the insets in **Figure 4.11**(a, b), suggesting that partial N-demethylation is also suppressed in the absence of water. The fact that vibrational signatures of N-demethylation remain weak even in the presence of water molecules in the gas phase indicate that it is the hydrated form of MB that undergoes N-demethylation reaction. In hydrated MB, water molecules are likely to be in the proximity of the −N(CH3)2 functional group because of a favorable electrostatic interaction and can be the source of hydrogen atoms that replace the methyl groups.

4.7 4.6 Mechanism of plasmon-pumped adsorbate excitation

SERS results discussed above showed that oxygen and water molecules are directly involved in the mechanism of partial or complete N-demethylation of methylene blue. The direct adsorption of MB on plasmonic metal nanostructure favor the formation of partial N-demethylation products. These photochemical processes occur when the excitation source is 632.8 nm laser and not when 532 nm and 808 nm lasers are used for excitation of the plasmonic nanoparticles. Aqueous solution of MB has absorption maxima at 664 nm and laser fairly overlap the electronic excitation of the molecule on resonantly excited

metal nanoparticle. The observation of plasmon-enhanced N-demethylation under resonant condition in the presence of oxygen molecule suggests the involvement the singlet oxygen in the photochemical transformation process.

It is well-known that singlet oxygen ($^1O_2$) reacts with organic molecules, resulting in oxidative transformation and degradation.[37, 68] Thermally or photon-induced generation of singlet oxygen is used to initiate oxidative N-dealkylation reactions.[69,70] Selective biocatalytic oxidative N-demethylation reactions are known to play a crucial role in nucleic acid regulation and synthesis.[71-74] More recently, highly selective biomimetic riboflavin-catalyzed oxidative demethylation of N-methyl adenine and related compounds using blue light has been reported by Xie and coauthors.[75] Photoexcited adsorbed molecular oxygen via hot electron transfer is proposed to initiate the oxidation of dyes and simple organic molecules such as formaldehyde, ethylene, and methanol under ambient conditions.[76] In this mechanism, hot electrons are injected into the antibonding molecular orbital of adsorbed O_2 to form electronically excited adsorbed O_2^-. The superoxide relaxes quickly to the ground electronic but vibrationally excited state of neutral O_2 by releasing electrons back into the metal. The activated neutral oxygen undergoes fast reaction to yield selective oxidation of organic molecules that are very close to the surface of the metal nanoparticles. Alternatively, adsorbed O_2 captures hot electron to form very reactive anionic oxygen that readily extracts protons from the organic molecules or water to generate more reactive free radical species to initiate the oxidation reaction.[69, 70]

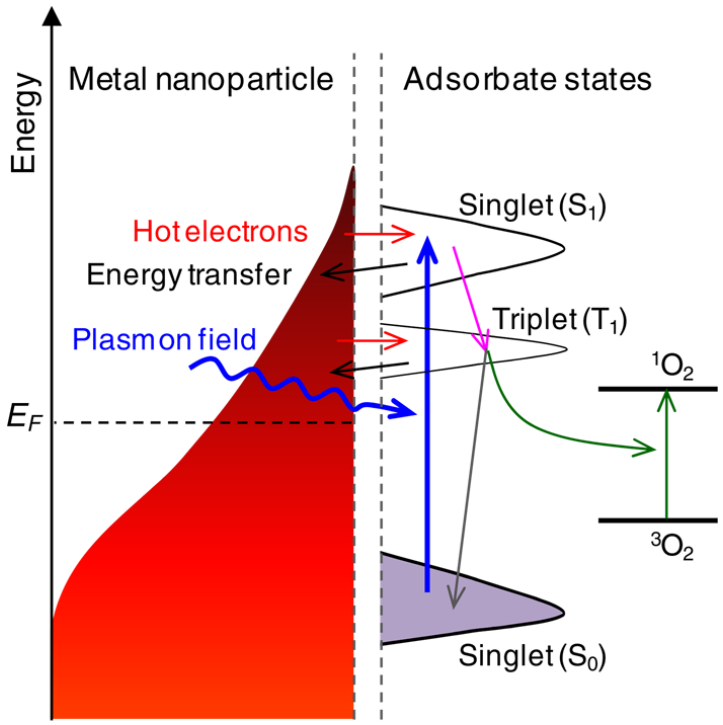

Figure 4.12 Schematic showing possible photophysical processes for MB on gold nanoparticles when the excitation energy is in resonance with the particle plasmon resonance and MB adsorbate electronic transition. The plasmon near field of the particle pumps the $S_0 \rightarrow S_1$ electronic transition of the MB adsorbate (blue lines). S_1 to T_1 intersystem crossing (purple arrow) can populate the MB T_1 state, from which energy transfer (green arrows) can promote oxygen from its triplet ground state ($^3O_2$) to singlet excited state ($^1O_2$). The black arrows indicate energy transfer to the metal surface, and red arrows indicate hot electron transfer to the unoccupied adsorbate states.

Recent experimental observations indicate that plasmonic nanoparticles enhance the efficiency of photosensitizers to generate singlet oxygen.[35, 77, 78] Considering that MB is a well-known photosensitizer,[79] the photochemical N-demethylation is likely to involve singlet oxygen. In fact, it has been shown that singlet oxygen drives N-demethylation of different organic molecules.[38, 54, 55, 80]

Scheme 2 Proposed Reaction Pathway of PEND-MB

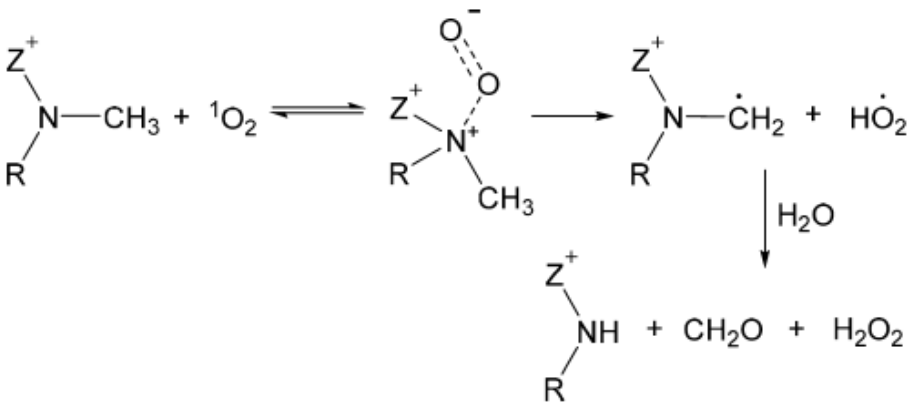

The interaction of MB with visible light can induce electronic transition from the singlet ground state (S_0) to the singlet excited state (S_1) that can be followed by intersystem crossing to the excited triplet state (T_1) as illustrated in **Figure 4.12**. The energy transfer from MB (T_1) to oxygen in its triplet ground state ($^3O_2$) can generate the reactive singlet oxygen ($^1O_2$). That is, the plasmon field drives the photochemical N-demethylation by pumping the $S_0 \rightarrow S_1$ electronic excitation of the MB adsorbate that leads to enhanced generation of $^1O_2$.

Singlet oxygen can interact with MB to form a charge-transfer complex (exciplex).[81, 82] Similar to the solution-phase mechanism,[55] H-atom transfer within the complex can lead to formation of a radical species, which in the presence of water results in N-demethylation as shown in **Scheme 2**,[61] in which only one of the methyl groups is shown for brevity, where Z^+ represents the rest of the cationic structural constituents of MB including the fused ring system and the two methyl groups attached to the N-atom on the other end of the molecule.

The discussion so far, particularly the dependence on excitation wavelength (**see chapter 3**), strongly supports that photochemical conversion of MB to thionine on gold nanoparticles is initiated by plasmon-pumped electronic excitation of the adsorbate. However, based on these observations, we cannot rule out the involvement of hot electron transfer in the reaction. Signatures of light-induced surface molecule interaction and partial charge transfer processes can be revealed by analyzing the frequencies of the vibrational modes that may be sensitive to charge redistribution in the surface-molecule complex. In the oxygen atmosphere, the frequency shift due to surface-molecule interaction and charge transfer can be overwhelmed by chemical transformation. However, the charging effect can be discovered in N_2 atmosphere, in which the photochemical reaction is suppressed.

In N_2 atmosphere, the 1392 cm^{-1} and 1620 cm^{-1} vibration modes shift in opposite direction, indicating the importance of light-induced surface-molecule interaction and charge-transfer effects. The surface-molecule interaction may cause delocalization of the π-electron density of the fused aromatic ring. This charge delocalization can strengthen the 1392 cm^{-1} vibration mode, which is due to the stretching vibration of the C−N attached to the methyl groups coupled to the stretching vibration of the fused aromatic ring. In contrast, the 1620 cm^{-1} ring vibration mode can be slightly weakened as the electron density is spread more over the entire aromatic system.[83]

We note that the blue shifting of the 1392 cm^{-1} vibration frequency in inert atmosphere (**Figure 4.8**f) is in contrast to the red shifting in the reactive atmospheres (**Figure 4.8**(d and e)), which suggests that the charge transfer and the N-demethylation reaction shift the vibration frequency in opposite direction. On the other hand, from the shifting of the vibrational frequency that initially appears at 1435 cm^{-1}, it is clear that the photochemical

N-demethylation is not completely absent. These observations suggest that if the photochemical transformation could be suppressed completely, the shifts induced by the surface-molecule interaction and charge transfer for the bands that initially peak at 1392 and 1620 cm^{-1} might be more significant than observed in this study. More comprehensive understanding into the charge transfer effect may be obtained by performing the SERS experiment at excitation wavelengths that do not induce photochemical transformation (see chapter 3). In fact, hot electron transfer to the unoccupied orbital of MB adsorbed on silver nanocubes has been proposed based on the unusually large anti-Stokes to Stokes Raman intensity ratio at 785 nm excitation wavelength at which no N-demethylation has been observed.[48, 49]

Charge transfer to MB adsorbate and local heating due to dissipation of energy from the resonant excitation of the molecule and particle resonances may assist the photochemical reactions by activating the surface−molecule complex to readily undergo chemical transformation. In addition, the hot electron can assist the reaction by activating molecular oxygen.[8, 41, 84] The formation of singlet oxygen and hot electron transfer can take place in concert. Considering the involvement of water in the reaction, it may be appropriate to think in terms of solvated hot electron, where a metastable $[MB(O_2)x.(H_2O)_n]^-$ cluster anion is adsorbed on the gold surface. This charge transfer process can modify the mechanism in **Scheme 2** according to the pathways proposed for photochemical N-demethylation of rufloxacin.[80] It is also important to note that the photochemical transformation of MB to thionine involves multistep reactions to replace four methyl groups with hydrogen. Calculated adsorption geometries of MB and its N-demethylated derivatives on Au(111) show that the molecules orient parallel to the surface with the separation between the center

of mass of the molecules and the surface decreasing from 3.31 Å (MB) to 3.24 Å (thionine) upon N-demethylation.[52]

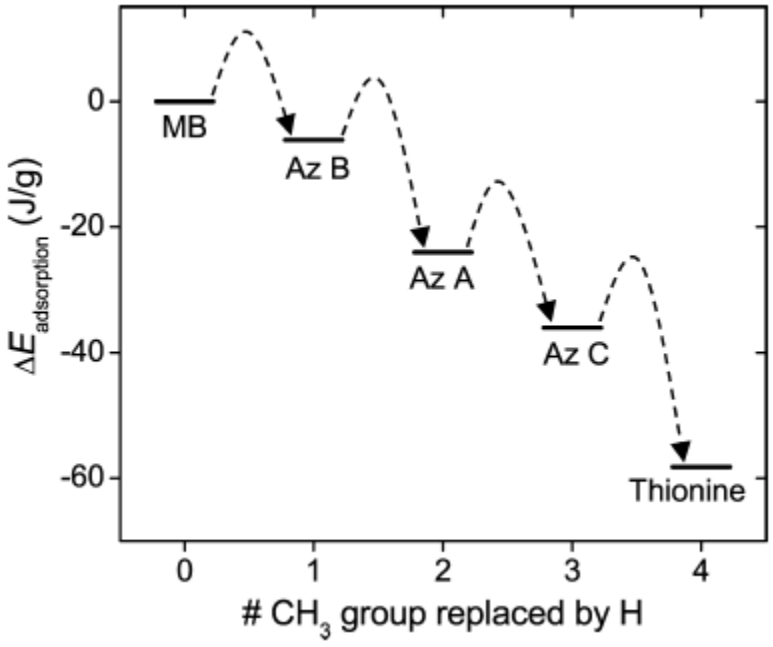

Figure 4.13 Relative adsorption energy per gram for methylene blue (MB), azure B (AZB), azure A (AZA), azure C (AZC), and thionine based on the theoretical results in ref 52.

In addition, the calculated adsorption energies indicate that N-demethylation of MB adsorbate is thermodynamically feasible. That is, every replacement of CH_3 group with H atom results in more favorable surface-molecule interaction, leading to a cascade of photochemical reactions until all of the methyl groups are replaced by hydrogen atoms, as depicted in **Figure 4.13**, which is based on the results of the theoretical calculations of Zhou et al.[52] Therefore, confirming whether the excited-state processes are important at each step requires future systematic experimental studies.

4.8 Conclusion

The mechanisms of a plasmon-enhanced photochemical reaction, N-demethylation of methylene blue, are investigated under different atmospheric and adsorption conditions

using SERS as operando spectroscopy. We found that in the presence of oxygen in the atmosphere and water molecules as adsorbates, MB undergoes photochemical N-demethylation to produce thionine and other intermediate species that have distinct vibrational signatures. The mechanism of the reaction appears to involve singlet oxygen generated via energy transfer from MB excited state to oxygen molecule. The localized plasmon field enhances the generation of singlet oxygen by pumping the electronic transition of methylene blue. Singlet oxygen can react with MB to form an exciplex that can transform MB to thionine and partial N-demethylation products in the presence of water. Unlike random degradation of organic molecules on traditional semiconductor catalysts, the photochemical reaction observed in this work is selective to N-demethylation of MB indicating that electronic excitations of adsorbates pumped by localized surface plasmon field can lead to selective reaction pathways.

4.9 Reference

1. Zhang, Y. et al. Surface-Plasmon-Driven Hot Electron Photochemistry. *Chem. Rev.* **118**, 2927 (2018).

2. Zrimsek, A.B. et al. Single-Molecule Chemistry with Surface- and Tip-Enhanced Raman Spectroscopy. *Chem. Rev.* **117**, 7583 (2017).

3. Bjerneld, E.J., Svedberg, F., Johansson, P. & Kall, M. Direct Observation of Heterogeneous Photochemistry on Aggregated Ag Nanocrystals Using Raman Spectroscopy: The Case of Photoinduced Degradation of Aromatic Amino Acids. *J. Phys. Chem. A* **108**, 4187 (2004).

4. Choi, H.K. et al. Metal-Catalyzed Chemical Reaction of Single Molecules Directly Probed by Vibrational Spectroscopy. *J. Am. Chem. Soc.* **138**, 4673 (2016).

5. Harvey, C.E. & Weckhuysen, B.M. Surface- and Tip-Enhanced Raman Spectroscopy as Operando Probes for Monitoring and Understanding Heterogeneous Catalysis. *Catal. Lett.* **145**, 40 (2015).

6. Joseph, V. et al. Characterizing the Kinetics of Nanoparticle-Catalyzed Reactions by Surface-Enhanced Raman Scattering. *Angew. Chem., Int. Ed.* **51**, 7592 (2012).

7. Cao, E. et al. Electrooptical Synergy on Plasmon-Exciton-Codriven Surface Reduction Reactions. *Adv. Mater. Interfaces* **4**, 1700869 (2017).

8. Christopher, P., Xin, H.L. & Linic, S. Visible-Light-Enhanced Catalytic Oxidation Reactions on Plasmonic Silver Nanostructures. *Nat. Chem.* **3**, 467 (2011).

9. Christopher, P., Xin, H.L., Marimuthu, A. & Linic, S. Singular Characteristics and Unique Chemical Bond Activation Mechanisms of Photocatalytic Reactions on Plasmonic Nanostructures. *Nat. Mater.* **11**, 1044 (2012).

10. Goncher, G.M., Parsons, C.A. & Harris, C.B. Photochemistry on Rough Metal-Surfaces. *J. Phys. Chem.* **88**, 4200 (1984).

11. Huang, Y.F. et al. When the Signal Is Not from the Original Molecule to Be Detected: Chemical Transformation of Para-Aminothiophenol on Ag During the SERS Measurement. *J. Am. Chem. Soc.* **132**, 9244 (2010).

12. Jeong, D.H., Jang, N.H., Suh, J.S. & Moskovits, M. Photodecomposition of Diazanaphthalenes Adsorbed on Silver Colloid Surfaces. *J. Phys. Chem. B* **104**, 3594 (2000).

13. Kazuma, E., Jung, J., Ueba, H., Trenary, M. & Kim, Y. Real-Space and Real-Time Observation of a Plasmon-Induced Chemical Reaction of a Single Molecule. *Science* **360**, 521 (2018).

14. Mukherjee, S. et al. Hot Electrons Do the Impossible: Plasmon-Induced Dissociation of H2 on Au. *Nano Lett.* **13**, 240 (2013).

15. Redmond, P.L., Wu, X.M. & Brus, L. Photovoltage and Photocatalyzed Growth in Citrate-Stabilized Colloidal Silver Nanocrystals. *J. Phys. Chem. C* **111**, 8942 (2007).

16. Tesema, T.E., Kafle, B., Tadesse, M.G. & Habteyes, T.G. Plasmon-Enhanced Resonant Excitation and Demethylation of Methylene Blue. *J. Phys. Chem. C* **121**, 7421 (2017).

17. Yu, S.J., Wilson, A.J., Heo, J. & Jain, P.K. Plasmonic Control of Multi-Electron Transfer and C-C Coupling in Visible-Light-Driven CO2 Reduction on Au Nanoparticles. *Nano Lett.* **18**, 2189 (2018).

18. Zhang, Y. et al. Direct Photocatalytic Conversion of Aldehydes to Esters Using Supported Gold Nanoparticles under Visible Light Irradiation at Room Temperature. *J. Phys. Chem. C* **118**, 19062 (2014).

19. Zhao, J. et al. A Comparison of Photocatalytic Activities of Gold Nanoparticles Following Plasmonic and Interband Excitation and a Strategy for Harnessing Interband Hot Carriers for Solution Phase Photocatalysis. *ACS Cent. Sci.* **3**, 482 (2017).

20. Hartland, G.V., Besteiro, L.V., Johns, P. & Govorov, A.O. What's So Hot About Electrons in Metal Nanoparticles? *ACS Energy Lett.* **2**, 1641 (2017).

21. Brus, L. Noble Metal Nanocrystals: Plasmon Electron Transfer Photochemistry and Single-Molecule Raman Spectroscopy. *Acc. Chem. Res.* **41**, 1742 (2008).

22. Linic, S., Aslam, U., Boerigter, C. & Morabito, M. Photochemical Transformations on Plasmonic Metal Nanoparticles. *Nat. Mater.* **14**, 567 (2015).

23. Carattino, A., Caldarola, M. & Orrit, M. Gold Nanoparticles as Absolute Nanothermometers. *Nano Lett.* **18**, 874 (2018).

24. Keller, E.L. & Frontiera, R.R. Ultrafast Nanoscale Raman Thermometry Proves Heating Is Not a Primary Mechanism for Plasmon-Driven Photocatalysis. *ACS Nano* **12**, 5848 (2018).

25. Nguyen, S.C. et al. Study of Heat Transfer Dynamics from Gold Nanorods to the Environment Via Time-Resolved Infrared Spectroscopy. *ACS Nano* **10**, 2144 (2016).

26. Pozzi, E.A. et al. Evaluating Single-Molecule Stokes and Anti-Stokes SERS for Nanoscale Thermometry. *J. Phys. Chem. C* **119**, 21116 (2015).

27. Adleman, J.R., Boyd, D.A., Goodwin, D.G. & Psaltis, D. Heterogenous Catalysis Mediated by Plasmon Heating. *Nano Lett.* **9**, 4417 (2009).

28. Golubev, A.A., Khlebtsov, B.N., Rodriguez, R.D., Chen, Y. & Zahn, D.R.T. Plasmonic Heating Plays a Dominant Role in the Plasmon-Induced Photocatalytic Reduction of 4-Nitrobenzenethiol. *J. Phys. Chem. C* **122**, 5657 (2018).

29. Zhang, X. et al. Plasmon-Enhanced Catalysis: Distinguishing Thermal and Nonthermal Effects. *Nano Lett.* **18**, 1714 (2018).

30. Kafle, B., Poveda, M. & Habteyes, T.G. Surface Ligand-Mediated Plasmon-Driven Photochemical Reactions. *J. Phys. Chem. Lett.* **8**, 890 (2017).

31. Nitzan, A. & Brus, L.E. Theoretical-Model for Enhanced Photochemistry on Rough Surfaces. *J. Chem. Phys.* **75**, 2205 (1981).

32. Wolkow, R.A. & Moskovits, M. Enhanced Photochemistry on Silver Surfaces. *J. Chem. Phys.* **87**, 5858 (1987).

33. Zhang, Y., Aslan, K., Previte, M.J.R. & Geddes, C.D. Metal-Enhanced Singlet Oxygen Generation: A Consequence of Plasmon Enhanced Triplet Yields. *J. Fluoresc.* **17**, 345 (2007).

34. Zhang, Y., Aslan, K., Previte, M.J.R. & Geddes, C.D. Plasmonic Engineering of Singlet Oxygen Generation. *Proc. Natl. Acad. Sci. U.S.A.* **105**, 1798 (2008).

35. Planas, O., Macia, N., Agut, M., Nonell, S. & Heyne, B. Distance-Dependent Plasmon-Enhanced Singlet Oxygen Production and Emission for Bacterial Inactivation. *J. Am. Chem. Soc.* **138**, 2762 (2016).

36. Lv, J.L., Wu, G.Q., He, Y., Zhang, L.J. & Yi, Y.H. Methylene Blue-Loaded Gold Nanobipyramids@SiO2 Enhanced Singlet Oxygen Generation for Phototherapy of Cancer Cells. *Opt. Mater. Express* **7**, 409 (2017).

37. Li, H.R., Wu, L.Z. & Tung, C.H. Reactions of Singlet Oxygen with Olefins and Sterically Hindered Amine in Mixed Surfactant Vesicles. *J. Am. Chem. Soc.* **122**, 2446 (2000).

38. Baciocchi, E., Del Giacco, T., Lanzalunga, O. & Lapi, A. Singlet Oxygen Promoted Carbon-Heteroatom Bond Cleavage in Dibenzyl Sulfides and Tertiary Dibenzylamines. Structural Effects and the Role of Exciplexes. *J. Org. Chem.* **72**, 9582 (2007).

39. Ho-Wu, R., Yau, S.H. & Goodson, T. Efficient Singlet Oxygen Generation in Metal Nanoclusters for Two-Photon Photodynamic Therapy Applications. *J. Phys. Chem. B* **121**, 10073 (2017).

40. Vankayala, R., Sagadevan, A., Vijayaraghavan, P., Kuo, C.L. & Hwang, K.C. Metal Nanoparticles Sensitize the Formation of Singlet Oxygen. *Angew. Chem., Int. Ed.* **50**, 10640 (2011).

41. Huang, Y.F. et al. Activation of Oxygen on Gold and Silver Nanoparticles Assisted by Surface Plasmon Resonances. *Angew. Chem., Int. Ed.* **53**, 2353 (2014).

42. Kim, M., Lin, M., Son, J., Xu, H.X. & Nam, J.M. Hot-Electron-Mediated Photochemical Reactions: Principles, Recent Advances, and Challenges. *Adv. Opt. Mater.* **5**, 1700004 (2017).

43. Zhang, Z.L., Xu, P., Yang, X.Z., Liang, W.J. & Sun, M.T. Surface Plasmon-Driven Photocatalysis in Ambient, Aqueous and High-Vacuum Monitored by SERS and TERS. *J. Photochem. Photobiol., C* **27**, 100 (2016).

44. Lombardi, J.R., Birke, R.L., Lu, T.H. & Xu, J. Charge-Transfer Theory of Surface Enhanced Raman-Spectroscopy - Herzberg-Teller Contributions. *J. Chem. Phys.* **84**, 4174 (1986).

45. Morton, S.M. & Jensen, L. Understanding the Molecule-Surface Chemical Coupling in SERS. *J. Am. Chem. Soc.* **131**, 4090 (2009).

46. Valley, N., Greeneltch, N., Van Duyne, R.P. & Schatz, G.C. A Look at the Origin and Magnitude of the Chemical Contribution to the Enhancement Mechanism of Surface-Enhanced Raman Spectroscopy (SERS): Theory and Experiment. *J. Phys. Chem. Lett.* **4**, 2599 (2013).

47. Birke, R.L., Lombardi, J.R., Saidi, W.A. & Norman, P. Surface-Enhanced Raman Scattering Due to Charge-Transfer Resonances: A Time-Dependent Density Functional Theory Study of Ag13-4-Mercaptopyridine. *J. Phys. Chem. C* **120**, 20721 (2016).

48. Boerigter, C., Aslam, U. & Linic, S. Mechanism of Charge Transfer from Plasmonic Nanostructures to Chemically Attached Materials. *ACS Nano* **10**, 6108 (2016).

49. Boerigter, C., Campana, R., Morabito, M. & Linic, S. Evidence and Implications of Direct Charge Excitation as the Dominant Mechanism in Plasmon-Mediated Photocatalysis. *Nat. Commun.* **7**, 10545 (2016).

50. Anderson, S. Orientation of Methylene Blue Molecules Adsorbed on Solids. *J. Opt. Soc. Am.* **39**, 49 (1949).

51. Greathouse, J.A. et al. Methylene Blue Adsorption on the Basal Surfaces of Kaolinite: Structure and Thermodynamics from Quantum and Classical Molecular Simulation. *Clay Clay Miner.* **63**, 185 (2015).

52. Zhou, L., Johnson, R., Habteyes, T. & Guo, H. Adsorption of Methylene Blue and Its N-Demethylated Derivatives on the (111) Face of Coinage Metals: The Importance of Dispersion Interactions. *J. Chem. Phys.* **146**, 164701 (2017).

53. Hutchinson, K., Hester, R.E., Albery, W.J. & Hillman, A.R. Raman-Spectroscopic Studies of a Thionine-Modified Electrode. *J. Chem. Soc., Faraday Trans. 1* **80**, 2053 (1984).

54. Baciocchi, E., Del Giacco, T. & Lapi, A. Oxygenation of Benzyldimethylamine by Singlet Oxygen. Products and Mechanism. *Org. Lett.* **6**, 4791 (2004).

55. Baciocchi, E., Del Giacco, T. & Lapi, A. Quenching of Singlet Oxygen by Tertiary Aliphatic Amines. Structural Effects on Rates and Products. *Helv. Chim. Acta* **89**, 2273 (2006).

56. Craighead, H.G. & Glass, A.M. Optical-Absorption of Small Metal Particles with Adsorbed Dye Coats. *Optics Letters* **6**, 248 (1981).

57. Darby, B.L., Auguie, B., Meyer, M., Pantoja, A.E. & Le Ru, E.C. Modified Optical Absorption of Molecules on Metallic Nanoparticles at Sub-Monolayer Coverage. *Nat. Photonics* **10**, 40 (2016).

58. Hildebrandt, P. & Stockburger, M. Surface-Enhanced Resonance Raman-Spectroscopy of Rhodamine-6g Adsorbed on Colloidal Silver. *J. Phys. Chem.* **88**, 5935 (1984).

59. Tognalli, N.G., Fainstein, A., Vericat, C., Vela, M.E. & Salvarezza, R.C. Exploring Three-Dimensional Nanosystems with Raman Spectroscopy: Methylene Blue

Adsorbed on Thiol and Sulfur Monolayers on Gold. *J. Phys. Chem. B* **110**, 354 (2006).

60. Lombardi, J.R. & Birke, R.L. A Unified Approach to Surface-Enhanced Raman Spectroscopy. *J. Phys. Chem. C* **112**, 5605 (2008).

61. Tesema, T.E., Annesley, C. & Habteyes, T.G. Plasmon-Enhanced Autocatalytic N-Demethylation. *J. Phys. Chem. C* **122**, 19831 (2018).

62. Habteyes, T.G., Dhuey, S., Kiesow, K.I. & Vold, A. Probe-Sample Optical Interaction: Size and Wavelength Dependence in Localized Plasmon Near-Field Imaging. *Optics Express* **21**, 21607 (2013).

63. Kafle, B., Tesema, T.E., Kazemi, A. & Habteyes, T.G. Stripping and Transforming Alloyed Semiconductor Quantum Dots via Atomic Interdiffusion. *J. Phys. Chem. C* **120**, 12850 (2016).

64. Tesema, T.E., Kafle, B. & Habteyes, T.G. Plasmon-Driven Reaction Mechanisms: Hot Electron Transfer versus Plasmon-Pumped Adsorbate Excitation. *The Journal of Physical Chemistry C* **123**, 8469-8483 (2019).

65. Dutta Roy, S.D., Ghosh, M. & Chowdhury, J. Adsorptive Parameters and Influence of Hot Geometries on the SER(R)S Spectra of Methylene Blue Molecules Adsorbed on Gold Nanocolloidal Particles. *J. Raman Spectrosc.* **46**, 451 (2015).

66. Roy, S.D., Ghosh, M. & Chowdhury, J. Adsorptive Parameters and Influence of Hot Geometries on the SER(R)S Spectra of Methylene Blue Molecules Adsorbed on Gold Nanocolloidal Particles. *J. Raman Spectrosc.* **46**, 451 (2015).

67. Li, Y. et al. Interplay of Bias-Driven Charging and the Vibrational Stark Effect in Molecular Junctions. *Nano Lett.* **16**, 1104 (2016).

68. Bernstein, R. & Foote, C.S. Singlet Oxygen Involvement in the Photochemical Reaction of C-60 and Amines. Synthesis of an Alkyne-Containing Fullerene. *J. Phys. Chem. A* **103**, 7244 (1999).

69. Zhu, H. et al. Mechanism of Supported Gold Nanoparticles as Photocatalysts under Ultraviolet and Visible Light Irradiation. *Chem. Commun.*, 7524 (2009).

70. Brus, L. Growing Gold Nanoprisms with Light. *Nat. Mater.* **15**, 824 (2016).

71. Fu, Y. et al. Fto-Mediated Formation of N6-Hydroxymethyladenosine and N6-Formyladenosine in Mammalian Rna. *Nat. Commun.* **4**, 1798 (2013).

72. Pan, T. N6-Methyl-Adenosine Modification in Messenger and Long Non-Coding Rna. *Trends Biochem. Sci.* **38**, 204 (2013).

73. Zheng, G. et al. Alkbh5 Is a Mammalian Rna Demethylase That Impacts Rna Metabolism and Mouse Fertility. *Mol. Cell* **49**, 18 (2013).

74. Ye, F. et al. Repair of Methyl Lesions in RNA by Oxidative Demethylation. *MedChemComm* **5**, 1797 (2014).

75. Xie, L.J., Wang, R.L., Wang, D., Liu, L. & Cheng, L. Visible-Light-Mediated Oxidative Demethylation of N6-Methyl Adenines. *Chem. Commun.* **53**, 10734 (2017).

76. Shaik, F., Peer, I., Jain, P.K. & Amirav, L. Plasmon-Enhanced Multicarrier Photocatalysis. *Nano Lett.* **18**, 4370 (2018).

77. Zhang, Y., Aslan, K., Previte, M.J.R. & Geddes, C.D. Plasmonic Engineering of Singlet Oxygen Generation. *Proc. Natl. Acad. Sci. U. S. A.* **105**, 1798 (2008).

78. Lv, J.L., Wu, G.Q., He, Y., Zhang, L.J. & Yi, Y.H. Methylene Blue-Loaded Gold Nanobipyramids @SiO2 Enhanced Singlet Oxygen Generation for Phototherapy of Cancer Cells. *Opt. Mater. Express* **7**, 409 (2017).

79. Tardivo, J.P. et al. Methylene Blue in Photodynamic Therapy: From Basic Mechanisms to Clinical Applications. *Photodiagn. Photodyn. Ther.* **2**, 175 (2005).

80. Belvedere, A., Bosca, F., Cuquerella, M.C., de Guidi, G. & Miranda, M.A. Photoinduced N-Demethylation of Rufloxacin and Its Methyl Ester Under Aerobic Conditions. *Photochem. Photobiol.* **76**, 252 (2002).

81. Gorman, A.A., Gould, I.R., Hamblett, I. & Standen, M.C. Reversible Exciplex Formation Between Singlet Oxygen, 1-Delta-G, and Vitamin-E - Solvent and Temperature Effects. *J. Am. Chem. Soc.* **106**, 6956 (1984).

82. Gould, I.R., Young, R.H., Mueller, L.J. & Farid, S. Mechanisms of Exciplex Formation - Roles of Superexchange, Solvent Polarity, and Driving-Force for Electron-Transfer. *J. Am. Chem. Soc.* **116**, 8176 (1994).

83. Phan, H.T. & Haes, A.J. Impacts of Ph and Intermolecular Interactions on Surface-Enhanced Raman Scattering Chemical Enhancements. *J. Phys. Chem. C* **122**, 14846 (2018).

84. Xu, P. et al. Mechanistic Understanding of Surface Plasmon Assisted Catalysis on a Single Particle: Cyclic Redox of 4-Aminothiophenol. *Sci. Rep.* **3**, 2997 (2013).

Chapter Five

5 Extracting transition band of adsorbate from molecule-plasmon coupling

5.1 Abstract

The coupling between molecular electronic and plasmon excitations can result in various intriguing outcomes depending on how strongly the excitations couple to compete with their respective decay rates. In the strong coupling regime, the excited states can hybridize resulting in spectral splitting, while modification of absorption and spontaneous emission rates is expected in the weak coupling regime. Here, we show that molecule-plasmon weak excitation coupling can be used for determining the electronic absorption band of resonant adsorbates with sensitivity down to sub-monolayer surface coverage. By comparing the absorbance of gold nanoisland (AuNI) with and without adsorbate of resonant molecules (methylene blue (MB) and thionine (TH)), induced transparency is observed at the absorption band of the adsorbates. Apart from significant spectral broadening and red shifting of peak wavelength, the inverted transparency spectrum has surprising similarity to the absorption spectrum of the corresponding dye in solution. Interestingly, the adsorption isotherm determined based on the integral area under the inverted transparency spectra is linearly correlated to the corresponding isotherm determined based on adsorbate induced plasmon resonance red shift. The results presented in this work demonstrate a simple, sensitive and reliable approach for determining adsorbate absorption spectrum from molecule-plasmon excitation coupling.

5.2 Introduction

Characteristic optical properties of a hybrid material can obtained be obtained with efficient coupling of light induced molecular dipoles with different surface plasmon modes [1-9] that can be exploited for applications in optical[10], chemical, and biological sensors as well as photonic-device.[11, 12] It has been reported more than two decades ago, an energy gap for the surface plasmon polaritons (SPP) propagating in metallic grating can modify the emission properties of a dye adsorbed on the surface of the metal grating.[13, 14] The excited dye molecules on metallic grating can relax non-radiatively by generating surface plasmons.[15] Non-intuitive transmission properties have been observed when an array of periodic and disordered group of nanoholes in a gold or silver metal film is coated with physiosorbed dense layer of strongly absorbing dye. This is the occurrence of strong transmission peak at a wavelength at which the dye molecule absorbs strongly, a phenomenon called absorption-Induced transparency (AIT). J. Dintinger *et al.* and S. M. Williams *et al.* were demonstrated that a molecular monolayer coverage on an array of holes is sufficient to induce strong enhancement in electronic[16] and vibrational[17] absorption spectra of adsorbates.

On the other hand, metal nanoparticles are capable of enhancing the absorption coefficient of dyes adsorbed on their surfaces and contribute in a wide area of applications.[18] Strong coupling between the dye and metal particle depends on the degree of spectral overlap of the dye absorption and surface plasmon resonance (SPR) of the particles.[19, 20] However, most studies to date are devoted to strong dye-plasmon coupling interaction that can be maximized by increasing the molecular layer, usually high surface coverage or aggregates.[21-27] There is only one report that claims the observation of strong coupling for

less than ten methylene blue (MB) molecules at room temperature.[28] In this experiment, spectral splitting has been observed only when the molecules of MB are aligned vertically along the electric field in particle-film plasmonic system that provides extremely small cavity volume. No spectral splitting has been observed when the MB molecules adsorb to the gold surface randomly.

For aggregates of dye adsorbed on metal particles, the observed optical properties are an average effect of dye-dye and dye-plasmon interactions and the effect of isolate molecule on the optical properties of the hybrid system is difficult to distinguish. To solve this problem, Brendan *et al*[29] used very dilute solution (10 nM) of common chromophores such as Rhodamine 700, Rhodamine 6G, Nile blue, and Crystal Violet to determine the surface absorbance of an isolated molecule at negligible dye-dye and dye-plasmon resonance interactions. However, their investigations were mainly in the context of spectral changes associated with the adsorption of an isolated molecule on the surface of metal nanoparticles with the absorption band detuned by ~200 nm from the SPR of the nanoparticles. Similarly, the optical responses of nanoparticle-dye interaction at very low concentration of Rhodamine 6G molecule have be thoroughly investigated by tuning the plasmon resonance of silver nanosphere lithography with respect to the dye resonance.[30]. But this may method lacks surface specificity due to interferences from non-adsorbate molecules in a solution.

The strong and weak coupling regimes may be quantified in terms of the coupling constant (β), which is based on atom-field interaction that is estimated as[31]

$$\beta = \frac{\mu}{\hbar}\sqrt{\frac{\hbar\omega_0}{2\varepsilon_0 V}} \qquad Eq\ 1$$

where $\hbar$ is the reduced Planck's constant, ε_0 the vacuum permittivity constant, ω_0 transition frequency of the molecule, μ the dipole matrix element and V the effective cavity volume. For realizing the strong coupling regime, β must be large enough to overcome the cavity loss rate as well as dye scattering rate that is proportional to temperature.

In general, for □-conjugated molecules like MB, the molecules orient parallel to the surface resulting in weak coupling with the surface plasmon. In this case, the interaction may be explained based on dipole-surface interaction that may result in plasmon coupled photon emission and quenching depending on the competition among different channels. For molecules, directly adsorbed on metal surface, direct emission by the molecule is unlikely as the energy transfer to the surface dominates.[32] However, important insight into the molecule-plasmon excitation coupling can be obtained through careful analysis of the plasmon resonance spectral properties. This analysis may allow determining adsorbate properties that otherwise are difficult or impossible to quantify.

In this study, we show that molecule-plasmon excitation coupling can be used for determining the electronic absorption band of adsorbates on metal surfaces. The electronic transition energy of adsorbates is critical for understanding surface chemical, electronic and optical properties. For example, determining the spectral overlap between excitation wavelength with the molecular electronic and particle plasmon resonances should be the first step in explaining the mechanisms of surface-enhanced fluorescence,[33, 34] surface-enhanced Raman scattering,[35-37] and plasmon driven photochemistry.[38-41]

The hypothesis of determining adsorbate absorption band from molecule-plasmon excitation coupling is tested by comparing the absorption band of plasmonic gold

nanoisland (AuNI) before and after adsorption of MB and TH molecules that have well known electronic absorption band in the visible spectral region. The results indicate reduced absorbance (increased transmission) of the plasmon resonance in the spectral regions that overlap with the respective absorption band of the adsorbates. The absorption band of the adsorbate is extracted from the absorption spectrum of the plasmon resonance through systematic experimental and data analysis procedures.

5.3 Result and Discussion

The schematic in **Figure 5.1**a shows the principle of the experiment for extracting the perturbation $\delta(M)$ on the optical transmission of the plasmonic system induced by the coupling of the molecular electronic excitation. The molecules represented by the green dots are adsorbed on the gold nanostructures (**Figure 5.1**b) that are supported on quartz glass. The incident light with intensity I_0 excites both the electronic transition of the molecule (M → M* transition) as well as the plasmon resonance of the gold nanostructures (AuNIs). The plasmon near-field concentrated around the AuNIs (**Figure 5.1**c) enhances the rate of the molecular excitation, and the excitation energy of the molecule couples back to the surface plasmon, modifying the intensity of the transmitted light. Modification in the intensity of the transmitted light can be denoted by $I(\lambda) + \delta(M)$, where $I(\lambda)$ is the intensity of the transmitted light assuming that the effect of the adsorbate is limited to wavelength (λ) shift of the plasmon resonance. Considering $\delta(M)$ is relevant only for resonant molecules, the absorbance of non-resonant adsorbate (A_N) can be expressed using the Beer-Lambert law as

$$A_N = -log\left(\frac{I(\lambda)}{I_0}\right) \qquad Eq\ 2$$

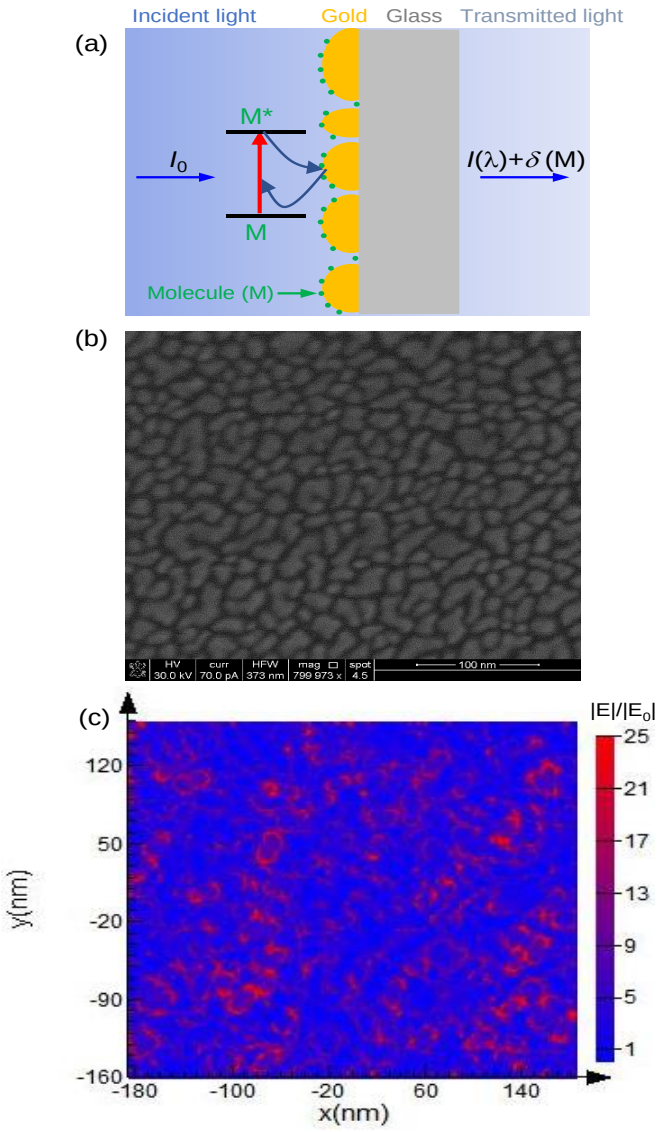

Figure 5.1 Schematic that shows the principle of the experiment. (b) Scanning electron microscope image of the gold nanoislands formed by electron-beam evaporation of gold on glass. (c) Calculated near-field distribution at □ = 680 nm.

Similarly, for resonant adsorbate that can induce similar plasmon resonance wavelength shift as the non-resonant one, the absorbance A_R can be written as

$$A_R = -log\left(\frac{I(\lambda)+\delta(M)}{I_0}\right) \qquad Eq\ 3$$

The change in the absorbance (ΔA) due to molecule-plasmon excitation coupling for a resonant adsorbate can then be calculated using the non-resonant adsorbate as a reference.

$$\Delta A = A_R - A_N = log\left(1 + \frac{\delta(M)}{I(\lambda)}\right) \quad Eq\ 4$$

In ***Eq* 4**, $\delta(M) < 0$ implies reduced absorbance ($\Delta A < 0$) due to the coupling of the molecular excitation energy to the surface plasmon mode that results in enhanced transmission at the absorption wavelength of the adsorbate. It is important to note that $\delta(M)$ is extremely small compared to the extinction cross-section of the plasmonic metal nanostructures. Consequently, determining the absorption band of the adsorbate based on ***Eq* 4** requires measuring the plasmon resonance of the same metal nanostructures before and after adsorption of the analyte molecule. The principle described above is implemented by depositing the gold nanoislands on one of the outer surfaces of quartz cuvettes so that the rigid mount of the absorption spectrophotometer (see method in **chapter 2** for sample fabrication, preparation and measurement details) is used to probe exactly the same plasmonic surfaces before and after adsorption of the analyte molecules. In **Figure 5.2**a, the absorption spectra of the bare gold nanoislands (AuNI-1 and AuNI-2) of ~4.8 nm thickness determined from atomic force microscope image displayed in **Figure 5.3** are shown by the dotted black and red lines. The absorption spectra of the same AuNIs after adsorption of resonant MB and non-resonant 6-mercaptohexanoic acid (MHA) are shown by the solid black and red lines, respectively. The adsorption of both MB and MHA has resulted in significant and comparable red shifting of the respective plasmon resonances. More importantly, the adsorption of MB has induced an elbowing effect (small quenching dip) as can be seen comparing the solid red line (A_R) to the solid black line (A_N) (**Figure 5.2**a).

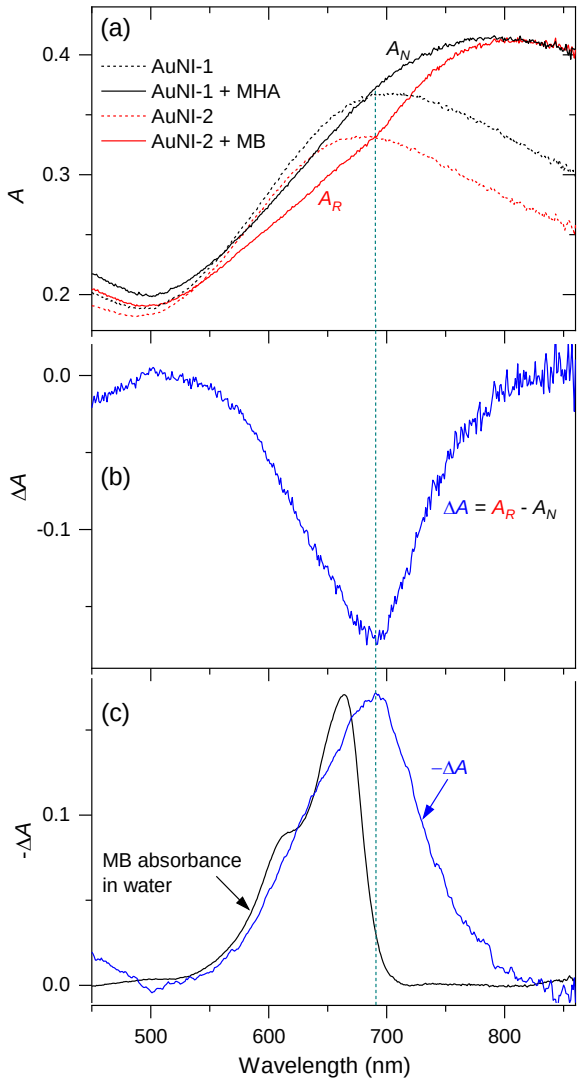

Figure 5.2 Experimental procedure for determining adsorbate induced transparency. (a) The dotted black (AuNI-1) and red lines (AuNI-2) are absorption spectra of two different bare plasmonic AuNIs. The solid lines (A_N) and (A_R) show the absorption spectra after the non-resonant MHA and resonant MB molecules are adsorbed on the AuNI-1 and AuNI-2, respectively. (b) Difference spectrum obtained by subtracting A_N from A_R. (c) The inverted difference spectrum (blue line) compared to the absorption spectrum of MB in water (black line).

The elbowing effect is attributed to enhanced transmission due to the coupling of the MB excitation energy to the plasmon resonance that results in the observation of reduced absorbance. The magnitude and shape of the absorbance reduction is obtained by

subtracting A_N from A_R (according to ***Eq* 4)** after normalizing the two curves such that they have the same minima and maxima, and the result (ΔA) is plotted in **Figure 5.2**b.

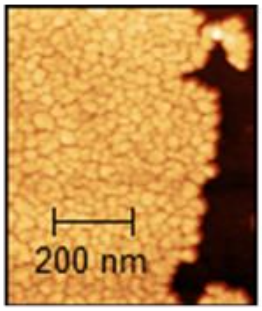

Figure 5.3 Representative AFM image of the AuNI

Clearly, a window of transparency that appears to match the absorption band of the MB adsorbate is observed. The inverted spectrum ($-\Delta A$) has reasonable similarity to the absorption spectrum of MB in water as shown in **Figure 5.2**c. With respect to the solution phase absorption band, the inverted spectrum is broad and is shifted to the red by about 24 nm, which is in agreement with the results obtained using integrating sphere absorption spectroscopy of Rhodamine 700 adsorbed on silver nanoparticles.[42] We note that enhanced transmission at the absorption band of over 30 nm thick cyanine J-aggregates has been observed when the aggregates are supported on arrays of 200 nm thick gold and silver nanoholes (100 nm diameter),[32, 43] while our observation is for sub-monolayer of adsorbates as demonstrated next.

In all our experiments, the adsorption of the analyte molecules is carried out by immersing the AuNIs in solutions of 100 – 220 □M concentration for 1 – 2 hours. Next, we confirm that these solution processes produce sub-monolayer to monolayer surface coverage. For correlating the surface concentration to the induced transparency, the absorption measurement has been repeated on AuNIs after increasing the adsorption times

successively for a duration of 1 minute. The results presented in **Figure 5.4**a shows that as the adsorption time increases, the plasmonic absorbance at the absorption wavelength of the MB adsorbate decreases continuously. The effect of the adsorption time is more apparent in the difference spectra plotted in **Figure 5.4**b. Signature of the adsorbate absorption band that results from molecule-plasmon excitation coupling is observed at short adsorption time (one minute). The magnitude of the ΔA increases with increasing time as the number of MB adsorbates per unit area increases.

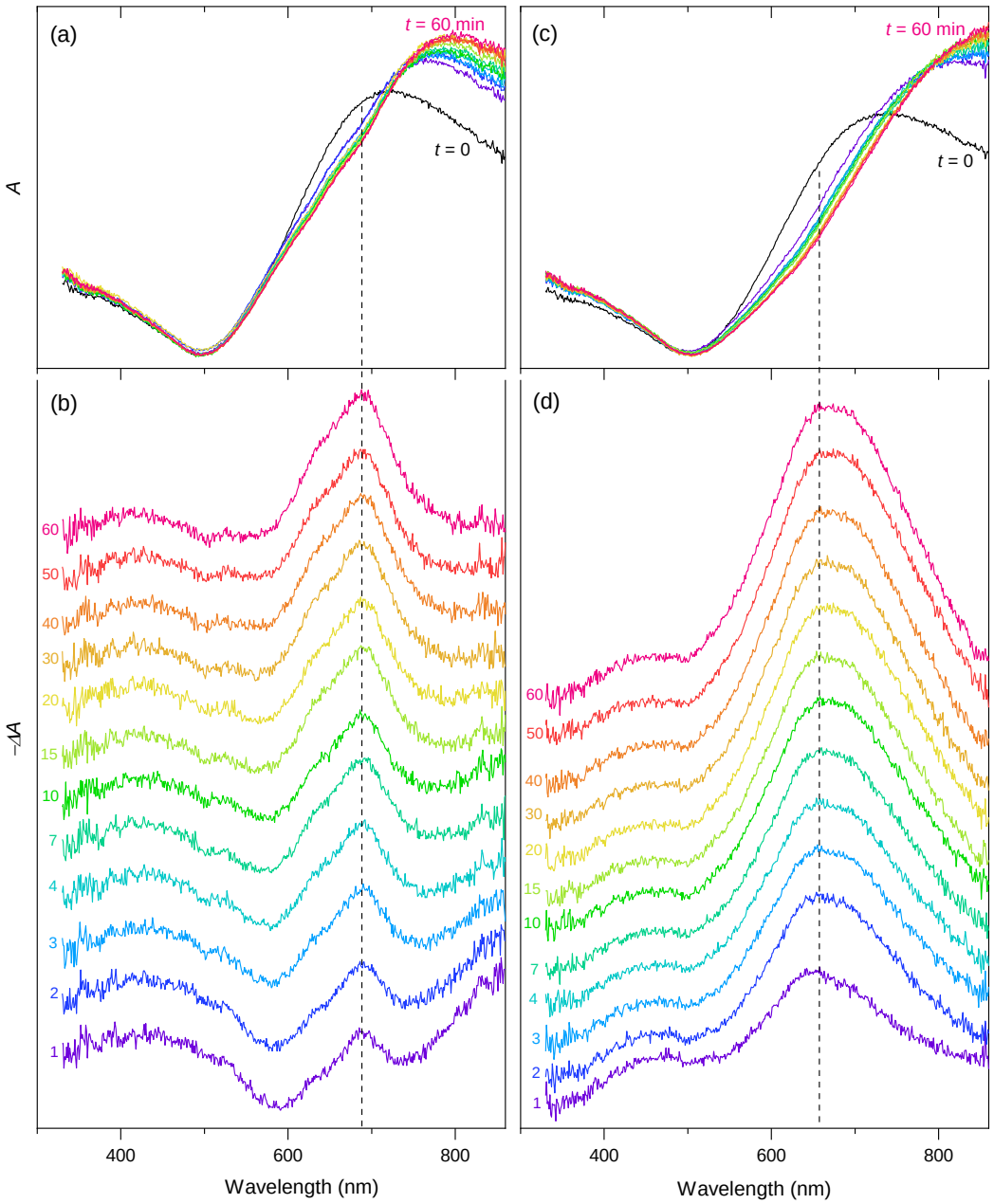

Figure 5.4 Spectral evolution depending on adsorption time. (a) The absorption spectra of the same AuNIs as the adsorption time of MB is increased from 0 (black line, bare gold) to 60 minutes (pink line). (b) Difference spectra obtained by subtracting the spectrum of AuNI-MHA from the AuNI-MB spectra at different adsorption time. The numbers next to each plot are the adsorption time in minutes. (c, d) Same as (a, b) for thionine as adsorbate.

Interestingly, the shoulder peak that is observed in the solution phase absorption spectrum

MB (see **Figure 5.2**c) appears to be reproduced in the series of spectra in **Figure 5.4**b. To

obtain insight into the adsorption properties depending on molecular structures, the results obtained for MB adsorbate (Figure 5.4a-b) are compared to that of thionine (**Figure 5.4**c-d). The peak position in the difference surface absorption spectra for thionine (**Figure 5.4**d) has shifted to the red by about 57 nm with respect to the absorption band of thionine in water that peak at 599 nm (see **chapter 2**), compared to the 24 nm red shift for MB. This large wavelength shift for thionine is accompanied by drastic linewidth broadening. The more pronounced wavelength shift and broadening for TH than for MB is attributed to the more favorable dye-surface interaction due to the absence of the four methyl groups at the N-terminal of MB (**chapter 2)**. Replacing bulkier methyl groups with hydrogen atoms upon converting MB to TH increases the interaction of the molecule through the amine functional groups as the adsorption geometry reported by Guo et al suggests.[44]

The absorbance changes observed as a function of substrate incubation time in the solutions are analyzed using the Langmuir adsorption isotherm based on the integral area under the curves in **Figure 5.4**b and d by defining a parameter as

$$\eta = \frac{\Delta A_{i,t}}{\Delta A_{i,M}} \qquad Eq\ 5$$

where $\Delta A_{i,t}$ and $\Delta A_{i,m}$, respectively, are integral (i) areas at any time (t) and infinite time when monolayer (m) surface coverage is assumed. As shown in panel (a) and (b) in **Figure 5.5** for MB and TH, η increases with time first rapidly and then saturates exhibiting characteristics of a Langmuir adsorption isotherm for monolayer surface coverage. The rise time constants are estimated as 3 – 9 minutes for both MB and thionine adsorption on the gold nanostructures by fitting an exponential function. We note that the adsorption isotherms determined from the induced absorption changes compares favorably with the

time dependence of the plasmon resonance wavelength shift presented in **Figure 5.5**c and d for MB and TH, respectively. However, it is important to note that the plasmon wavelength shift ($\Delta\lambda$) increases much faster than η initially.

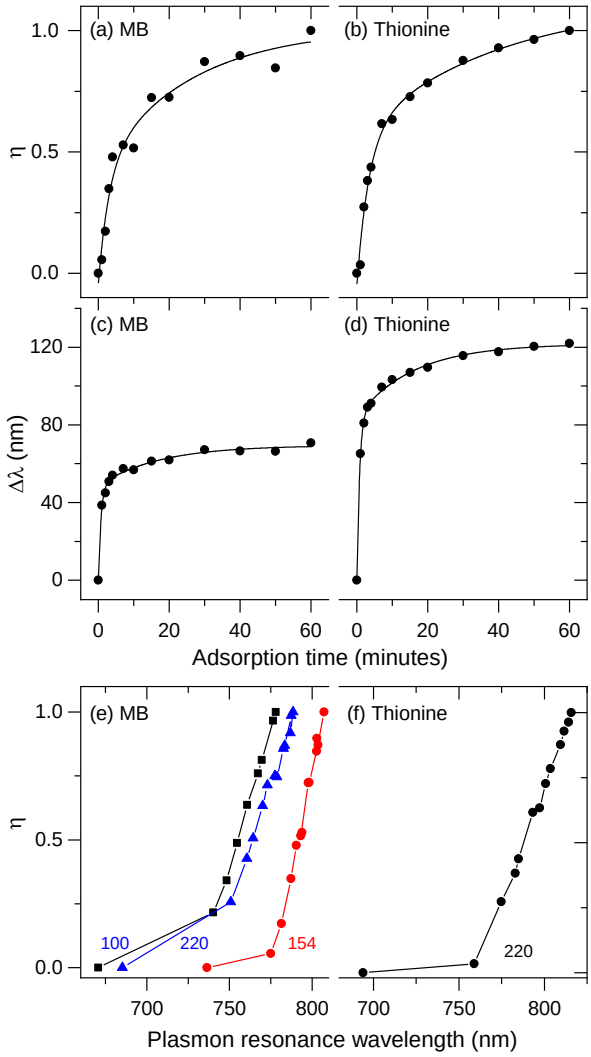

Figure 5.5 (a, b) Adsorption isotherms determined from plasmonic absorbance intensity changes induced by MB (a) and TH (b). (c, d) Adsorption isotherms determined from plasmon resonance wavelength shifts induced by MB (c) and TH (d). (e, f) Correlation between normalized intensity changes and plasmon resonance wavelength shift for MB (e) and TH (f) The numbers in (e) indicate the concentration in □M of MB water, in which nominally the same AuNIs are immersed.

Fitting a bi-exponential function ($\Delta\lambda = \Delta\lambda_m - ae^{-t/\tau_1} - be^{-t/\tau_2}$, where $\Delta\lambda_m$ is the plasmon resonance wavelength shift at infinite adsorption time that may result in monolayer surface coverage) to the data produces $\Delta\lambda_m = 69\ nm$, $\tau_1 = 0.74\ min$ and $\tau_2 = 17\ min$ for MB and $\Delta\lambda_m = 122\ nm$, $\tau_1 = 0.76\ min$ and $\tau_2 = 16\ min$ for thionine. While the time constants for MB and thionine adsorbates are comparable, $\Delta\lambda_m$ varies from sample to sample significantly, ranging from 69 nm to 113 nm for MB on five different AuNIs. On the other hand, for most fabricated gold nanoislands, adsorption of TH shifts the resonance wavelength outside the detection window of our spectrometer as shown in **Figure 5.4**c. It is interesting to note that the larger plasmon resonance shift for TH corresponds to the more pronounced molecular resonance shift as mentioned earlier in comparing the results in panel b and d of **Figure 5.4.**

The plots presented in panels e and f of **Figure 5.5** indicate a linear correlation between η and $\Delta\lambda$ except at the transition from the bare AuNIs to the shortest adsorption time (one minute). This deviation can be attributed to lack of clear background reference for extracting the adsorbate induced change in the plasmonic absorbance, while the plasmon resonance shift can be monitored accurately and unambiguously. A more accurate procedure for extracting η accurately is particularly important at very short incubation time that results in low number density of adsorbates.

So far, the reduction of the plasmonic absorbance intensity at the absorption band of the adsorbates has been discussed in terms of the electronic excitation energy coupling to the surface plasmon modes. Alternatively, the observation may be explained in terms of chemical interface plasmon damping (CIPD) in which the surface plasmon field is used up for pumping the electronic excitation of the molecular adsorbates. Since the adsorbates are

directly adsorbed on the metal surface, vibrational relation in the excited electronic state may be unlikely to compete with the excitation coupling to the plasmon mode. This explains the similarity of the ΔA spectral shape (see **Figure 5.4**b) to the absorption band of MB in solution as opposed to the fluorescence band, which appears as the mirror image of the former. In this regard, the CIPD effect can result in the same experimental observation except that the terminology is appropriate only to account for the dephasing of plasmon resonances. We note that CIDP effect has been studied extensively based on homogeneous linewidth broadening of single particle scattering spectra.[45-48] However, it is practically impossible to read out signatures of absorption bands of adsorbates based on the CID effect on single particle spectra, which are relatively narrow and shifts significantly upon adsorption. The broad plasmon resonance of the evaporated gold nanoislands is advantageous to observe the electronic transition bands of adsorbates in analogy to infrared vibrational absorption spectroscopy.

5.4 Conclusion

In this study, we established a method of sub-monolayer sensitivity to measure surface absorbance of methylene blue and thionine dyes on gold nanoparticles via coupling of adsorbate excitation and localized surface plasmon resonance of well-defined nanoisland structure in thin gold film. The magnitude of spectral red shift and line shape broadening of electronic absorption band of physisorbed molecules depend on the degree of molecule-surface interaction and their preferential orientation on the surface. Parallel trend is determined in adsorption kinetics of the dye molecules which is analyzed from the area under surface absorption curve as function of time. Linear correlation is observed between the adsorption isotherm and adsorption induced shifts in peak wavelength of the localized

surface plasmon resonance of gold nanostructure. The method is simple and requires conventional UV-visible spectrometer and it is surface specific process offering useful insights in the interpretation of ultrasensitive spectroscopic signature and enhanced surface photochemistry of molecular species.

5.5 References

1. Salomon, L., Grillot, F., Zayats, A.V. & de Fornel, F. Near-field distribution of optical transmission of periodic subwavelength holes in a metal film. *Phys Rev Lett* **86**, 1110-3 (2001).

2. Singh, M.R., Schindel, D.G. & Hatef, A. Dipole-dipole interaction in a quantum dot and metallic nanorod hybrid system. *Applied Physics Letters* **99**, 181106 (2011).

3. Cheng, M.-T., Liu, S.-D., Zhou, H.-J., Hao, Z.-H. & Wang, Q.-Q. Coherent exciton-plasmon interaction in the hybrid semiconductor quantum dot and metal nanoparticle complex. *Optics Letters* **32**, 2125-2127 (2007).

4. Gómez, D.E., Roberts, A., Davis, T.J. & Vernon, K.C. Surface plasmon hybridization and exciton coupling. *Physical Review B* **86**, 035411 (2012).

5. Hatef, A., Sadeghi, S.M., Boulais, É. & Meunier, M. Quantum dot–metallic nanorod sensors via exciton–plasmon interaction. *Nanotechnology* **24**, 015502 (2012).

6. Hatef, A., Sadeghi, S.M., Fortin-Deschenes, S., Boulais, E. & Meunier, M. Coherently-enabled environmental control of optics and energy transfer pathways of hybrid quantum dot-metallic nanoparticle systems. *Opt Express* **21**, 5643-53 (2013).

7. Liu, M., Lee, T.-W., Gray, S.K., Guyot-Sionnest, P. & Pelton, M. Excitation of Dark Plasmons in Metal Nanoparticles by a Localized Emitter. *Physical Review Letters* **102**, 107401 (2009).

8. Kajetan Schmidt, M., Mackowski, S. & Aizpurua, J. Control of single emitter radiation by polarization- and position-dependent activation of dark antenna modes. *Optics Letters* **37**, 1017-1019 (2012).

9. Bryant, G.W., Artuso, R.D., Garcia-Etxarri, A. & Aizpurua, J. in CLEO:2011 - Laser Applications to Photonic Applications QThL3 (Optical Society of America, Baltimore, Maryland, 2011).

10. Pendry, J. Playing Tricks with Light. *Science* **285**, 1687-1688 (1999).

11. Kitson, S.C., Barnes, W.L. & Sambles, J.R. Full Photonic Band Gap for Surface Modes in the Visible. *Physical Review Letters* **77**, 2670-2673 (1996).

12. Villeneuve, P.R. Light beats the diffraction limit. *Physics World* **11**, 28-29 (1998).

13. Kitson, S.C., Barnes, W.L. & Sambles, J.R. Surface-plasmon energy gaps and photoluminescence. *Physical Review B* **52**, 11441-11445 (1995).

14. Ghaemi, H.F., Thio, T., Grupp, D.E., Ebbesen, T.W. & Lezec, H.J. Surface plasmons enhance optical transmission through subwavelength holes. *Physical Review B* **58**, 6779-6782 (1998).

15. Kitson, S.C., Barnes, W.L. & Sambles, J.R. Photoluminescence from dye molecules on silver gratings. *Optics Communications* **122**, 147-154 (1996).

16. Dintinger, J., Klein, S. & Ebbesen, T.W. Molecule–Surface Plasmon Interactions in Hole Arrays: Enhanced Absorption, Refractive Index Changes, and All-Optical Switching. *Advanced Materials* **18**, 1267-1270 (2006).

17. Williams, S.M., Stafford, A.D., Rodriguez, K.R., Rogers, T.M. & Coe, J.V. Accessing Surface Plasmons with Ni Microarrays for Enhanced IR Absorption by Monolayers. *The Journal of Physical Chemistry B* **107**, 11871-11879 (2003).

18. Ihara, M., Tanaka, K., Sakaki, K., Honma, I. & Yamada, K. Enhancement of the absorption coefficient of cis-(NCS)(2) bis(2,2'-bipyridyl-4,4'-dicarboxylate)ruthenium(II) dye in dye-sensitized solar cells by a silver island film. *Journal of Physical Chemistry B* **101**, 5153-5157 (1997).

19. Glass, A.M., Liao, P.F., Bergman, J.G. & Olson, D.H. Interaction of metal particles with adsorbed dye molecules: absorption and luminescence. *Optics Letters* **5**, 368-370 (1980).

20. Craighead, H.G. & Glass, A.M. Optical absorption of small metal particles with adsorbed dye coats. *Optics Letters* **6**, 248-250 (1981).

21. Wiederrecht, G.P., Wurtz, G.A. & Hranisavljevic, J. Coherent Coupling of Molecular Excitons to Electronic Polarizations of Noble Metal Nanoparticles. *Nano Lett* **4**, 2121-2125 (2004).

22. Fofang, N.T. et al. Plexcitonic Nanoparticles: Plasmon−Exciton Coupling in Nanoshell−J-Aggregate Complexes. *Nano Lett* **8**, 3481-3487 (2008).

23. Ni, W. et al. Effects of Dyes, Gold Nanocrystals, pH, and Metal Ions on Plasmonic and Molecular Resonance Coupling. *Journal of the American Chemical Society* **132**, 4806-4814 (2010).

24. Ni, W., Ambjörnsson, T., Apell, S.P., Chen, H. & Wang, J. Observing Plasmonic−Molecular Resonance Coupling on Single Gold Nanorods. *Nano Lett* **10**, 77-84 (2010).

25. Zengin, G. et al. Approaching the strong coupling limit in single plasmonic nanorods interacting with J-aggregates. *Sci Rep* **3**, 3074 (2013).

26. Schlather, A.E., Large, N., Urban, A.S., Nordlander, P. & Halas, N.J. Near-Field Mediated Plexcitonic Coupling and Giant Rabi Splitting in Individual Metallic Dimers. *Nano Lett* **13**, 3281-3286 (2013).

27. Zengin, G. et al. Realizing Strong Light-Matter Interactions between Single-Nanoparticle Plasmons and Molecular Excitons at Ambient Conditions. *Physical Review Letters* **114**, 157401 (2015).

28. Chikkaraddy, R. et al. Single-molecule strong coupling at room temperature in plasmonic nanocavities. *Nature* **535**, 127-130 (2016).

29. Darby, B.L., Auguié, B., Meyer, M., Pantoja, A.E. & Le Ru, E.C. Modified optical absorption of molecules on metallic nanoparticles at sub-monolayer coverage. *Nature Photonics* **10**, 40 (2015).

30. Zhao, J. et al. Interaction of Plasmon and Molecular Resonances for Rhodamine 6G Adsorbed on Silver Nanoparticles. *Journal of the American Chemical Society* **129**, 7647-7656 (2007).

31. Novotny, L. & Hecht, B. Principles of Nano-Optics (Cambridge University Press, Cambridge, 2006).

32. Hutchison, J.A., O'Carroll, D.M., Schwartz, T., Genet, C. & Ebbesen, T.W. Absorption-Induced Transparency. *Angewandte Chemie International Edition* **50**, 2085-2089 (2011).

33. Kühn, S., Håkanson, U., Rogobete, L. & Sandoghdar, V. Enhancement of single-molecule fluorescence using a gold nanoparticle as an optical nanoantenna. *Phys. Rev. Lett* **97** (2006).

34. Le Ru, E.C. Mechanisms of spectral profile modification in surface-enhanced fluorescence. *J. Phys. Chem. C* **111** (2007).

35. Aroca, R. Surface-Enhanced Vibrational Spectroscopy (2006).

36. Le Ru, E.C. & Etchegoin, P.G. Principles of Surface Enhanced Raman Spectroscopy and Related Plasmonic Effects (2009).

37. Moskovits, M. Surface-enhanced spectroscopy. *Rev. Mod. Phys* **57** (1985).

38. Galloway, C.M., Artur, C., Grand, J. & Le Ru, E.C. Photobleaching of fluorophores on the surface of nanoantennas. *J. Phys. Chem. C* **118** (2014).

39. Kleinman, S.L., Frontiera, R.R., Henry, A.I., Dieringer, J.A. & Van Duyne, R.P. Creating, characterizing, and controlling chemistry with SERS hot spots. *Phys. Chem. Chem. Phys* **15** (2013).

40. Linic, S., Christopher, P. & Ingram, D.B. Plasmonic-metal nanostructures for efficient conversion of solar to chemical energy. *Nature Mater.* **10** (2011).

41. Xu, S., Shan, J., Shi, W., Liu, L. & Xu, L. Modifying photoisomerization efficiency by metallic nanostructures. *Opt. Express* **19** (2011).

42. Darby, B.L., Auguie, B., Meyer, M., Pantoja, A.E. & Le Ru, E.C. Modified optical absorption of molecules on metallic nanoparticles at sub-monolayer coverage. *Nature Photonics* **10**, 40-U54 (2016).

43. Zhong, X. et al. Waveguide and Plasmonic Absorption-Induced Transparency. *ACS Nano* **10**, 4570-4578 (2016).

44. Zhou, L., Johnson, R., Habteyes, T. & Guo, H. Adsorption of methylene blue and its N-demethylated derivatives on the (111) face of coinage metals: The importance of dispersion interactions. *The Journal of Chemical Physics* **146**, 164701 (2017).

45. Olson, J. et al. Optical characterization of single plasmonic nanoparticles. *Chemical Society Reviews* **44**, 40-57 (2015).

46. Hövel, H., Fritz, S., Hilger, A., Kreibig, U. & Vollmer, M. Width of cluster plasmon resonances: Bulk dielectric functions and chemical interface damping. *Physical Review B* **48**, 18178-18188 (1993).

47. Zijlstra, P., Paulo, P.M.R., Yu, K., Xu, Q.-H. & Orrit, M. Chemical Interface Damping in Single Gold Nanorods and Its Near Elimination by Tip-Specific Functionalization. *Angewandte Chemie International Edition* **51**, 8352-8355 (2012).

48. Foerster, B. et al. Chemical Interface Damping Depends on Electrons Reaching the Surface. *ACS Nano* **11**, 2886-2893 (2017).

6 Future work

6.1 Plasmon Assisted photobiology of phenothiazinium dyes

Methylene blue and its N-demethylation analogous are among the most prominent compound, are perhaps the best-known photosensitizers used in photodynamic inactivation of bacteria and viruses[1-3] as well as photodynamic therapy in cancer treatment.[4-6] According to photophysical and photochemical investigations, plasmon assisted characteristics of phenothiazinium dyes are very important for application in photobiology.[7] The physisorption of these cationic dyes on gold nanorods (AuNR) facilitates uptake pathways in the internalization process of dye-particle system into a biological target.[8] Notably, the dye-AuNR system has higher tendency to be localize and bind selectively to a target organelle (e.g. mitochondria).[9-11] This is very crucial as free dyes are usually distribute in several cell components and organelles and limits fraction of dyes bound to the target. More importantly, the optical density of these dyes are highly amplified by resonance excitation of the gold nanorods and enables the photosensitizer to generate high quantum yield of singlet oxygen at a lower dose. Both gold nanorods and the phenothiazinium dyes absorb photons in the therapeutic window (600-950 nm) and the coupled systems undergo very efficient intersystem crossing, a highly desirable property for photodynamic therapy (PDT) that selectively enhance singlet oxygen generation.

Hence, plasmon-enhanced electronic excitation of organic adsorbates can be readily extended to research in photobiology and optimize methods for medical application.

6.2 Correlation of near-field distribution and Raman scattering

Tip-based near-field optical microscopy can map near-field distribution (**Figure 6.1**)[12-14] and Raman scattering[15-18] in real space with high spatial resolution. These super-resolution capabilities can be combined to correlate plasmon-field localization with reactivity because with continual improvements of the tip-based microscopy it may be possible to resolve the distribution of the reactant and product species adsorbed on individual plasmonic nanoparticles. For example, a recent report by Apkarian and co-workers demonstrates the possibility of imaging electrostatic fields with sub-molecular spatial resolution using tip-enhanced Raman scattering for imaging charge density distribution on single metalloporphyrins adsorbed on Au(111).[19]

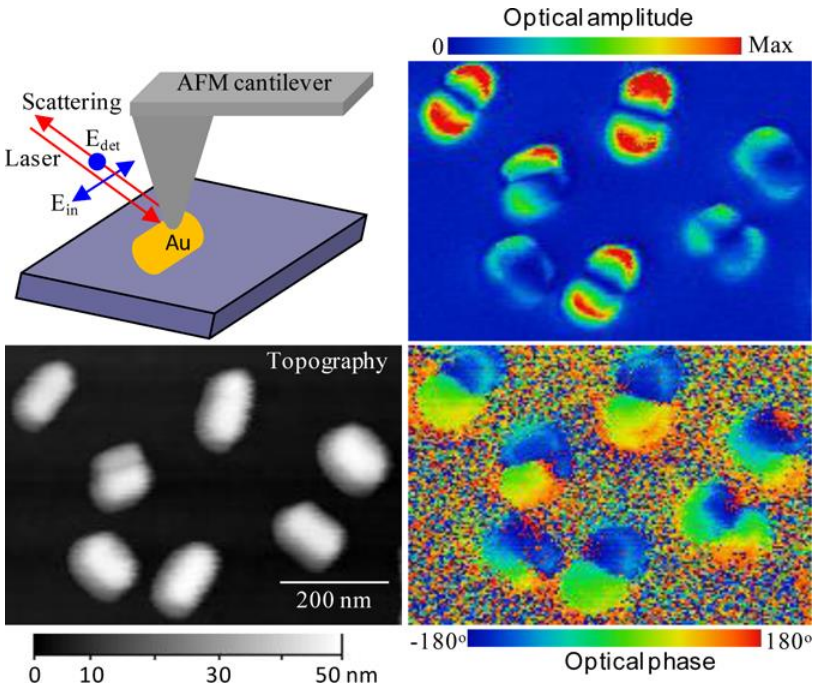

Figure 6.1 Experimental setup and near-field optical amplitude and optical phase images of gold nanorods randomly dispersed on oxide-coated silicon wafer. Adapted with permission from reference [14] Copyright (2014) American Chemical Society.

6.3 Exciton-Induced excitation of higher order plasmonic mode

Because of diffraction limited resolving capacity, mechanistic study of interparticle interaction of nanoscale materials applicable in emerging technologies such as sensing, [20] catalysis,[21] and energy conversion[22] is difficult by using conventional optical microscopy. Developing a novel high resolution near-field optical microscopic imaging method is crucial to study the fundamentals of the interaction between metamaterials such as semiconductor quantum dot (QD) and plasmonic metal nanoparticles.

To this end, we developed a method to control and understand the behavior of self-assembled quantum dots that will be coupled with plasmonic metal nanoparticle. The schematic of the model system for future study is depicted in Figure 6.2. Preliminary studies of the behavior of QD at different interfaces before placing mono-dispersed plasmonic metal nanoparticle for coupling study have be performed and the results are presented in **Figure 6.3-Figure 6.6**.

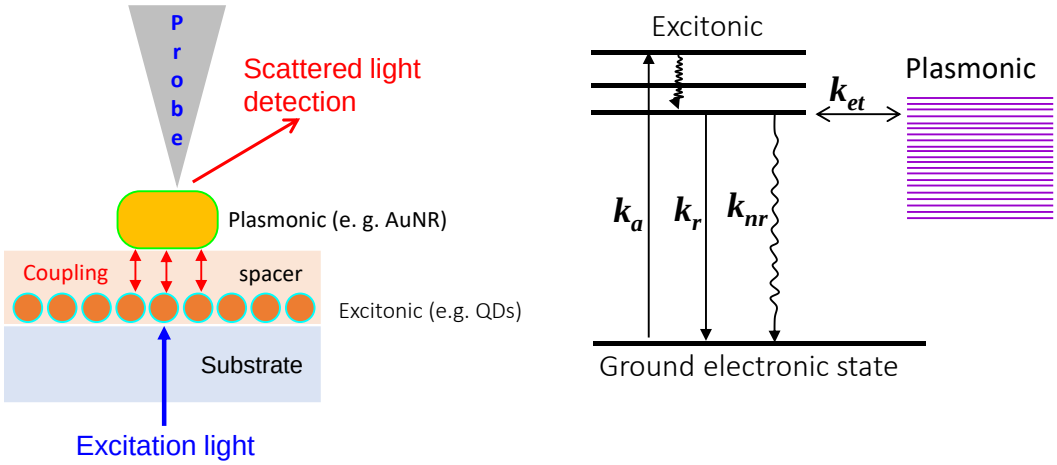

Figure 6.2 schematic show method for probing plasmon-exciton interaction

The self-assembly of close-packed QDs and optically transparent spacing material films were prepared by layer-by-layer assembly using Langmuir-Blodgett (LB) technique. The thickness of LB film was characterized by AFM (**Figure 6.3**a) and their photoluminescence spectra of two QDs, yellow emitting (QD450 nm) and red emitting (QD645 nm) is shown in **Figure 6.3**c**.**

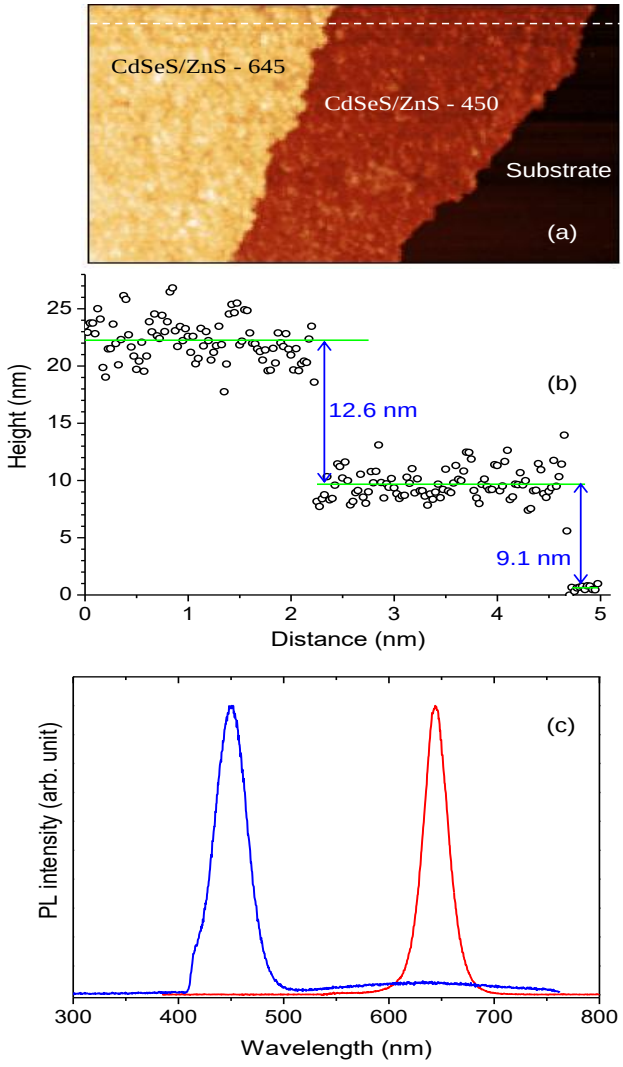

Figure 6.3 AFM image of Langmuir Blodgett (LB) monolayer films of CdSeS/ZnS-645, QD645 (orange) on top of monolayer of CdSeS/ZnS-450, QD450 (red). The substrate (black) is an oxide coated silicon wafer. (b) AFM film thickness profile measured along white dashed line. (c) Photoluminescence spectra of QD450 and QD645. The average size of QD450 and QD645 are 9.1 and 12.6 nm respectively

A close-packed monolayer of Oleic acid on the surface of the dots maintains ~1.1 nm spacing between the QDs. The optical phenomena due to the close-packed of arrays of ternary QDs of different size and composition were studied by the continuous illumination ($I \approx 55$ kW/cm^2) of monolayer film with 532 nm laser. The change in optical properties, *i.e.* peak intensity, peak wavelength, and full width at half maximum (FWHM) have been determined for spectra acquired at different time interval for a period of 1.40 hrs. It has been observed (see **Figure 6.4**a,c) that for a double layer of QD645-QD450 system the peak position and peak intensity undergone dramatic decrease with time upon a continuous illumination of the sample with 532 nm excitation wavelength. Whereas the peak PL position and peak intensity for a system of QD645 on oxide coated silicon and a binary QD (CdSe/ZnS (QD 630)) were observed to show no change upon exposure to the laser for the same duration. We fit the abrupt decline in the peak position as a function of time to the exponential decay with time constant τ_1 and τ_2 equals to ~8.40 min. and 1 ½ hrs., respectively. **Figure 6.4**b shows the change in the change in full width at half maxima (FWHM) undergo drastic exponentially increase for the QD645-QD450 system, whereas the corresponding values remain constant for the QD645 on glass and QD630-QD450 system. These show a particular type of interaction is happening between the monolayers of these ternary QDs.

The major difference between the QD450 (yellow emitting) and QD645 (red emitting) ternary QDs is that Se/S mole ratio in the core of the red QD is greater than that of yellow. This situation causes anisotropic strain within the core and at the core/shell interface in each monolayer. If the system under this constraint is photo-excited on the red absorption

edge of the QD450, the applied optical field may induce strain that will result in the modulation of the optical properties of the system.

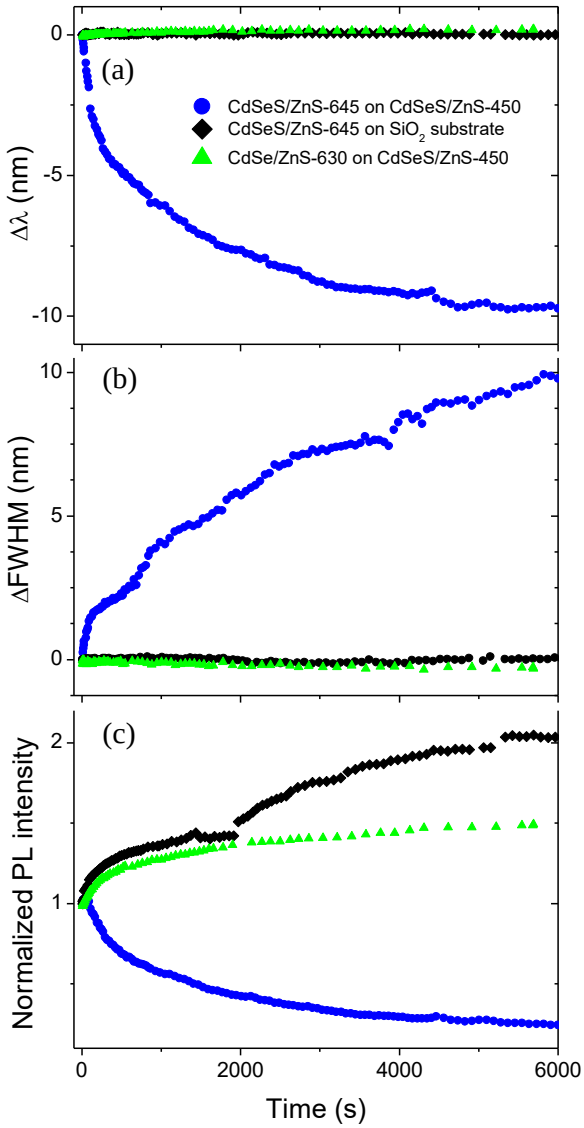

Figure 6.4 Photoluminescence (PL) peak position shift (a), FWHM shift (b), and normalized peak intensity (c) as a function of time at excitation wavelength of 532 nm for a system of QD645 on QD450 (blue dot); QD645 on glass (black diamond); QD630 on QD450 (green triangle).

Figure 6.5 summarizes results of the excitation of the film from the blue absorption edge of the yellow (QD450). Electronic energy transfer from the slightly smaller QD450

(yellow) to the larger QD645(red) cause rapid quenching of the PL of yellow dot while that of red dot is significantly enhanced as a result of strong inter dot coupling. The exponential red-shift of PL peak position of QD450 with time while that of QD645 is blue shifting may be attributed to electronic energy transfer coupling

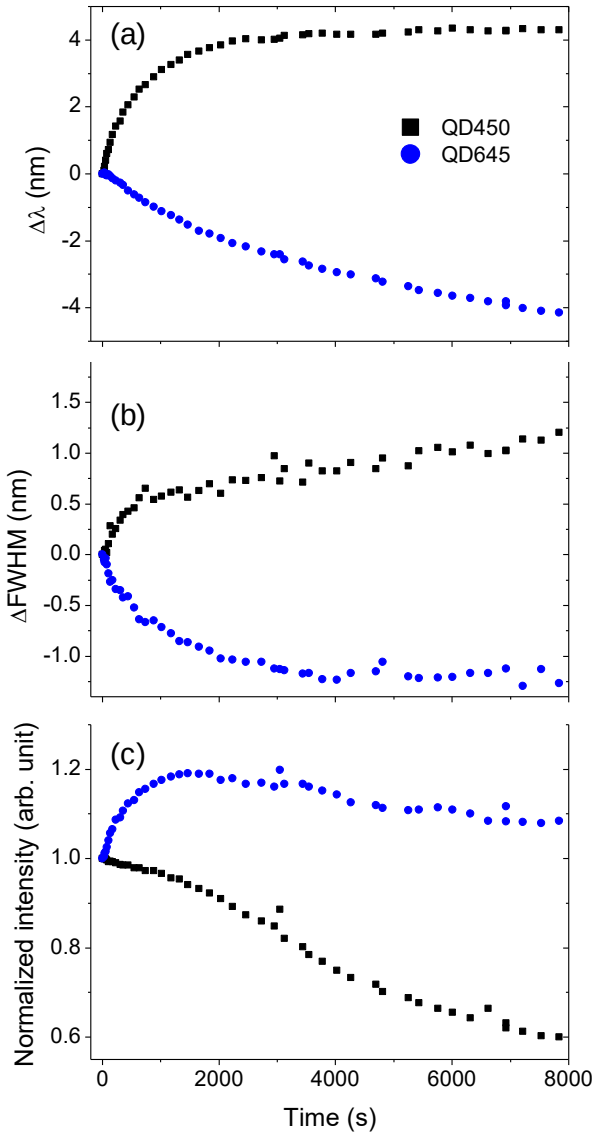

Figure 6.5 Photoluminescence (PL) peak position shift (a), FWHM shift (b), and normalized peak intensity (c) as a function of time at excitation wavelength of 405 nm for a system of QD645 on QD450. Blue dot is for QD645 spectrum and black diamond is for QD450

The data in **Figure 6.6** show the variation of the QD645-QD450 model system at different intensities of a laser source. The trends in emission peak, fwhm, and normalized intensities with time at various intensities of light source follow a linear increase in the energy gap with time for low intensity laser. The non-linearity in the band-gap energy with increasing laser power indicates the presence of nonlinear effect at higher intensities.

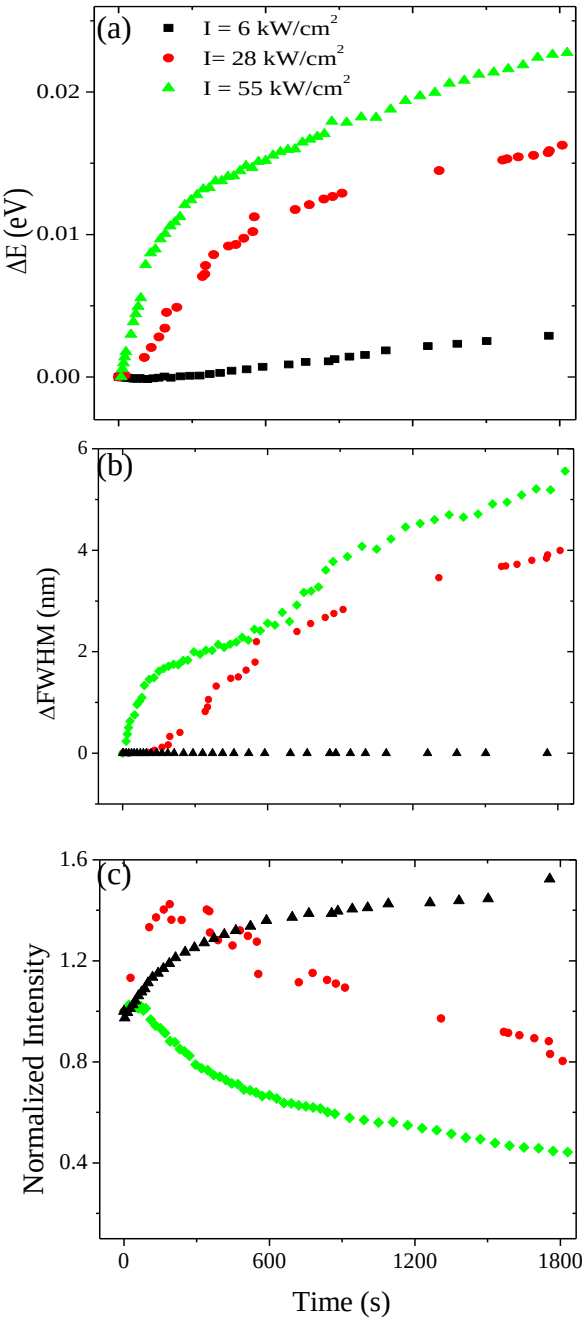

Figure 6.6 Variation in emission peak position (a), FWHM (b), and normalized intensity (c) as a function of time at different intensities of light source. Low intensity, 6 kW/cm^2 (black square), medium intensity, 28 kW/cm^2 (red dot), and high intensity, 55 kW/cm^2 (green diamond)

6.4 References

1. Floyd, R.A. Serendipitous findings while researching oxygen free radicals. *Free radical biology & medicine* **46**, 1004-1013 (2009).

2. Wiehe, A., O'Brien, J.M. & Senge, M.O. Trends and targets in antiviral phototherapy. *Photochemical & Photobiological Sciences* **18**, 2565-2612 (2019).

3. Menezes, P.F.C., Bernal, C., Imasato, H., Bagnato, V.S. & Perussi, J.R. Photodynamic activity of different dyes. *Laser Physics* **17**, 468-471 (2007).

4. dos Santos, A.F. et al. Fluence Rate Determines PDT Efficiency in Breast Cancer Cells Displaying Different GSH Levels. *Photochemistry and Photobiology* **n/a**.

5. Hosseinzadeh, R. & Khorsandi, K. Photodynamic effect of Zirconium phosphate biocompatible nano-bilayers containing methylene blue on cancer and normal cells. *Scientific Reports* **9**, 14899 (2019).

6. Zhao, J., Zhong, D. & Zhou, S. NIR-I-to-NIR-II fluorescent nanomaterials for biomedical imaging and cancer therapy. *Journal of Materials Chemistry B* **6**, 349-365 (2018).

7. Bunting, J.R. A test of the singlet oxygen mechanism of cationic dye photosensitization of mitochondrial damage. *Photochemistry and Photobiology* **55**, 81-87 (1992).

8. Wang, L. et al. Selective Targeting of Gold Nanorods at the Mitochondria of Cancer Cells: Implications for Cancer Therapy. *Nano Letters* **11**, 772-780 (2011).

9. Tardivo, J.P. et al. Methylene blue in photodynamic therapy: From basic mechanisms to clinical applications. *Photodiagnosis and Photodynamic Therapy* **2**, 175-191 (2005).

10. Kessel, D. & Luo, Y. Mitochondrial photodamage and PDT-induced apoptosis. *Journal of Photochemistry and Photobiology B: Biology* **42**, 89-95 (1998).

11. Kandela, I.K., Bartlett, J.A. & Indig, G.L. Effect of molecular structure on the selective phototoxicity of triarylmethane dyes towards tumor cells. *Photochemical & Photobiological Sciences* **1**, 309-314 (2002).

12. Kiesow, K.I., Dhuey, S. & Habteyes, T.G. Mapping near-field localization in plasmonic optical nanoantennas with 10 nm spatial resolution. *Applied Physics Letters* **105**, 053105 (2014).

13. Habteyes, T.G., Dhuey, S., Kiesow, K.I. & Vold, A. Probe-sample optical interaction: size and wavelength dependence in localized plasmon near-field imaging. *Optics Express* **21**, 21607-21617 (2013).

14. Habteyes, T.G. Direct near-field observation of orientation-dependent optical response of gold nanorods. *The Journal of Physical Chemistry C* **118**, 9119-9127 (2014).

15. Sun, M., Zhang, Z., Zheng, H. & Xu, H. In-situ plasmon-driven chemical reactions revealed by high vacuum tip-enhanced Raman spectroscopy. *Scientific Reports* **2**, 647 (2012).

16. Zrimsek, A.B. et al. Single-Molecule Chemistry with Surface- and Tip-Enhanced Raman Spectroscopy. *Chemical Reviews* **117**, 7583-7613 (2017).

17. Lee, J. et al. Tip-Enhanced Raman Spectromicroscopy of Co(II)-Tetraphenylporphyrin on Au(111): Toward the Chemists' Microscope. *ACS Nano* **11**, 11466-11474 (2017).

18. Harvey, C.E. & Weckhuysen, B.M. Surface- and Tip-Enhanced Raman Spectroscopy as Operando Probes for Monitoring and Understanding Heterogeneous Catalysis. *Catalysis Letters* **145**, 40-57 (2015).

19. Lee, J., Tallarida, N., Chen, X., Jensen, L. & Apkarian, V.A. Microscopy with a single-molecule scanning electrometer. *Science Advances* **4**, eaat5472 (2018).

20. Wu, B.-Y., Wang, H.-F., Chen, J.-T. & Yan, X.-P. Fluorescence Resonance Energy Transfer Inhibition Assay for α-Fetoprotein Excreted during Cancer Cell Growth Using Functionalized Persistent Luminescence Nanoparticles. *Journal of the American Chemical Society* **133**, 686-688 (2011).

21. Liu, Z., Hou, W., Pavaskar, P., Aykol, M. & Cronin, S.B. Plasmon Resonant Enhancement of Photocatalytic Water Splitting Under Visible Illumination. *Nano Letters* **11**, 1111-1116 (2011).

22. Atwater, H.A. & Polman, A. Plasmonics for improved photovoltaic devices. *Nature Materials* **9**, 205-213 (2010).

1 Appendix A

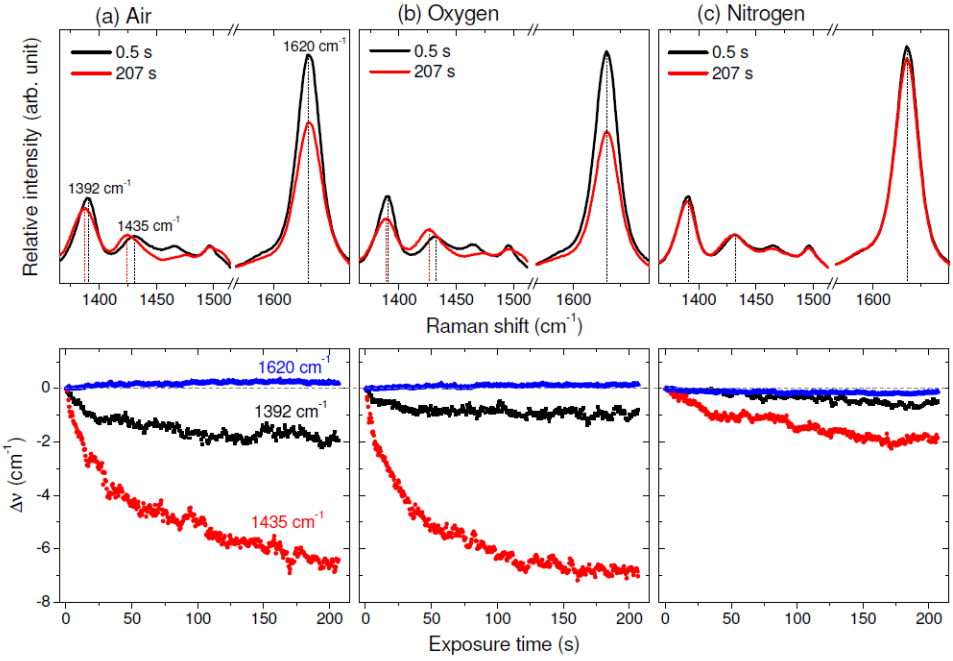

A 1 Vibrational frequency shift as a function of exposure time. Top panels: the first (black line) and the last (red line) spectra out of 400 spectra recorded sequentially during the continuous illumination of the MB-AuNR sample for ~207 seconds in (a) air, (b) oxygen and (c) nitrogen atmospheres. Bottom panels: the vibration frequency peak values plotted as a function of exposure time. The peak values are extracted by fitting Gaussian functions to the spectra. Each spectrum is acquired with 0.5 s acquisition time at 633 nm excitation wavelength and 0.4 mW incident laser power.

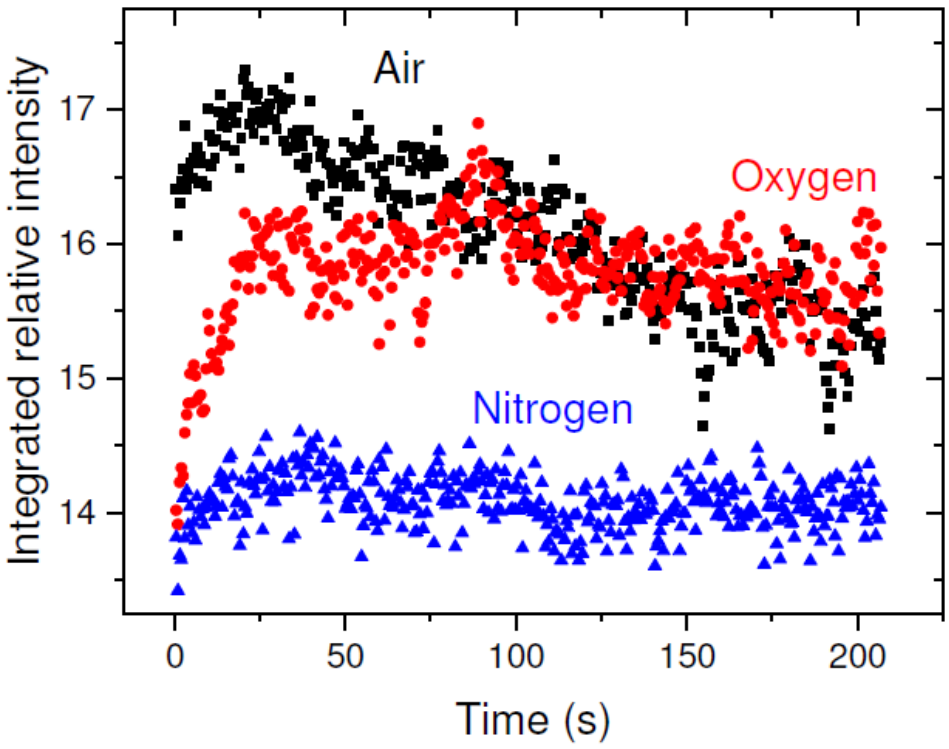

A 2 The initial relative intensity of the 1435 cm-1 band as a function of exposure time at 0.4 mW incident laser power and 0.5 s acquisition times.

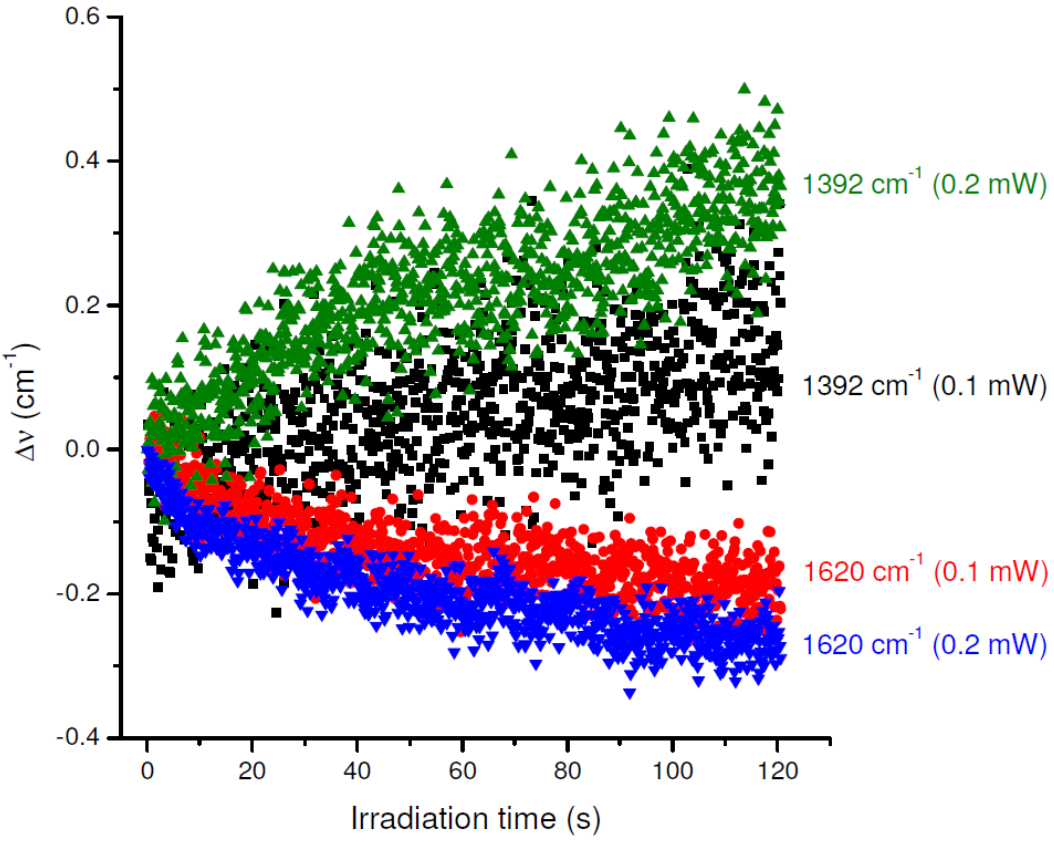

A 3 Frequency shift of the 1392 cm-1 and 1620 cm-1 vibration bands as a function of exposure time in nitrogen atmosphere at different incident laser powers as labeled for a different sample from that used to obtain the data in Figure 3. In each case, the peak values are extracted from 1000 spectra recorded within 120 s continuous exposure time using 0.1 s acquisition time for each spectrum.

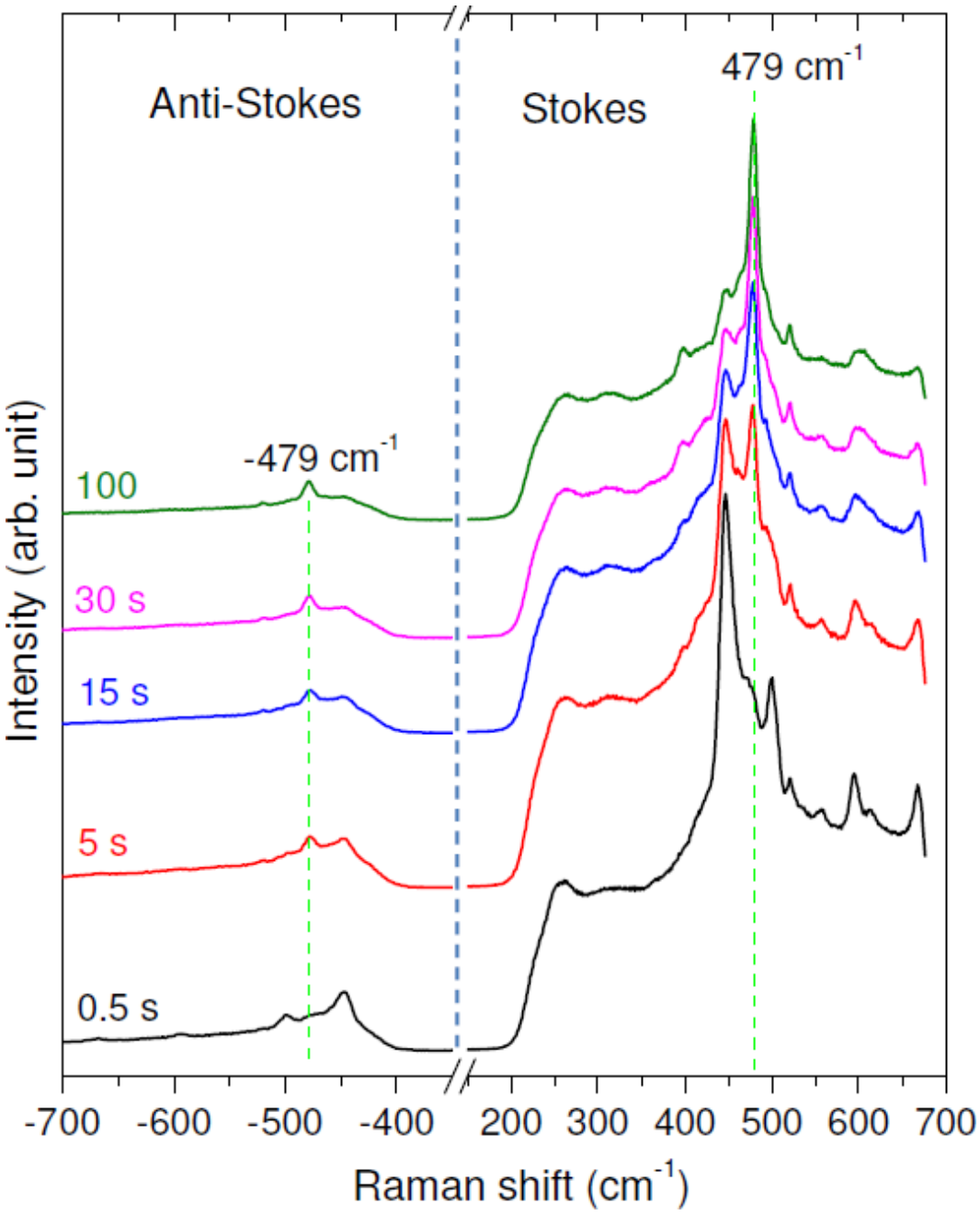

A 4 Comparison of Stokes and anti-Stokes Raman scattering intensities obtained at 633 nm excitation wavelength

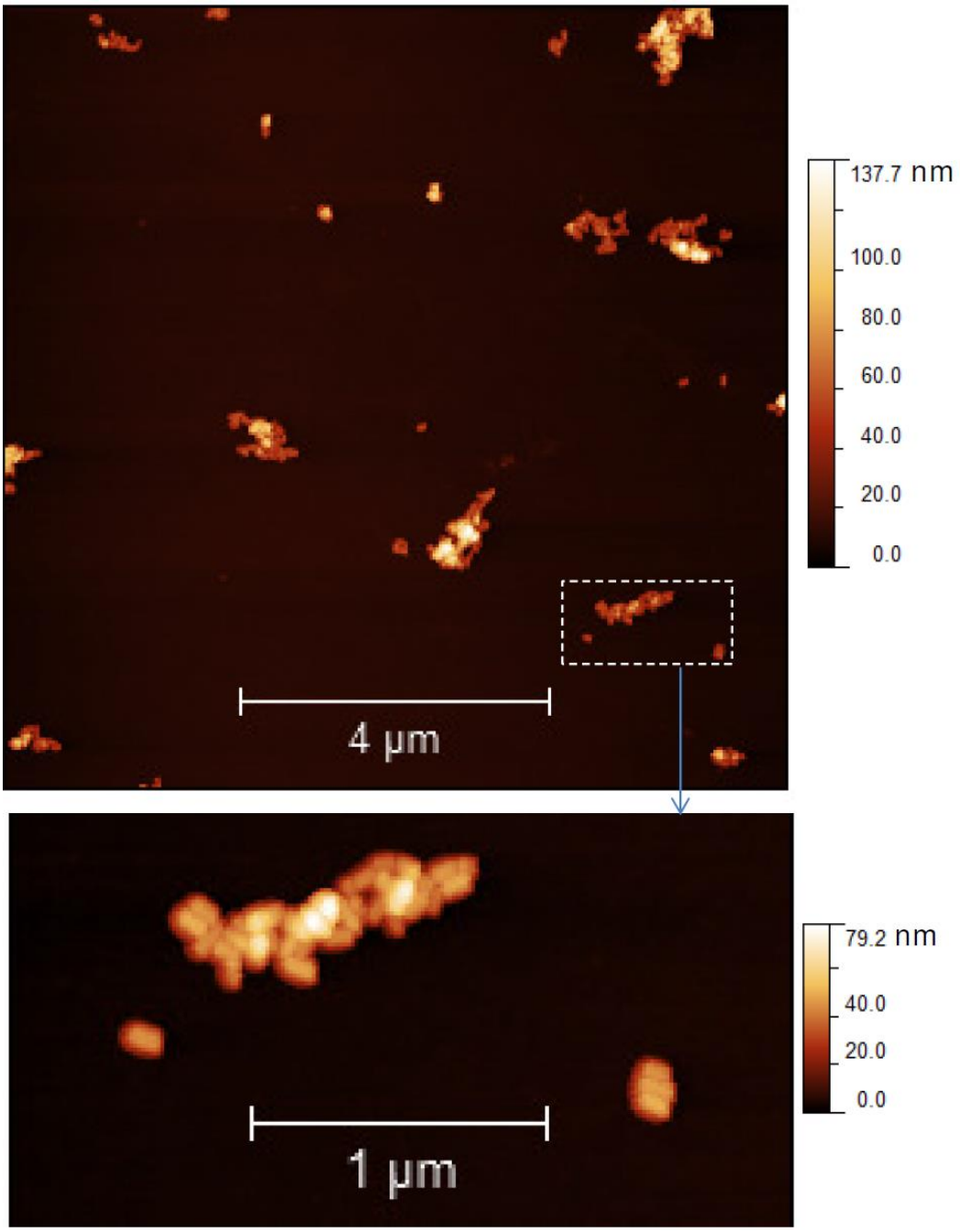

A 5 Representative atomic force microscope topographic images of the gold nanorod aggregates.

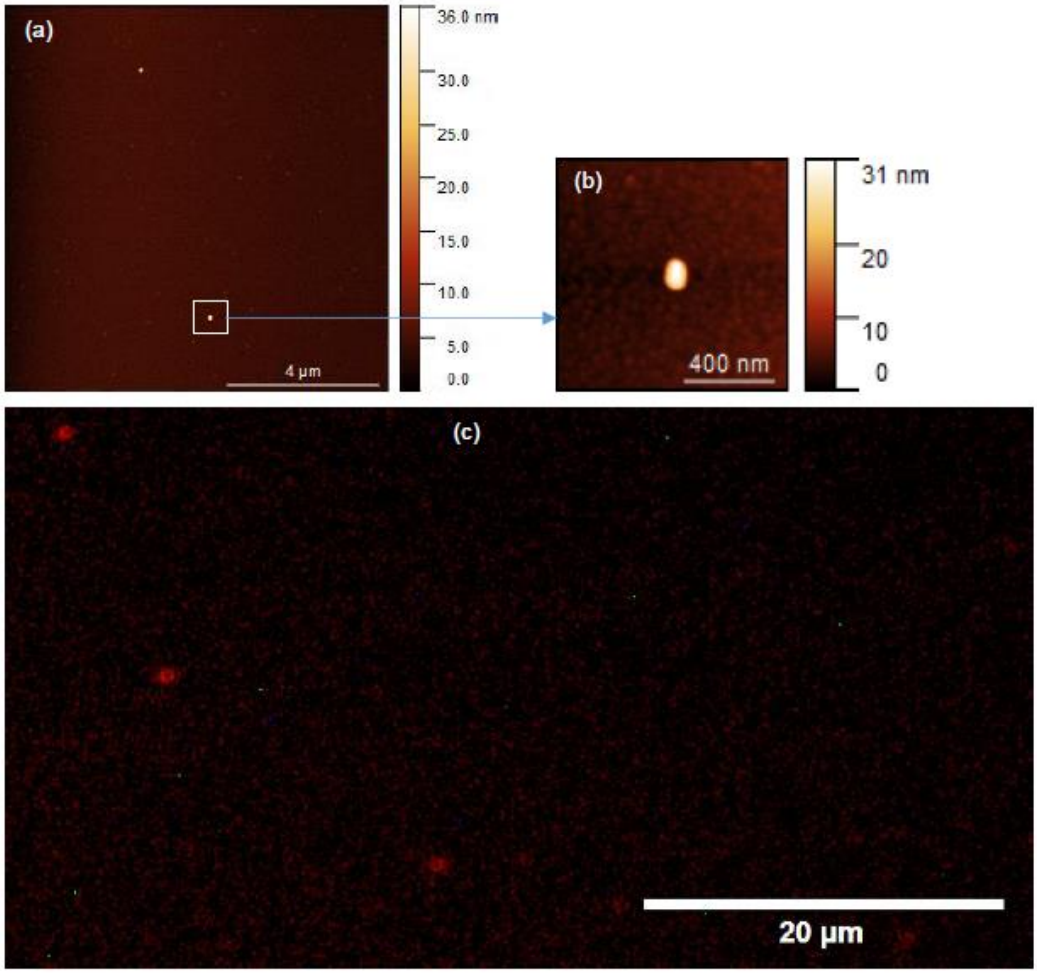

A 6 AFM topography of AuNRs on gold film. (b) AFM image showing the AuNR within the square. (c) Dark-field image of AuNRs on gold film for the same sample as in (a) but not necessarily the same location.

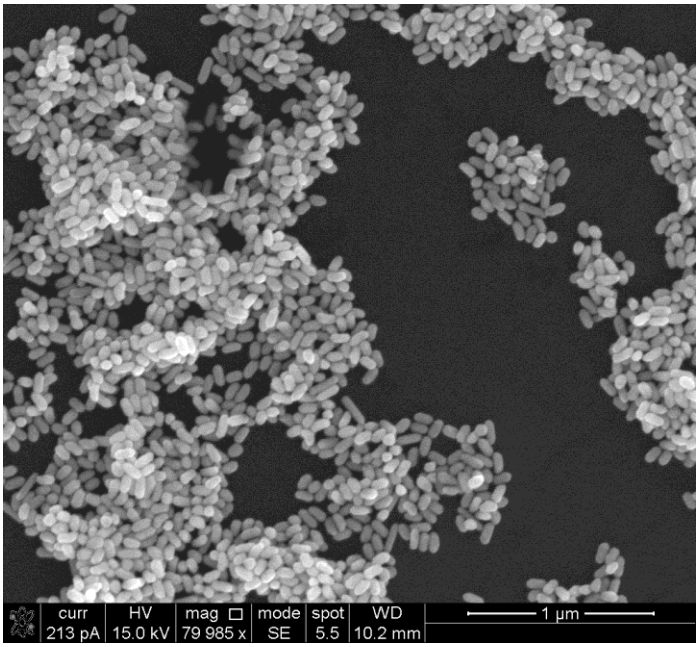

A 7 Self-assembled gold nanorods used as a SERS substrate